

DEMONSTRATION OF OPTICAL TUNABLE DISPERSION COMPENSATION  
WITH A VIRTUALLY-IMAGED PHASED-ARRAY BASED PULSE SHAPER

A Thesis

Submitted to the Faculty

of

Purdue University

by

Ghang-Ho Lee

In Partial Fulfillment of the

Requirements for the Degree

of

Doctor of Philosophy

August 2006

Purdue University

West Lafayette, Indiana

This thesis is dedicate to my father Sun-Yong Lee, my daughter Sejin,  
and my lovely wife Heeju Han.

## ACKNOWLEDGMENTS

I would especially like to thank my advisor Professor Andrew Weiner for his guidance, support, and encouragement throughout my Ph.D. studies. Without his support this work would have never been possible. I would also like to thank my committee members Professor Vladimir Shalaev, Professor Mark Bell, and Professor Xianfan Xu for their support on this thesis.

Thanks to our group members, especially Dr. Dan Leaird, Shijun Xiao, Zhi Jiang, Shawn Wang, Al Vega, and Professor Dongsun Seo for their collaborations and fruitful discussions on various topics. Many thanks to corporate helps including Avanex, Corning, and Ciena for donation and loan of the VIPA and SMF.

Finally, I would like to thank all the friends I made in Purdue who made my life here in West Lafayette enjoyable.

## TABLE OF CONTENTS

	Page
LIST OF TABLES .....	vi
LIST OF FIGURES .....	vii
LIST OF ABBREVIATIONS.....	xiii
ABSTRACT.....	xiv
1. INTRODUCTION .....	1
2. VIPA BASED PULSE SHAPER.....	4
2.1 Virtually Imaged Phased Array .....	4
2.2 VIPA Based Pulse Shaper Design .....	5
2.3 Optical Pulse Burst Manipulation Using VIPA Based Pulse Shaper .....	9
3. OPTICAL TUNABLE DISPERSION COMPENSATION WITH VIPA BASED PULSE SHAPER.....	23
3.1 Fiber Dispersion And Positively Chirped Optical Source .....	23
3.1.1 Basic Propagation Equation.....	23
3.1.2 Dispersion In Single Mode Fiber.....	25
3.1.3 Positively Chirped Optical Source.....	28

	Page
3.2 The Reason For Tunable Dispersion Compensation .....	31
3.2.1 Time Variant Optical Networks.....	31
3.2.2 The Reason For Tunable Dispersion Compensation .....	31
3.3 Previous Works On Optical Tunable Dispersion Compensation.....	34
3.3.1 Previous Works On Optical Tunable Dispersion Compensation.....	36
3.3.2 Figure Of Merit .....	39
3.4 Optical Tunable Dispersion Compensation With A VIPA based TDC.....	39
3.4.1 VIPA Based Optical TDC.....	39
3.4.2 Evaluating System Performances .....	43
3.4.3 Optical Transmission Results Using VIPA Based Optical TDC.....	46
4. RETURN-TO-ZERO LIGHTWAVE TRANSMISSION WITH VIPA BASED PULSE SHAPER.....	79
4.1 Introduction.....	79
4.2 Experiments And Results.....	80
5. CONCLUSION.....	88
LIST OF REFERENCES.....	90
A. LOSS MECHANISMS IN VIPA BASED PULSE SHAPER .....	98
VITA.....	110

## LIST OF TABLES

Table	Page
Table 3.1 Comparison of optical and electrical TDC.....	75
Table 3.2 Characteristics of optical TDC technologies. ....	76
Table 3.3 Comparison of optical TDC technologies. ....	77

## LIST OF FIGURES

Figure	Page
Fig.2.1 (a) Schematic of wavelength decomposition with the VIPA. (b) Details of the VIPA structure. ....	15
Fig.2.2 Example of relation between angular dispersion and wavelength (adapted from [6]). ....	16
Fig.2.3 Generic layout of the Fourier transform pulse shaper. ....	16
Fig.2.4 VIPA Fourier transform pulse shaper response : (a) Example of VIPA response (angular dispersion) with frequency $\omega$ as function of spatial position $x$ . (b) Example of single period quadratic spatial phase function, $\Phi(x)$ , applied at Fourier plane by spatial mask. (c) Resulting periodic quadratic spectral phase function, $\Psi(\omega)$ , applied to input spectrum. ....	17
Fig.2.5 Schematic diagram illustrating effect of applying different spatial masks to identical inputs, $E_{in}(\omega)$ . Input optical spectrum (left trace), applied phase functions (middle traces), resulting output intensity correlations (right traces), $I_{a,out}(t)$ , $I_{b,out}(t)$ , $I_{c,out}(t)$ : (a) No phase applied, $\Psi_a(\omega)$ . (b) Single period quadratic phase function applied, $\Psi_b(\omega)$ . (c) Periodic quadratic phase function applied, $\Psi_c(\omega)$ .....	18
Fig.2.6 Experimental apparatus for programmable Fourier transform pulse shaper based on VIPA. ....	19

Figure	Page
Fig.2.7 Results obtained by applying periodic quadratic phase function with apparatus. Applied phase functions (top trace), resulting output intensity correlation measurements (middle trace), simulated results (bottom trace), dashed line in bottom trace is optical pulse burst envelope function: (a) Phase function varying zero to $\pi/2$ . (b) Phase function varying zero to $\pi$ . (c) Phase function spectrally shifted by 3/4 of single period. (d) Phase function spectrally shifted by $-1/2$ of single period. ....	20
Fig.2.8 Results obtained by applying periodic cubic phase function with apparatus. Applied phase functions (top trace), resulting output intensity correlation measurements (middle trace), simulated results (bottom trace): (a) Phase function varying $-\pi$ to $\pi$ , with negative slope ( $\phi_{cubic} < 0$ ). (b) Phase function with negative slope, spectrally shifted by 1/4 of single period. (c) Phase function with negative slope, spectrally shifted by 3/8 of single period. (d) Phase function varying $-\pi$ to $\pi$ , with positive slope ( $\phi_{cubic} > 0$ ). (e) Phase function with positive slope, spectrally shifted by 1/4 of single period. (f) Phase function with positive slope, spectrally shifted by 3/8 of single period. ....	21
Fig.2.9 Output intensity correlation measurements obtained by applying periodic m-sequence phase function with apparatus. (a) Phase function with 7-element periodic m-sequence (0010111). (b) Phase function with 15-element periodic m-sequence (000100110101111). ....	22
Fig. 3.1 Time resolved spectra speed 100ps apart are shown for the start-up and shut-down portion of a pulse from a positively chirped optical source (adapted from [50]) .....	52
Fig.3.2 Broadening of a 125-psec half-width pulse with the fiber length for three values of the chirp parameters using $D=16\text{ps/nm/km}$ . Solid and dashed curves correspond to super-Gaussian and Gaussian pulse shape (adapted from [46]). ....	53
Fig.3.3 Variation of maximum fiber length with chirp parameter $C$ . The BD product shown is assuming a bit rate of 4Gbps (adapted from [46]). ....	54

Figure	Page
Fig.3.4 (a) Measured dispersion penalty versus modulator chirp parameter in 5Gbps transmission system using external $LiNbO_3$ modulator with adjustable chirp, (b) eye-patterns at 256km for different chirp parameters (adapted from [53]).	55
Fig.3.5 Schematics of MEMS based TDC (adapted from [8]).	56
Fig.3.6 Schematic of the MEMS actuator and mirror: (a) No voltage applied. (0 [V]) (b) Voltage applied (100 [V]). (adapted from [8]).	56
Fig.3.7 Schematic of multicavity etalon TDC. The etalons have a reflective interface between each cavity with only $R_1$ being close to 100% reflective. (adapted from [10-11]).	57
Fig.3.8 Optical coupling configuration for multicavity etalon based TDC. (adapted from [10-11]).	57
Fig.3.9 Schematic of chirped reflective FBG based TDC.	58
Fig.3.10 Schematic layout of the WGR based TDC using pulse shaper concept (adapted from [25]).	58
Fig.3.11 Schematic of VIPA based optical TDC.	59
Fig.3.12 Conceptual diagram of quadratic phase applied to incident wave spectrum by SLM in a VIPA based optical TDC.	60
Fig.3.13 Schematic diagram of BER test set-up.	61
Fig.3.14 Example of typical BER curve (BER vs received power).	61
Fig.3.15 Example of typical eye diagrams : (a) For Non-Return-to-Zero (NRZ) signals. (b) For Return-to-Zero (RZ) signals.	62
Fig.3.16 Experimental set-up for TDC.	63

Figure	Page
Fig.3.17 Electric-to-Optical (E/O) converter module : (a) For $LiNbO_3$ external modulator. (b) For directly modulated laser.....	63
Fig.3.18 TDC measurements using positively chirped 10-Gbps NRZ ( $2^{31}$ -1) source (a) BER characteristics before compensation without TDC. “B2B VIPA” denotes the case for 0km transmission in Fig.3.16 with TDC set to apply zero (flat) phases for entire wavelength. (b) BER characteristics after compensation for different SMF fiber spans.....	65
Fig.3.19 Eye diagrams before TDC compensation for a positively chirped 10-Gbps NRZ ( $2^{31}$ -1) source (a) Back-to-Back (B2B). (b) After 20km SMF transmission. (c) After 40km SMF transmission. (d) After 60km SMF transmission. (e) After 120km SMF transmission. (f) After 240km transmission. ....	66
Fig.3.20 Eye diagrams after optimum TDC compensation for a positively chirped 10-Gbps NRZ ( $2^{31}$ -1) source. (a) 20km SMF transmission and compensation (-340 ps/nm). (b) 40km SMF transmission and compensation (-680 ps/nm). (c) 60km SMF transmission and compensation (-1020 ps/nm). (d) 120km SMF transmission and compensation (-2040 ps/nm). (e) 240km SMF transmission and compensation (-4080 ps/nm). ....	67
Fig.3.21 BER curves for a positively chirped 10-Gbps NRZ source transmitted along the various DCF spans with and without TDC compensation. ....	68
Fig.3.22 Eye diagrams of DCF transmission and compensation (a) 4.8km DCF transmission without TDC compensation. (b) 9.5km DCF transmission without TDC compensation. (c) 4.8km DCF transmission and compensation (+425 ps/nm). (d) 9.5km DCF transmission and compensation (+850 ps/nm). ....	69
Fig.3.23 BER curves for a positively chirped 10-Gbps NRZ source transmitted along 240km SMF and compensated by TDC for several adjacent 50-GHz spaced ITU wavelength channels around 1550nm (1550.12, 1550.52, 1550.92, 1551.32nm).....	70

Figure	Page
Fig.3.24 BER curves for a positively chirped 10-Gbps NRZ source transmitted along 240km SMF and compensated by TDC for five different polarization states (arbitrary elliptical, linear horizontal, linear vertical, linear 45-degrees, left hand circular).....	71
Fig.3.25 (a) VIPA based TDC Transmission spectra with different dispersion settings ranging (from -4080 ps/nm to +4080 ps/nm). (b) Same figure as Fig. 3.25(a) with expanded axis.....	73
Fig.3.26 (a) Measured phase response with different dispersion settings (from -2000 ps/nm to +2000 ps/nm) for TDC. (b) Experimental Setup.....	74
Fig.4.1 Schematic diagram for the experimental setup for RZ lightwave transmission.....	83
Fig.4.2 TDC transmittance and optical spectrum for the optically generated RZ signal with different pulse durations.....	83
Fig.4.3 TDC measurements using 33% RZ signal source : (a) BER vs received power without TDC. (b) BER vs received power after TDC optimum compensation.....	85
Fig.4.4 TDC measurements : BER vs received power after TDC optimum compensation for 50% RZ signal source.....	86
Fig.4.5 Eye diagrams for 10-Gbps RZ source : (a) For 33% RZ, back-to-back without TDC (measured by 50-GHz PD). (b) For 33% RZ, 100km SMF transmission without TDC. (c) For 33% RZ, 100km SMF transmission with optimum compensation by TDC. (d) For 50% RZ, back-to-back without TDC (measured by 50-GHz PD). (e) For 50% RZ, 100km SMF transmission without TDC. (f) For 50% RZ, 100km SMF transmission with optimum compensation by TDC.....	87

Figure	Page
Fig.A.1 Gaussian beam path within the VIPA and output field at observation plane. ....	99
Fig.A.2 Multiple output field at the VIPA output (observation plane) expressed in terms of propagation axis (z-axis). ....	99
Fig.A.3 Simulated example of VIPA output at the observation plane. ....	100
Fig.A.4 VIPA loss due to finite length of VIPA. ....	101
Fig.A.5 Simulated example of overlapped VIPA output of propagating and reflecting waves at the observation planes. ....	102
Fig.A.6 Setup and observation planes of VIPA based pulse shaper to measure the loss mechanism due to coupling between propagating and reflecting waves. ....	103
Fig.A.7 Convolved intensity for propagating and reflecting waves. ....	103
Fig.A.8 Controllable parameters for the insertion loss mechanisms in VIPA based pulse shaper : relative amount of shift between VIPA DeMux and VIPA Mux ( $d$ ), input beam incident angle ( $\theta_{in}$ ), position of incident beam ( $d$ ). ....	105
Fig.A.9 Simulated results for controlling the relative amount of shift between VIPA DeMux and VIPA Mux ( $\delta$ ). The upper figures are the overlapped intensities of propagating and reflecting waves and the lower figures are the convolved results of propagating and reflecting waves. ....	106
Fig.A.10 Insertion loss for controlling the relative amount of shift between VIPA DeMux and VIPA Mux. The minimum insertion loss occurs at $\delta = 6$ -mm. ....	107
Fig.A.11 Simulated results of intensity of propagating waves for changing incident angle ( $\theta_{in}$ ). ....	108
Fig.A.12 Insertion loss for changing incident angle ( $\theta_{in}$ ). Optimum values of $\theta_{in}$ and $\delta$ are shown. ....	109

## LIST OF ABBREVIATIONS

TDC	Tunable Dispersion Compensator
VIPA	Virtually-Imaged Phased-Array
WDM	Wavelength Division Multiplexing
AWG	Array Waveguide Grating
MEMS	Micro-Electro-Mechanical Systems
SLM	Spatial Light Modulator
NRZ	Nonreturn-to-Zero
RZ	Return-to-Zero
FSR	Free Spectral Range
OCDMA	Optical Code Division Multiple Access
GVD	Group Velocity Dispersion
BER	Bit Error Rate
FBG	Fiber Bragg Grating
PLC	Plannar Lightwave Circuit
WGR	Wavelength Grating Router
FOM	Figure Of Merit
PRBS	Pseudo-Random Binary Sequence
PPG	Pulse Pattern Generator
BERT	Bit Error Rate Tester
CW	Continuous Wave
PC	Polarization Controller
EDFA	Erbium Doped Fiber Amplifier
VOA	Variable Optical Attenuator

## ABSTRACT

Lee, Ghang-Ho Ph.D., Purdue University, August 2006. Demonstration Of Optical Tunable Dispersion Compensation With A Virtually-Imaged Phased-Array Based Pulse Shaper. Major Professor: Andrew M. Weiner.

Tunable dispersion compensation is one of the most essential technologies needed for the next generation fiber optic communication systems. The applications will include replacing various lengths of conventional Dispersion Compensating Fibers (DCF) and compensating residual dispersion after the DCF to meet the tight dispersion tolerances required in 40-Gbps and above based networks. To satisfy the future applications, tunable dispersion compensator (TDC) must provide both positive and negative dispersion as well as large tuning range.

The Virtually-Imaged Phased-Array (VIPA) may be considered as a side-entrance etalon device that achieves angular dispersion through multiple beam interference. To our knowledge, we introduced the first VIPA based programmable Fourier transform pulse shaper in the application of optical pulse manipulation in the femtosecond time scale. Here we extend the application of VIPA based pulse shaper to TDC for fiber optic communication systems. Although many TDCs have been demonstrated with various technologies, their tunability is limited to relative small ranges or only provide single wavelength channel compensation.

This thesis covers development and demonstration of the VIPA based pulse shaper in the application of TDC which provide WDM-capability, polarization independence, and large tuning range in both positive and negative directions (largest for optical TDC, to our knowledge). The fiber optic transmission system with various modulation formats has been used to evaluate TDC characteristics.

## 1. INTRODUCTION

Tunable dispersion compensation is essential for the next generation fiber optic communication systems. There is a trend away from the static, passive fiber devices towards tunable devices that will allow system designers to cope with the shrinking system margins and with the rapidly emerging reconfigurable optical networks. The important aspect of optical systems and network that make tunable dispersion compensation solution attractive include : significantly reducing the inventory of different required types of compensation modules, tuning capability to adapt to routing path changes in a reconfigurable networks, tracking dynamic changes in dispersion due to environment, and achieving a high degree of accuracy necessary for 40-Gbps and above systems. To satisfy future applications, tunable dispersion compensator (TDC) must also provide WDM capability, polarization independence, large tuning range, and capability to provide both positive and negative dispersion [1].

Pulse shaping which allows for manipulation of femtosecond optical pulses according to user needs is now a well established technique. The most widely adopted pulse shaping method, Fourier transform pulse shaping, uses a pair of diffraction gratings as spatial dispersers, a pair of Fourier transform lenses to separate the optical spectrum, and a spatial mask or modulator array to manipulate spatially dispersed optical frequency components in parallel [2-3]. This technique is now applied in fields ranging from optical communications to coherent control of quantum mechanical motions to optical pulse compression at the few cycle level. For applications in optical communications, for example, there is interest in extending pulse shaping to larger time apertures, which requires higher spectral resolution. This requires larger spectral dispersion compared to diffraction gratings. One possibility that has been reported involves using modified Arrayed Waveguide Grating (AWG) structures. Some of the early papers, Tsuda et al.,

discussed how AWGs could support larger time apertures [4-5]. Another possibility, which is presented in this work, is to use the Virtually Imaged Phased Array (VIPA) as the spatial disperser. The VIPA may be considered as a side-entrance etalon device that achieves angular dispersion through multiple beam interference. The VIPA has advantages compared to conventional dispersers, like diffraction gratings, such as polarization insensitivity, compactness, larger angular dispersion, potential for finer spectral resolutions, and potentially low cost [6-7].

Many TDC technologies have emerged that meet some or most of the above requirements including MEMS [8], Gires-Tournois etalons [9-13], fiber Bragg grating [14-23], planar lightwave circuits [24-30], and virtually imaged phased array (VIPA) [31-33]. However the tuning range of these works is limited to  $\pm 800$  ps/nm [8-13, 17-18, 24-26, 28, 32-33] or only provides negative dispersion [14-16, 19-23, 27-30]. Several of TDC technologies [8, 24-26, 32-33] employed an optical signal processing approach based on parallel phase control of spatially dispersed optical frequency components [3]. The first demonstration of this approach for programmable fiber dispersion compensation was performed for subpicosecond pulses using a liquid crystal spatial light modulator (SLM) for phase control [34].

In this work we employ a similar optical signal processing approach for TDC using a VIPA and SLM arranged in a reflective pulse shaper geometry [35]. We demonstrate tunable dispersion compensation of 10-Gbps positively chirped nonreturn-to-zero (NRZ) data signals and 10-Gbps return-to-zero (RZ) with different pulse durations, with capability for 50-GHz spaced WDM and polarization independence.

This work is organized in the following manner. In Chapter 2, we discuss the application of VIPA based programmable Fourier transform pulse shaper in the optical pulse manipulation in femtosecond time scale. We show the intensities of the individual pulses in the burst are determined by a temporal envelope function obtained from the inverse Fourier transform of the applied spatial phase function which is predictable. In Chapter 3, we start with basic principles of the pulse propagation by introducing wave equations, dispersion in the fiber, and frequency chirp in the optical transmission system.

Some examples of previous work on the tunable dispersion compensation are explained. Then, we demonstrate tunable dispersion compensation of 10-Gbps positively chirped nonreturn-to-zero (NRZ) data signals over a range of  $-4080 \sim +850$  ps/nm (240km SMF to 9.5km DCF), with capability for 50-GHz spaced WDM and polarization independence using a VIPA based programmable Fourier transform pulse shaper. In Chapter 4, we extend our work to demonstrate tunable chromatic dispersion compensation for 10-Gbps Return-to-Zero (RZ) signal transmissions (a string of binary data with optical pulses that do not occupy the entire bit period and has improved immunity to fiber nonlinearities relative to NRZ), with different pulse durations ( $\sim 33\%$  RZ and  $\sim 50\%$  RZ) with standard SMF upto 100-km ( $-1700$ ps/nm) using a VIPA based programmable Fourier transform pulse shaper. In Chapter 5, we will summarize.

## 2. VIPA BASED PULSE SHAPER

This chapter describes the concept of Virtually Imaged Phased Array (VIPA) and the VIPA based pulse shaper which will be used as optical tunable dispersion compensator (TDC) for DWDM transmission experiments in later chapters. The design and experimental results of manipulating optical pulse bursts, which is another application of VIPA based pulse shaper that were accomplished prior to optical TDC application, is also discussed.

### 2.1 Virtually Imaged Phased Array

The VIPA may be considered as a side-entrance etalon device that achieves angular dispersion through multiple beam interference. The VIPA has advantages compared to conventional dispersers, like diffraction gratings, such as polarization insensitivity, compactness, larger angular dispersion, potential for finer spectral resolutions, and potentially low cost [6].

The VIPA is composed by two glass plates, namely incident glass plate and transmission glass plate, with a different reflectivity coating. The incident glass plate has a nearly 100% total reflectivity, except for small window which is anti-reflection coated for optical beam input. The transmission glass plate has typically 95~99% partial reflectivity to transmit a small portion of optical beam out of etalon cavity and reflect the rest of the beam back. Due to the high reflectivity on both sides of glass plates, the injected optical beam experiences multiple reflections within the etalon cavity, thus producing multiple diverging beams through the transmission glass plate. Diverging

beams interfere with each other as they propagate, separating different wavelength component in the beam with respect to output angle. As a result, the VIPA acts as spatial disperser, which separates different wavelength components within the input optical beam at different locations. The schematic of wavelength decomposition with the VIPA and detailed VIPA structure are shown in Fig.2.1(a) and (b), respectively. The name VIPA came from the fact the apparatus produces many beams diverging from individual virtual images of the beam waist at the output as shown in Fig.2.1(b).

Fig.2.2 shows an example of relation between the output angle and the wavelength obtained by VIPA [6-7]. The angular dispersion is approximately  $2nt/d\lambda$ , where  $t$  is the thickness of the glass plate,  $d$  is the displacement of the virtual images determined by input beam incident angle  $\theta$ ,  $n$  is the refractive index of glass plate and  $\lambda$  is the operating wavelength. More accurate and exact expressions on angular dispersion can be found in [7]. The wavelength spacing, which is equal to the Free Spectral Range (FSR), is determined by the thickness of the plate  $t$ . The example on Fig.2.2 is obtained by an experiment using  $t = 100\mu\text{m}$ ,  $\theta = 6.4$  deg,  $d = 22.4\mu\text{m}$ , and  $n = 1.5$  which result in angular dispersion of  $0.4 \sim 0.8$  deg/nm, and the wavelength spacing of 8nm.

## 2.2 VIPA Based Pulse Shaper Design

Pulse shaping is a powerful tool for ultrafast scientific studies and optical communications [2-3]. The applications of pulse shapers include optical pulse manipulations [4, 35-40], dispersion compensation [5, 41], and optical encoding [42].

Fig.2.3 shows the generic layout of a Fourier transform pulse shaper [35]. It consists of a pair of spatial dispersers, a pair of lenses in  $4f$  configuration, and a spatial mask. The frequency (wavelength) components within the incident pulse are angularly dispersed by the first spectral disperser, and then focused to small diffraction-limited spots at the Fourier plane, where the frequency components are spatially separated along one dimension. Essentially the first focal lens performs a spatial Fourier transform, which

converts the angular dispersion from the disperser to a spatial separation at the Fourier plane. A spatial mask or a spatial light modulator is placed in this plane to manipulate the spatially dispersed optical frequency components. After manipulation by the spatial mask, the second lens and spatial disperser pair recombine all the frequency components into a single collimated beam. The resulting output pulse shape is determined by the Fourier transform of the spatial mask pattern.

The spectrum of the pulse emerging from the Fourier transform pulse shaper can be written as

$$E_{out}(\omega) = E_{in}(\omega) \cdot H(\omega) \quad (2.1)$$

where  $E_{out}(\omega)$  and  $E_{in}(\omega)$  are the complex spectral amplitudes of the output and the input fields, respectively, and  $H(\omega)$  is the frequency response function of the filter synthesized via the pulse shaper. For a pulse shaper with a grating as the spectral disperser, the applied filter transfer function is related to the spatial mask function by [36]

$$H(\omega) = \int dx M(x) \cdot \exp(-2(x - \alpha\omega)^2 / w_0^2) \quad (2.2)$$

where  $M(x)$  is the spatial mask function as a function of spatial position  $x$ ,  $\alpha$  denotes the spatial dispersion, and  $w_0$  denotes the beam radius of individual frequency components at the Fourier plane. For the phase-only mask, the spatial mask function can be expressed as

$$M(x) \sim \exp(-i\Phi(x)) \quad (2.3)$$

The shaped pulse in time domain can be obtained by performing the Fourier transform on Eq. (2.1), and is given by

$$e_{out}(t) = e_{in}(t) * h(t) \quad (2.4)$$

where  $e_{out}(t)$ ,  $e_{in}(t)$ , and  $h(t)$  are the inverse Fourier transform of  $E_{out}(\omega)$ ,  $E_{in}(\omega)$ , and  $H(\omega)$ .

For the conventional grating based Fourier transform pulse shaper, the spectral filter function  $H(\omega)$  is essentially a scaled version of the spatial mask function  $M(x)$  as illustrated in Eq. (2.2). But for the VIPA based Fourier transform pulse shaper, in which VIPA replaces the grating as spectral disperser, new behavior arises due to the properties of the VIPA, namely periodic spectral dispersion.

Fig. 2.4 illustrates schematically the relationship between the realized spectral phase function,  $\Psi(\omega)$ , and the spatial phase function,  $\Phi(x)$ , for the VIPA Fourier transform pulse shaper. Fig. 2.4(a) shows an example of the VIPA response (angular dispersion) with frequency  $\omega$  as function of the spatial position  $x$  at the Fourier plane. The key point is that the VIPA exhibits many closely spaced diffraction orders. The phase shift  $\Phi(x_0)$  imparted by the spatial mask at spatial position  $x_0$  in the Fourier plane determines the phases at frequencies  $\omega_1$ ,  $\omega_2$  and  $\omega_3$  in the spectral plane, i.e.,  $\Psi(\omega_1) = \Psi(\omega_2) = \Psi(\omega_3) = \Phi(x_0)$ . Fig. 2.4(b) shows an example of a single period quadratic spatial phase function,  $\Phi(x)$ , applied at the Fourier plane by a spatial mask. Fig. 2.4(c) is the resulting periodic quadratic spectral phase function,  $\Psi(\omega)$ , applied to input spectrum.

Approximating the VIPA spectral dispersion within a single diffraction order as linear, we can write Eq. (2.1) as

$$\begin{aligned} E_{out}(\omega) &= E_{in}(\omega) \cdot H(\omega) \\ &= E_{in}(\omega) \cdot \left[ \sum_k S(\omega - k\Delta\omega) \right] = E_{in}(\omega) \cdot \left[ S(\omega) * \sum_k \delta(\omega - k\Delta\omega) \right] \end{aligned} \quad (2.5)$$

where  $H(\omega)$  is now a periodic function with period  $\Delta\omega$  equal to the VIPA free spectral range.  $S(\omega)$  is the effective filter function for a single free spectral range in frequency, which is directly related to the spatial phase function,  $\Phi(x)$ , via

$$S(\omega) \sim \exp(-i\Phi(\alpha x)) \quad (2.6)$$

The temporal output is obtained by performing inverse Fourier transform of Eq. (2.5), which yields

$$e_{out}(t) \sim e_{in}(t) * \left[ s(t) \cdot \sum_l \delta\left(t - l \frac{2\pi}{\Delta\omega}\right) \right] \quad (2.7)$$

where  $e_{out}(t)$ ,  $e_{in}(t)$ , and  $s(t)$  are the inverse Fourier transform of  $E_{out}(\omega)$ ,  $E_{in}(\omega)$ , and  $S(\omega)$ , respectively. The temporal output,  $e_{out}(t)$ , is proportional to temporal input,  $e_{in}(t)$ , convolved with a set of delta functions spaced by the inverse of the free spectral range ( $2\pi/\Delta\omega$ ). For an input pulse shorter than  $2\pi/\Delta\omega$ , this results in a burst of periodically spaced output pulses. The amplitudes of the individual pulses are determined by the envelope function  $s(t)$ , the inverse Fourier transform of the single-period spectral filter function  $S(\omega)$ .

Fig. 2.5 is a simulated example comparing the results of applying a single period phase function and a periodic phase function (which is the new behavior arising due to the properties of the VIPA). The input optical spectrum  $E_{in}(\omega)$  is same in all cases. Three different phase functions  $\Psi(\omega)$  and resulting output intensity profiles  $I_{out}(t)$  are shown as the middle and right traces, respectively. Fig. 2.5(a) shows the result when no phase is applied to the input spectrum ( $\Psi_a(\omega)=0$ ). The resultant output pulse,  $I_{a,out}(t)$ , is a single narrow pulse centered at zero delay in the temporal window. Fig. 2.5(b) shows the result when a single period quadratic phase function,  $\Psi_b(\omega)$ , is applied to the input spectrum. The resultant output pulse,  $I_{b,out}(t)$ , is broadened in the time domain and chirped compared to the result in Fig. 2.5(a). Fig. 2.5(c) shows the result for the VIPA based pulse shaper, i.e. when a periodic quadratic phase function,  $\Psi_c(\omega)$ , is applied to the input spectrum. Instead of a single broadened pulse as in Fig. 2.5(b), a burst of identical pulses with different amplitudes is generated as shown in  $I_{c,out}(t)$ . For the VIPA Fourier transform pulse shaper, the periodic spectral phase function,  $\Psi(\omega)$ , similar to the one shown in the middle trace of Fig. 2.5(c), can be generated automatically from a

nonperiodic spatial phase function,  $\Phi(x)$ , provided that the input bandwidth exceeds the VIPA free spectral range. This allows us to perform experiments in which we generate optical pulse bursts and manipulate the envelopes of their bursts via pulse shaper control.

### 2.3 Optical Pulse Burst Manipulation Using VIPA Based Pulse Shaper

Fig.2.6 shows the schematic diagram of the experimental set up. The Fourier transform pulse shaper in Fig.2.3 was modified to a reflective geometry for simplicity, due to symmetry in the geometrical configuration, by inserting a mirror at the Fourier plane after the SLM (spatial mask) and separating the input and the reflected output by a circulator. An erbium fiber ring laser producing 250fs pulses with a repetition rate of 50-MHz centered at 1545nm with 12nm bandwidth was used as the source. By using a fiber collimator and a semicylindrical lens, the source is fed into the VIPA. The air spaced VIPA, with FSR of 400-GHz, spatially disperses the line-focused different frequency (wavelength) components of the source. The spatially dispersed frequency components are focused at the Fourier plane, where the SLM is located, by using a 190mm focal length lens. The SLM at the Fourier plane modulates the phases of individual wavelength components according to desired phase function,  $\Phi(x)$ . For the reflected path, the lens and the VIPA recombine the phase modulated frequency components into a single output beam which is coupled back into the fiber.

The SLM is a standard liquid crystal modulator array composed of 128 elements with dimensions of 2mm by 100 $\mu$ m per elements and having roughly 3 $\mu$ m gap between each element. The SLM was programmed to apply a desired phase function,  $\Phi(x)$ , by a laboratory computer through a controller. We have applied both continuous gray level phase modulation and discrete binary level phase modulation to the SLM.

Other design parameters used in the experimental setup include the focal length of semi-cylindrical lens (~10mm), and the input angle into the VIPA (~5 degrees). The total spatial spread of the incident spectrum on the SLM at the Fourier plane was 4.0mm

(corresponds to VIPA FSR : 3.2nm), which covers 40 SLM pixels. In most of our experiments, the SLM was programmed to provide quadratic and cubic phase functions,  $\Phi(x)$ , by using 40 adjacent discrete pixels within the SLM. The spatial phase function programmed onto the SLM can be written as

$$\Phi(n) = \phi_{quad} \left( n - \frac{N_{BW}}{2} - N_{q,shift} \right)^2 + \phi_{cubic} \left( n - \frac{N_{BW}}{2} - N_{c,shift} \right)^3 \quad (2.8)$$

where  $\Phi(n)$  is the phase at the  $n$ -th pixel of the programmable SLM and  $n$  varies from 1 to 40. It has same meaning as  $\Phi(x)$ , but with spatial position  $x$  digitized to pixel number  $n$ .  $\phi_{quad}$  and  $\phi_{cubic}$  are the amplitudes of the quadratic and cubic phases involved in pulse shaping operation,  $N_{BW}$  (equal to 40) denotes the total number of pixels,  $N_{q,shift}$  and  $N_{c,shift}$  denote shifts in the applied quadratic and cubic phase functions.

The output of VIPA Fourier transform pulse shaper was connected via fiber to an intensity correlator, using  $\sim 250$  fs reference pulses taken directly after the source input. Dispersion compensated fiber was used to balance the dispersion of the fiber used to relay the pulses to the cross-correlator. To a good approximation, the cross-correlation measurement yields the intensity profiles of the shaped pulse bursts generated by the VIPA Fourier transform pulse shaper.

We have obtained a number of results in manipulation of optical pulse bursts via the periodic phase modulation imparted using the VIPA Fourier transform pulse shaper. Fig.2.7 to Fig.2.9 are the examples. The top traces in these figures are the spectral phase functions,  $\Psi(\omega)$ , which are applied to the input optical spectrum. The middle traces are the experimental cross-correlation measurements of the temporal intensity profiles obtained at the pulse shaper output. The bottom traces are the simulated results obtained by multiplying the input optical spectrum,  $E_{in}(\omega)$ , with the periodic filter transfer function,  $H(\omega)$ , and performing the inverse Fourier transform. The dashed lines on the bottom traces are the simulated temporal envelope functions,  $|s(t)|^2$ , of the optical pulse bursts, which determine the relative intensities of the individual pulses in the generated bursts.

$s(t)$  is obtained by performing the inverse Fourier transform of the single period filter transfer function,  $S(\omega)$ , in eq. (2.5) and (2.6).

Fig.2.7 shows results when a periodic quadratic phase function with a period of 400-GHz (equal to the VIPA FSR) is applied. The cubic phase term is set to zero ( $\phi_{cubic} = 0$ ). The phase function repeats  $\sim 4$  times within the total input optical bandwidth. For Fig.2.7(a) the quadratic phase factor,  $\phi_{quad}$ , is set to 0.005 and  $N_{q,shift} = 0$ . This results in a symmetric quadratic phase variation ranging between zero and  $\pi/2$  within a single period. The resulting output contains three observable pulses consistent with the predicted envelope function shown in the dashed line in the bottom trace. Fig.2.7(b) shows the case when the maximum phase variation is increased to  $\pi$  ( $\Phi_{max}(n) = \pi$ ). The quadratic phase factor,  $\phi_{quad}$ , was increased to 0.01 and other parameters remained same as the case in Fig.2.7(a). The resulting output is burst of five distinct optical pulses. It is clear from Fig.2.7(a) and 2.7(b) that increasing the magnitude of quadratic phase variation broadens the temporal window and increases the number of pulses in the burst. There is some deviation between experimental results (middle trace) and simulated result (bottom trace) of Fig.2.7(b); in particular, the pulse at  $t = 0$  is higher for the experiment than for the simulation. We attribute this to a small phase calibration error for the SLM, since a phase calibration error modifies the modulo- $2\pi$  operation and intensity at  $t = 0$  for the case of large total phase swing. Otherwise the experimental and simulated results are in good agreement.

Fig.2.7(c) and 2.7(d) show cases where the phase functions are spectrally shifted. The spatial phase function within a single period in both cases is given by

$$\Phi(n) = \phi_{quad} \left( n - \frac{N_{BW}}{2} - N_{q,shift} \right)^2 \quad (2.9)$$

where all parameters are the same as the case in Fig.2.7(b), except  $N_{q,shift} \neq 0$ . This yields asymmetric parabolas for the phase function as shown in the top traces of Fig.2.7(c) and Fig.2.7(d). In Fig.2.7(c), the spectral phase function,  $\Psi(\omega)$ , is spectrally

shifted by 300-GHz (2.4nm) which corresponds to 3/4 of a single period (VIPA FSR),  $N_{q,shift} = 3/4 N_{BW} = 30$  pixels. The resulting optical pulse burst is advanced in time by 7.5ps, which is three times the pulse separation (2.5ps). The relatively strong intensity peak at  $t = 0$  for the experimental is, once again, attributed to phase calibration error in modulo- $2\pi$  operation. In Fig.2.7(d), the spectral phase function,  $\Psi(\omega)$ , is spectrally shifted by -200-GHz (-1.6nm) which corresponds to 1/2 of a single period,  $N_{q,shift} = -1/2 N_{BW} = -20$  pixels. The resulting optical pulse burst is delayed by 5.0ps, which is two times the pulse separation. From the results in Fig.2.7, we can see that it is possible to control the number of generated optical pulse bursts by adjusting the quadratic phase factor,  $\phi_{quad}$ , and to shift the optical pulse burst in time by introducing a shift ( $N_{q,shift}$ ) in the quadratic spatial phase function.

Fig.2.8. show the results of applying periodic cubic phase functions. The phase functions are cubic within a single period, i.e.,

$$\Phi(n) = \phi_{cubic} \left( n - \frac{N_{BW}}{2} - N_{c,shift} \right)^3 \quad (2.10)$$

Here the quadratic phase factor,  $\phi_{quad}$ , in equation (8) is set to zero and the cubic phase factor,  $\phi_{cubic}$ , is set to either -0.0005 (for negative cubic) or 0.0005 (for positive cubic) in all cases. The total bandwidth,  $N_{BW}$ , in terms of pixel numbers is equal to 40 as before. The resulting pulse bursts have temporal envelope functions (dotted line in bottom traces) that peak near  $t = 0$  with asymmetric ringing on one side. This is similar to what is observed for single ultrafast pulse with cubic spectral dispersion.

Fig.2.8(a), 2.8(b), 2.8(c) are the cases for a negative cubic phase function ( $\phi_{cubic} = -0.0005$ ) with no shift ( $N_{c,shift} = 0$ ), 1/4 of a period shift ( $N_{c,shift} = 1/4 N_{BW} = 10$  pixels) and 3/8 of a period shift ( $N_{c,shift} = 3/8 N_{BW} = 15$  pixels), respectively. For  $N_{c,shift} = 0$ , the total phase variations within one period is  $2\pi$ . For larger  $N_{c,shift}$ , the total phase variations within one period increases. The resulting temporal envelope functions are all broadened toward negative time. The extent of the temporal envelope functions and the number of

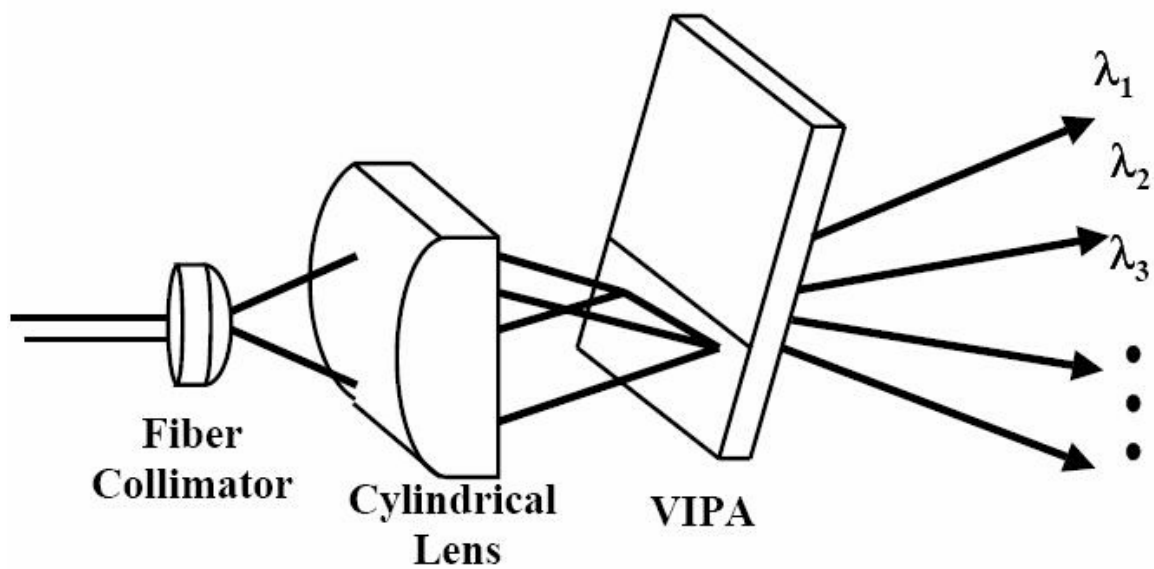
pulses within the burst increases with increasing  $N_{c,shift}$ , as expected when the total phase variation increases.

Fig.2.8(d), 2.8(e), 2.8(f) are the results when positive cubic phase terms are applied. The settings are the same as Fig.2.8(a), 2.8(b), 2.8(c), respectively, except a positive cubic phase factor is applied ( $\phi_{cubic} = 0.0005$ ). The results are similar to those shown in Fig.2.8(a), 2.8(b), 2.8(c), except that the pulse bursts extend toward positive time window. The data in Fig.2.8 demonstrate that we can produce optical pulse bursts on either the positive or negative side of  $t = 0$  by changing the sign of the cubic phase.

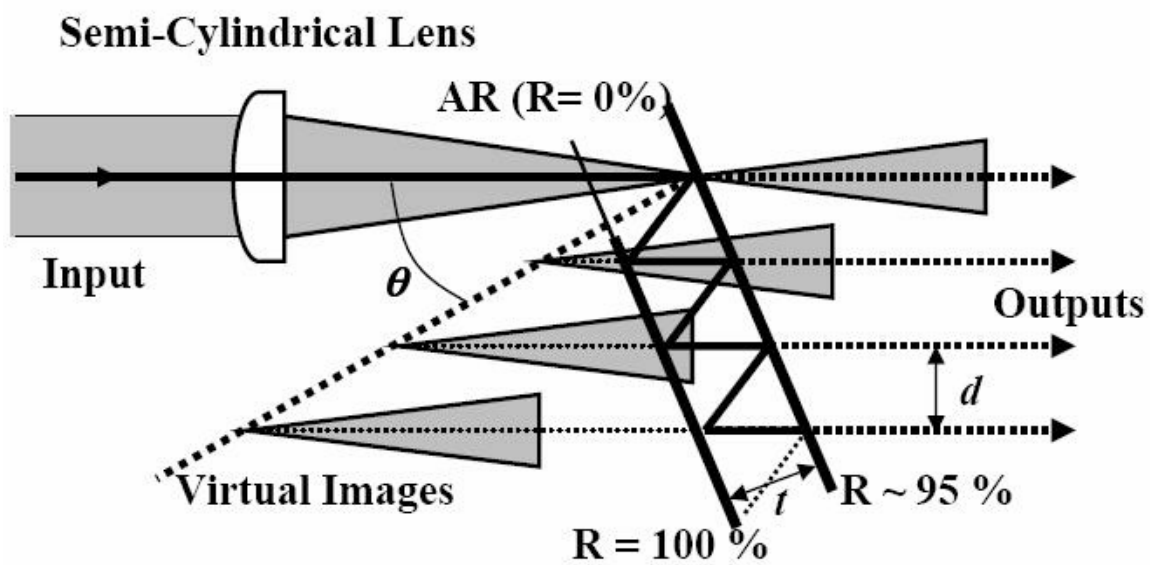
Fig.2.9 shows examples where binary phase patterns are applied instead of the gray level phase functions of Fig.2.7 and Fig.2.8. In particular, we programmed the SLM with m-sequence phase codes. For the binary phase modulation, we applied zero phase,  $\Phi(n) = 0$ , for digit '0' and  $\pi$  phase,  $\Phi(n) = \pi$ , for digit '1'. The m-sequence is a pseudo random binary sequence often used in wireless communications and coding [43]. Due to the periodic spectral dispersion of VIPA, the single m-sequence programmed onto the SLM results in a periodic m-sequence spectral phase function. This results in a pulse burst with the number of pulses in the burst roughly equal to the length of m-sequence code [34]. Fig.2.9(a) and 2.9(b) show the pulse bursts that result when a 7-element m-sequence (digits '0010111') and a 15-element m-sequence (digits '000100110101111') are applied respectively. The number of pulses scales roughly with the length of the m-sequence code, as expected. Results may have application to OCDMA, where pseudo random phase encoding/decoding is often employed [2-3, 36-37, 42].

From the experiment of optical pulse burst manipulation using VIPA based pulse shaper, we have showed the intensities of the individual pulses in the burst are determined by a temporal envelope function obtained from the inverse Fourier transform of the applied spatial phase function. These effects arise specifically because of the periodic spectral dispersion provided by the VIPA and have not been observed with grating based Fourier transform pulse shapers. The experimental data are in good agreement with simulations. The VIPA-based Fourier transform pulse shaping scheme holds promise for programmable optical waveform synthesizers with finer spectral

resolution than conventional grating-based pulse shapers. Furthermore, this work provides evidence that previous experiments on dispersion compensation using VIPAs [6, 31-33, 42] can be understood as an example of pulse shaping.



(a)



(b)

Fig.2.1 (a) Schematic of wavelength decomposition with the VIPA. (b) Details of the VIPA structure.

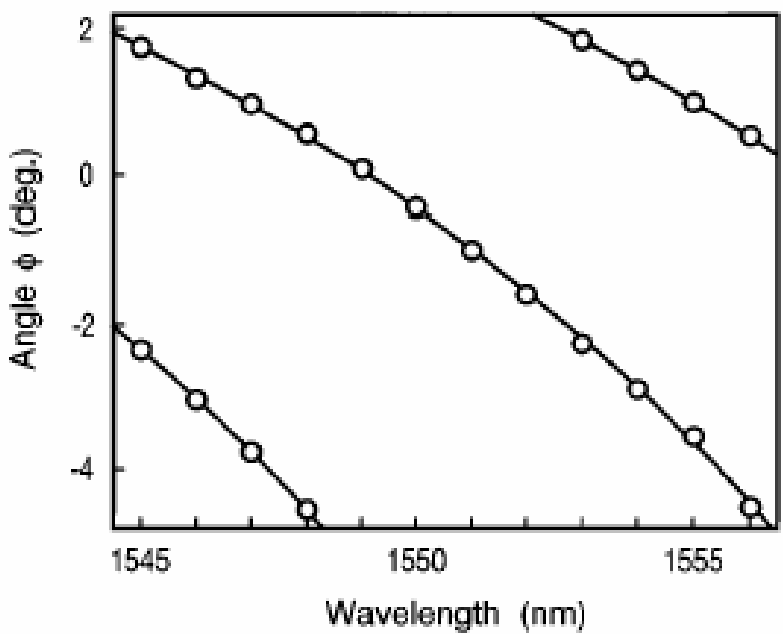


Fig.2.2 Example of relation between angular dispersion and wavelength (adapted from [6]).

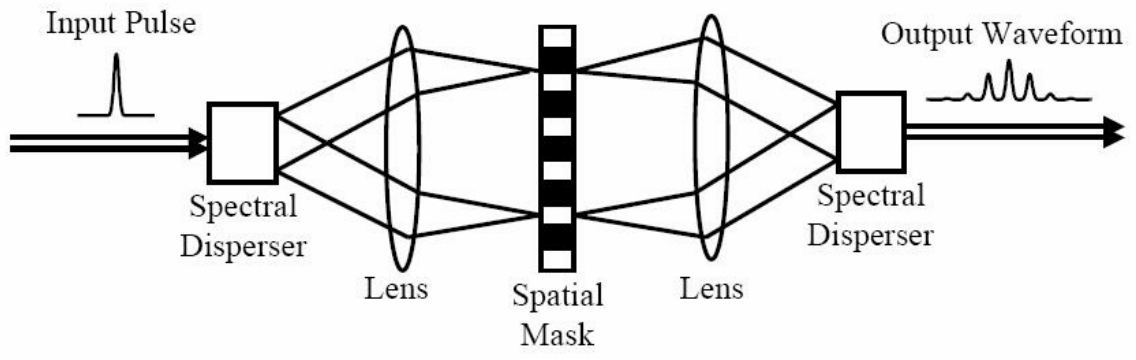


Fig.2.3 Generic layout of the Fourier transform pulse shaper.

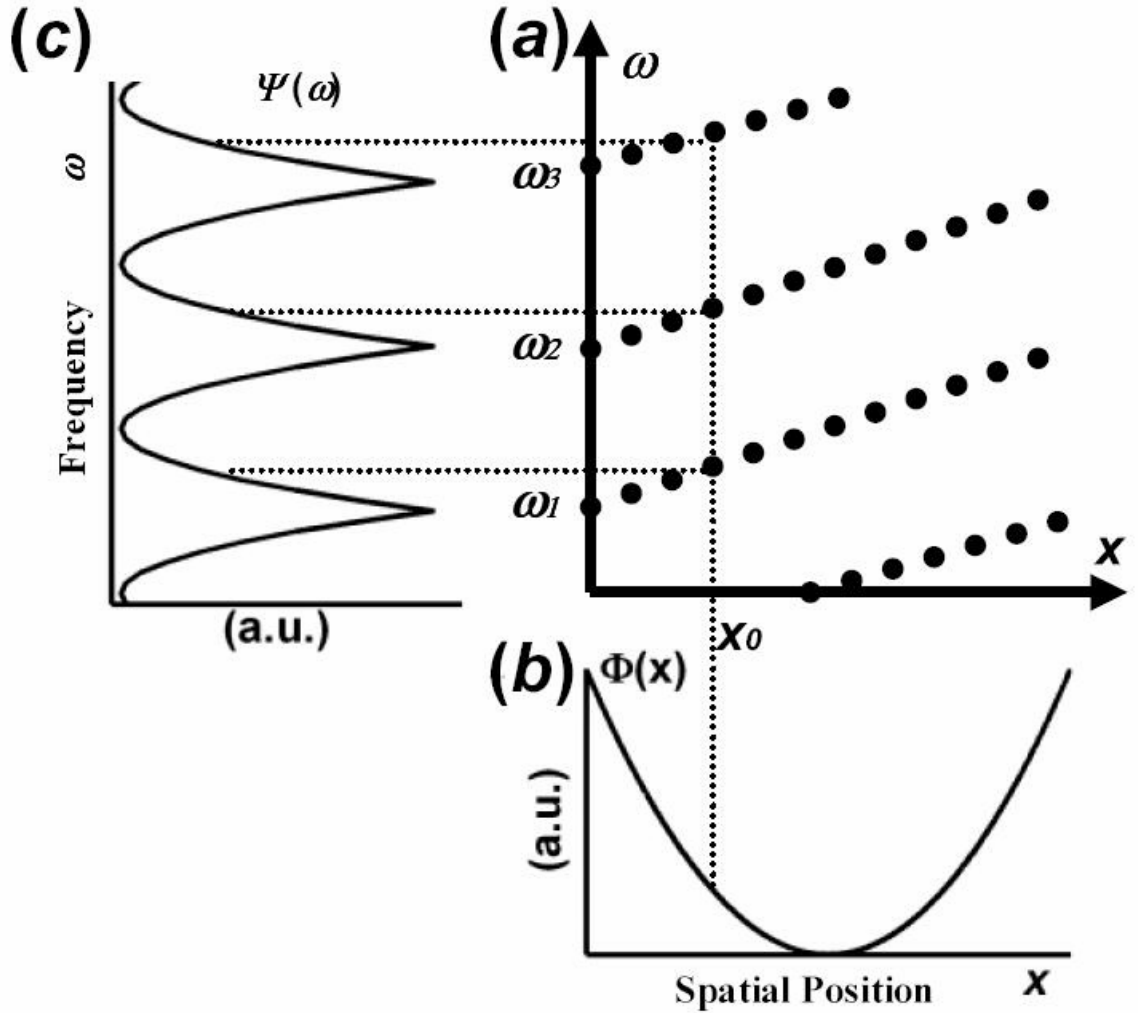


Fig.2.4 VIPA Fourier transform pulse shaper response : (a) Example of VIPA response (angular dispersion) with frequency  $\omega$  as function of spatial position  $x$ . (b) Example of single period quadratic spatial phase function,  $\Phi(x)$ , applied at Fourier plane by spatial mask. (c) Resulting periodic quadratic spectral phase function,  $\Psi(\omega)$ , applied to input spectrum.

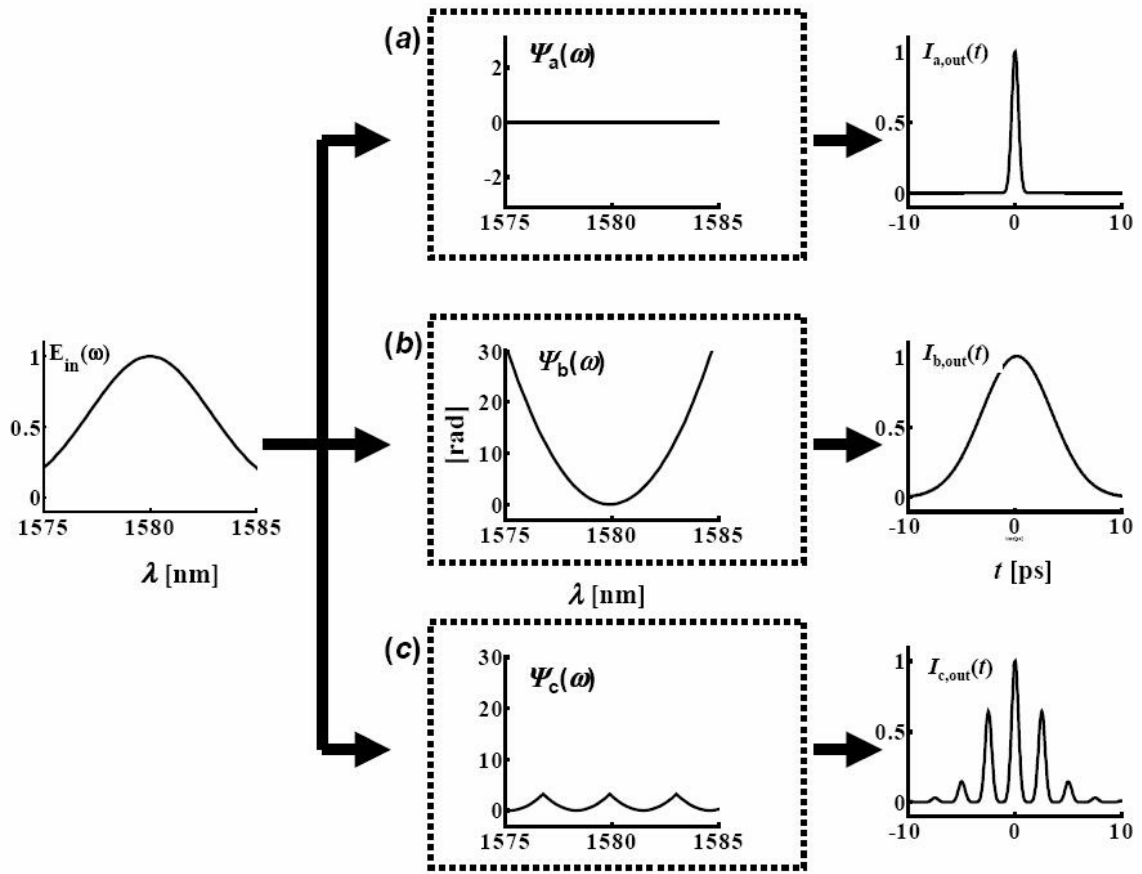


Fig.2.5 Schematic diagram illustrating effect of applying different spatial masks to identical inputs,  $E_{in}(\omega)$ . Input optical spectrum (left trace), applied phase functions (middle traces), resulting output intensity correlations (right traces),  $I_{a,out}(t)$ ,  $I_{b,out}(t)$ ,  $I_{c,out}(t)$  : (a) No phase applied,  $\Psi_a(\omega)$ . (b) Single period quadratic phase function applied,  $\Psi_b(\omega)$ . (c) Periodic quadratic phase function applied,  $\Psi_c(\omega)$ .

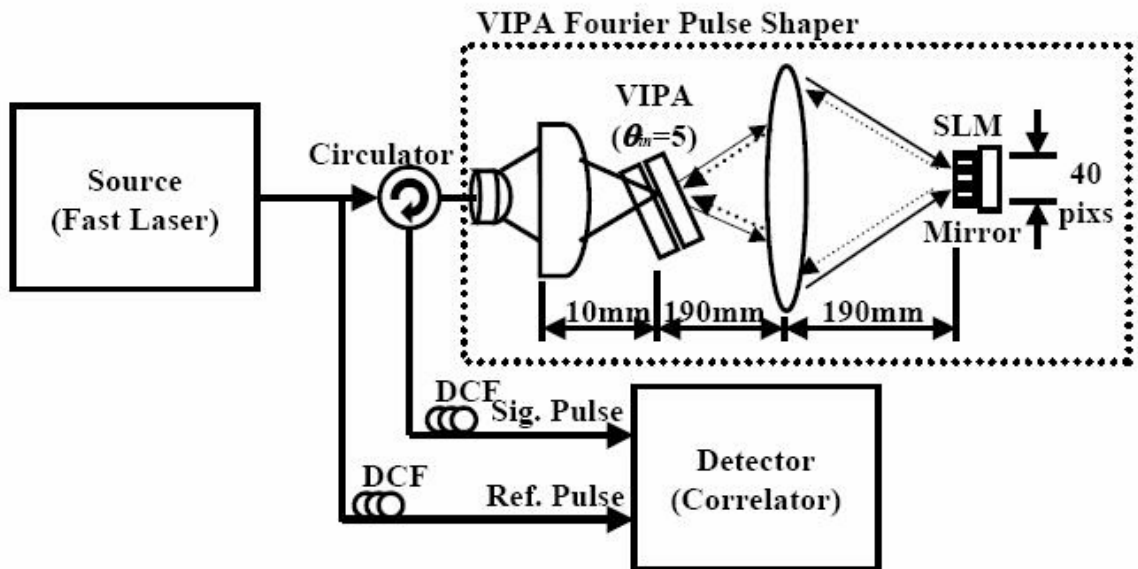


Fig.2.6 Experimental apparatus for programmable Fourier transform pulse shaper based on VIPA.

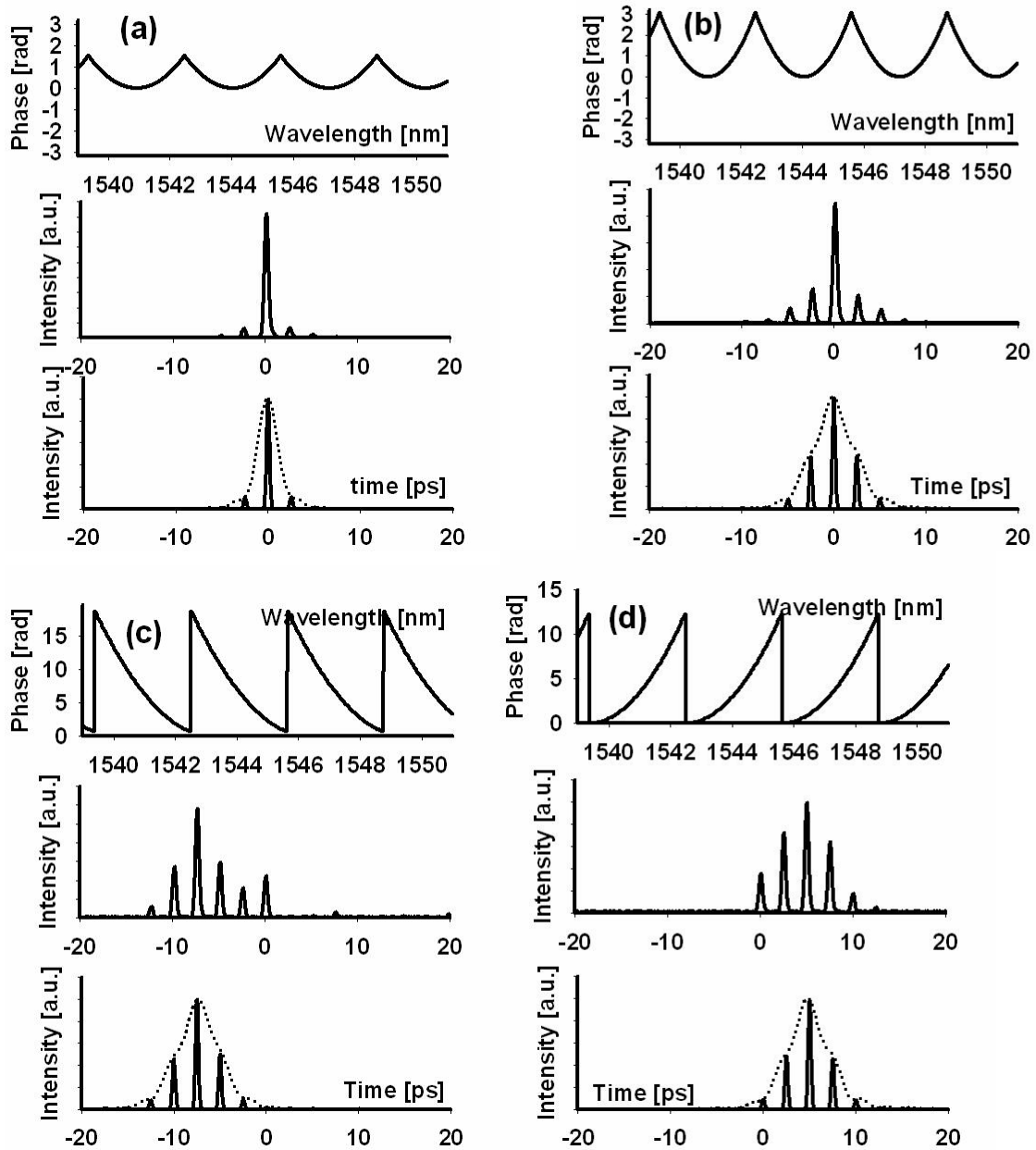


Fig.2.7 Results obtained by applying periodic quadratic phase function with apparatus. Applied phase functions (top trace), resulting output intensity correlation measurements (middle trace), simulated results (bottom trace), dashed line in bottom trace is optical pulse burst envelope function: (a) Phase function varying zero to  $\pi/2$ . (b) Phase function varying zero to  $\pi$ . (c) Phase function spectrally shifted by  $3/4$  of single period. (d) Phase function spectrally shifted by  $-1/2$  of single period.

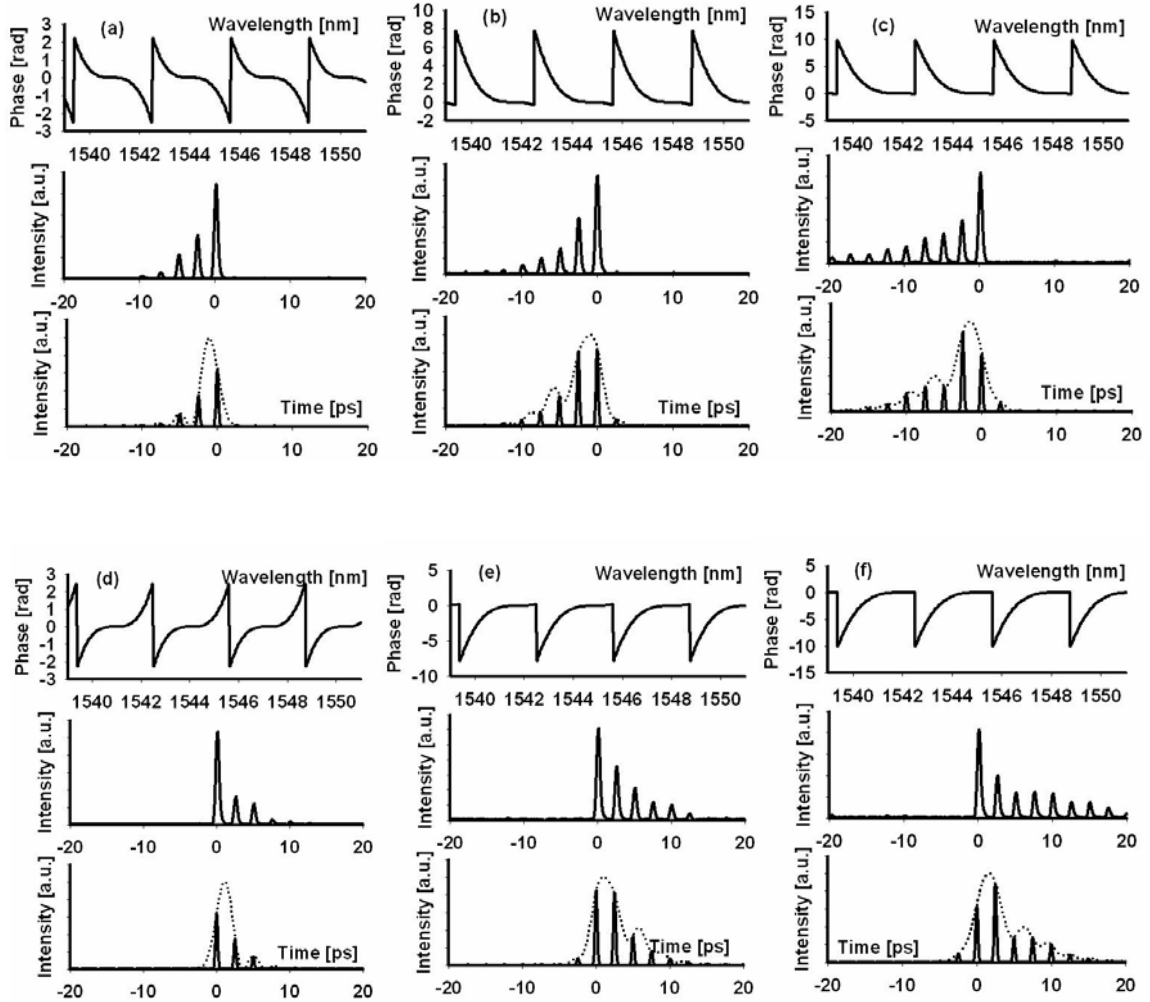


Fig.2.8 Results obtained by applying periodic cubic phase function with apparatus. Applied phase functions (top trace), resulting output intensity correlation measurements (middle trace), simulated results (bottom trace): (a) Phase function varying  $-\pi$  to  $\pi$ , with negative slope ( $\phi_{cubic} < 0$ ). (b) Phase function with negative slope, spectrally shifted by  $1/4$  of single period. (c) Phase function with negative slope, spectrally shifted by  $3/8$  of single period. (d) Phase function varying  $-\pi$  to  $\pi$ , with positive slope ( $\phi_{cubic} > 0$ ). (e) Phase function with positive slope, spectrally shifted by  $1/4$  of single period. (f) Phase function with positive slope, spectrally shifted by  $3/8$  of single period.

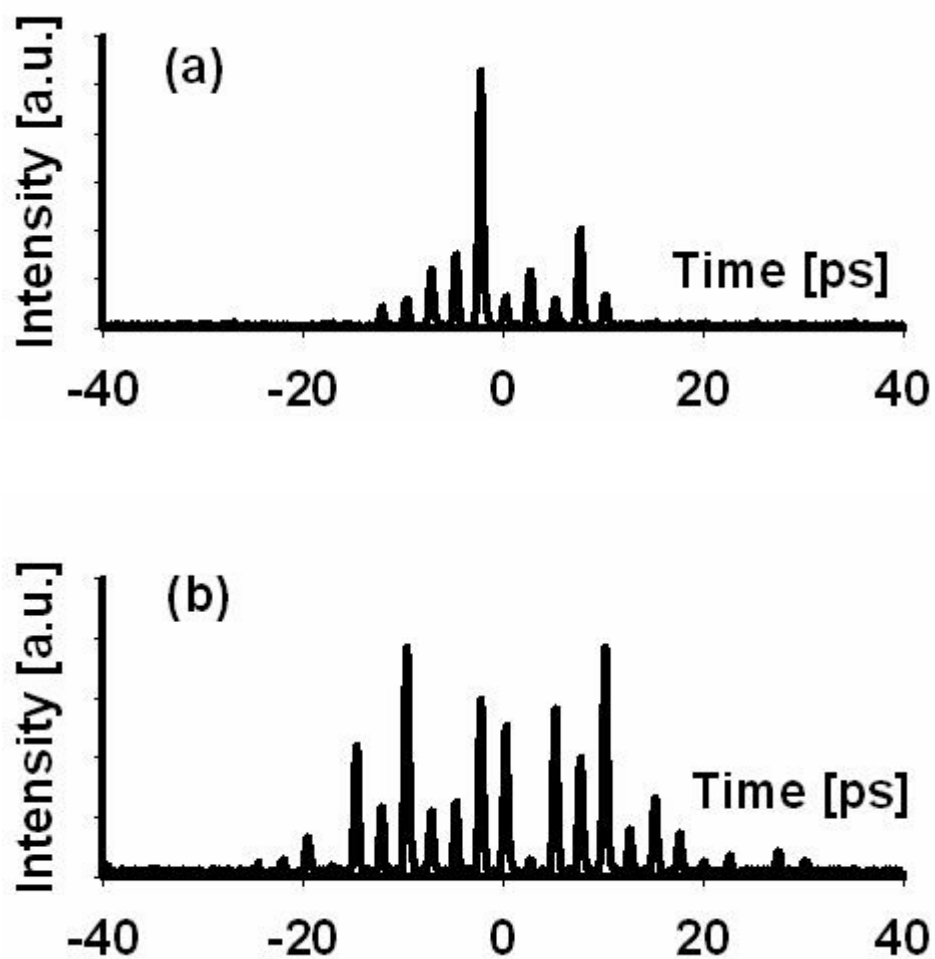


Fig.2.9 Output intensity correlation measurements obtained by applying periodic m-sequence phase function with apparatus. (a) Phase function with 7-element periodic m-sequence (0010111). (b) Phase function with 15-element periodic m-sequence (000100110101111).

### 3. OPTICAL TUNABLE DISPERSION COMPENSATION WITH VIP A BASED PULSE SHAPER

This chapter describes the concept of fiber dispersion, tunable dispersion compensation (including the comparison of previous works on optical TDC), and the experimental setup and results for positively chirped 10-Gbps NRZ signal transmission and compensation using VIP A based optical TDC.

#### 3.1 Fiber Dispersion And Positively Chirped Optical Source

##### 3.1.1 Basic Propagation Equation

The field distribution of wave propagating in a single-mode fiber is obtained by solving wave equation in cylindrical coordinate by making use of cylindrical symmetry of the fiber [44-46].

$$\frac{\partial^2 E_z}{\partial R^2} + \frac{1}{R} \frac{\partial E_z}{\partial R} + \frac{1}{R^2} \frac{\partial^2 E_z}{\partial \phi^2} + n^2 k_o^2 E_z = 0$$

$$E_z = F(R)\Phi(\phi)Z(z) \tag{3.1}$$

Applying  $E_z$  in Eq. (3.1) yields three ordinary differential equations as follow

$$\frac{d^2 Z}{dz^2} + \beta^2 Z = 0$$

$$\frac{d^2 \Phi}{d\phi^2} + m^2 \Phi = 0$$

$$\frac{\partial^2 F}{\partial R^2} + \frac{1}{R} \frac{\partial F}{\partial R} + \left( n^2 k_o^2 - \beta^2 - \frac{m^2}{R^2} \right) F = 0 \quad (3.2)$$

As the solution to the wave equation in Eq. (3.2) is cumbersome, in practice it is approximated by a Gaussian distribution or super Gaussian distribution. The frequency component of the quasi-monochromatic optical field propagating in a single-mode fiber can be expressed as [44-46]

$$\tilde{E}(r, \omega) = \hat{x} F(x, y) \tilde{B}(0, \omega) \exp(i\beta z) \quad (3.3)$$

where  $\hat{x}$  is the polarization unit vector,  $\tilde{B}(0, \omega)$  is the initial amplitude,  $\beta$  is the propagation constant, and  $z$  is the spatial position in the propagating direction.  $F(x, y)$  is the field distribution of the fundamental fiber mode that can be approximated by a Gaussian distribution obtained by Eq. (3.2).

For the pulse propagating in the fiber, pulse broadening results from the frequency dependence of propagation constant  $\beta$ . By expanding  $\beta(\omega)$  in a Taylor series around the carrier frequency  $\omega_0$  and neglecting high-order terms above four yields,

$$\beta(\omega) \approx \beta_0 + \beta_1(\Delta\omega) + \frac{1}{2}\beta_2(\Delta\omega)^2 + \frac{1}{6}\beta_3(\Delta\omega)^3 \quad (3.4)$$

where  $\Delta\omega = \omega - \omega_0$  and  $\beta_m = (d^m \beta / d\omega^m)_{\omega=\omega_0}$  is the m-order dispersion. The amplitude of different spectral components propagating inside the fiber can be expressed as

$$\tilde{B}(z, \omega) = \tilde{B}(0, \omega) \exp(i\beta z) \quad (3.5)$$

The amplitude in the time domain can be obtained by inverse Fourier transform and is given by

$$\begin{aligned}
B(z,t) &= \frac{1}{2\pi} \int_{-\infty}^{\infty} \tilde{B}(z,\omega) \exp(-i\omega t) d\omega \\
&= A(z,t) \exp[i(\beta_0 z - \omega_0 t)]
\end{aligned} \tag{3.6}$$

where  $A(z, t)$  is the slowly varying amplitude of the pulse envelope and is given by

$$\begin{aligned}
A(z,t) &= \frac{1}{2\pi} \int_{-\infty}^{\infty} d(\Delta\omega) \tilde{A}(0,\Delta\omega) \times \\
&\quad \exp\left[ i\beta_1 z \Delta\omega + \frac{i}{2} \beta_2 z (\Delta\omega)^2 + \frac{i}{6} \beta_3 z (\Delta\omega)^3 - i\Delta\omega t \right]
\end{aligned} \tag{3.7}$$

where  $A(0,\Delta\omega)$  is the Fourier transform of  $A(0, t)$ . From Eq. (3.7), we have the basic propagation equation for the pulse evolution inside the single-mode fiber by replacing  $\Delta\omega$  by  $i(\partial A / \partial t)$  and solving in terms of  $\partial A / \partial z$  [44-46].

$$\frac{\partial A}{\partial z} + \beta_1 \frac{\partial A}{\partial t} + \frac{i}{2} \beta_2 \frac{\partial^2 A}{\partial t^2} - \frac{1}{6} \beta_3 \frac{\partial^3 A}{\partial t^3} = 0 \tag{3.8}$$

### 3.1.2 Dispersion In Single Mode Fiber

In the single-mode fiber, the group velocity for the fundamental mode is frequency dependent. The different spectral components of the pulse travel at slightly different group velocities, a phenomenon called the Group Velocity Dispersion (GVD) occurs which results in pulse broadening. The effect of GVD can be explained by using group delay per unit length,  $T(\omega)$ , defined as inverse of group velocity [44-45, 47].

$$T(\omega) = \frac{1}{v_g} = \frac{\partial \beta(\omega)}{\partial \omega} = \beta_1 + \beta_2 (\Delta\omega) + \frac{1}{2} \beta_3 (\Delta\omega)^2 \tag{3.9}$$

where  $\Delta\omega = \omega - \omega_0$  and  $\omega_0$  is the center carrier frequency. As the frequency  $\omega$  moves away from the center carrier frequency  $\omega_0$ , the group delay deviate from  $\beta_1$  which indicates dispersion. Also if pulse width decreases, due to increasing bit rate, spectral spread  $\Delta\omega$  increases and group velocity spread also increases indicating more severe dispersion. The dispersion can also be expressed in terms of the variation in the group delay with respect to the wavelength given as

$$D(\lambda) = \frac{\partial T(\omega)}{\partial \lambda} = D(\lambda_0) + \frac{\partial D(\lambda_0)}{\partial \lambda} \Delta\lambda + \dots \quad (3.10)$$

where  $\Delta\lambda = \lambda - \lambda_0$  and  $\lambda_0 = 2\pi c/\omega_0$  is the center wavelength. The first and second term on right hand side are called dispersion parameter and second-order dispersion parameter (or dispersion slope parameter), respectively and they are given as

$$D = -\frac{2\pi c}{\lambda^2} \beta_2$$

$$S = \frac{\partial D}{\partial \lambda} = \left(\frac{2\pi c}{\lambda^2}\right)^2 \beta_3 + \left(\frac{4\pi c}{\lambda^3}\right) \beta_2 \quad (3.11)$$

The dispersion parameter  $D$  is expressed in units of ps/(nm-km). The dispersion slope parameter  $S$  is in units of ps/(nm<sup>2</sup>-km).

We can relate time delay  $\Delta T$ , which is the extent of pulse broadening for a fiber length  $L$ , with the transmission bit rate  $B$ . The time delay should be less than the allocated bit slot  $T_B = 1/B$ . So the condition for this will be  $B\Delta T < 1$ , which indicates  $BL$  product (limiting bit rate-distance product).

$$B\Delta T = BL|D|\Delta\lambda < 1$$

$$B\Delta T = BL|S|(\Delta\lambda)^2 < 1 \quad (3.12)$$

For  $\beta_2 > 0$  ( $D < 0$ ) it is called normal dispersion regime, where as for  $\beta_2 < 0$  ( $D > 0$ ) it is called anomalous dispersion regime. In the normal dispersion regime, high-frequency (blue-shifted) components of an optical pulse travel slower than the low-frequency (red-shifted) components of the same pulse. In the anomalous dispersion regime it is the opposite. Both dispersion regimes broaden the initial pulse. The dispersion slope  $\beta_3$  can be neglected when  $|\beta_2|$  exceeds  $1 \text{ ps}^2/\text{km}$  [44-46].

When dispersion slope is neglected ( $\beta_3 = 0$ ), the solution to the propagation equation for the pulse evolution inside the single-mode fiber in Eq.(3.7) can be rewritten as

$$A(z,t) = \frac{1}{2\pi} \int_{-\infty}^{\infty} d(\Delta\omega) A(0,\Delta\omega) \exp\left[\frac{i}{2}\beta_2 z(\Delta\omega)^2 - i\Delta\omega t\right] \quad (3.13)$$

The initial pulse amplitude is obtained by performing inverse Fourier transform to the factor  $A(0, \Delta\omega)$  in Eq.(3.13), and it can be approximated by super-Gaussian model given by

$$A(0,t) = A_0 \exp\left[-\frac{1}{2}\left(\frac{t}{\sigma}\right)^{2m}\right] \quad (3.14)$$

where  $A_0$  is the peak amplitude,  $\sigma$  is the half-width (at  $1/e$  intensity point).

The dispersion induced degradation is due to the phase factor  $\exp[i\beta_2 z(\Delta\omega)^2/2]$ , or frequency chirp, in Eq. (3.13) obtained during the propagation along the fiber. The degradation induced by dispersion may be compensated by several ways, depending on the applications, using dispersion shifted fiber, low-chirp transmitters, soliton propagation and dispersion equalization. All these dispersion compensation schemes attempt to cancel the phase factor  $\exp[i\beta_2 z(\Delta\omega)^2/2]$ .

### 3.1.3 Positively Chirped Optical Source

The optical pulse emitted from the semiconductor laser exhibit considerable chirp, when it is directly modulated (positively chirped). The direct amplitude modulation in the semiconductor laser is accompanied by time varying phase. A time varying phase is equivalent to transient changes in the mode frequency from its steady-state value. The pulse having this property is called to have chirp. Taking account for the frequency chirp for direct modulated laser in fiber propagation, the initial pulse amplitude obtained in Eq. (3.14) is modified to [44-46, 48-50]

$$A(0,t) = A_0 \exp \left[ -\frac{1+iC}{2} \left( \frac{t}{\sigma} \right)^{2m} \right] \quad (3.15)$$

where  $C$  is the chirp parameter, which indicates amount of chirp induced in the pulse amplitude.

The chirp of direct modulated lasers can be characterized by the time dependent change in frequency expressed as [48-52]

$$\Delta \nu(t) = -\frac{1}{2\pi} \frac{d\phi}{dt} = \frac{mC}{2\pi\sigma} \left( \frac{t}{\sigma} \right)^{2m-1} = \frac{C}{4\pi} \frac{d}{dt} (\ln P) \quad (3.16)$$

where  $\phi$  is the phase profile in pulse amplitude as in Eq. (3.15) and  $P = |A|^2$  is the modulate optical power. For direct modulated laser the chirp parameter  $C$  is negative (positively chirped), typically -6, where the pulse is blue shifted near the leading edge and red shifted near the trailing edge, as observed experimentally by Linke [50] shown in Fig. 3.1.

Fig.3.1 is the time resolved spectra for a 2ns optical pulse in 100ps steps from a positively chirped optical source. The wavelength is seen to move toward the blue on the

start-up (upper left side) and toward the red on the shut-down (upper right side). The total light is shown versus time in the inset. Fig.3.2 shows the broadening factor, defined as the final-to-initial rms-width ratio as a function of the fiber propagation length for three values of chirp parameters 0, -3, and -5 (corresponds to the linewidth enhancement factors  $\alpha = -C = 0, 3, \text{ and } 5$ ), respectively. Note, when the chirp parameter is negative, it is called positively chirped and when the chirp parameter is positive, it is called negatively chirped. The dashed line corresponds to the linearly chirped Gaussian pulse and solid line corresponds to the super-Gaussian pulse. A super-Gaussian pulse broadens faster than a Gaussian pulses with increase in the fiber propagation length and the situation becomes worse when the chirp parameter increases. The increase in broadening for super-Gaussian pulse is due to the abrupt changes in leading and trailing edges, which broaden the spectrum of the pulses. For the increase in the value of  $\alpha$  (increase in the positive frequency chirp) leads to an additional spectral broadening that further increases the pulse rms-width ratio with propagation.

Fig.3.3 is the dependence of the maximum achievable bit rate-distance (BD) product on the chirp parameter assuming that a pulse broadening of at most 20% can be tolerated. It is the case for the bit rate,  $B = 4\text{Gbps}$  propagating along standard single-mode fiber having dispersion parameter,  $D = 16 \text{ ps/km/nm}$ . It is clear that the system performance depends critically on the numerical values and the sign of the chirp parameter  $C$ . In particular, the BD product is larger when  $C$  is positive (negatively chirped). This is because the negatively chirped pulse undergoes an initial compression in the anomalous dispersion regime ( $\beta_2 < 0, D > 0$ ). However for semiconductor lasers, the chirp profile is positive (generally  $C = -6$ ). The positively chirped optical sources operating in the anomalous dispersion regime (laser center wavelength at  $1.5\mu\text{m}$ , using standard single-mode fiber) induce additional limit in propagation distance.

There are some new approaches in semiconductor lasers to compensate the chromatic dispersion along the fiber transmission by modifying the characteristics of input pulses at the transmitter before they are launched into the fiber link. The underlying idea of this approach can be understood from Eq. (3.13). It consists of changing the

spectral amplitude  $A(0, \Delta\omega)$  of the input pulse in such a way that GVD-induced degradation is eliminated, or at least reduced, substantially. Clearly, if the spectral amplitude is changed as

$$A(0, \Delta\omega) \rightarrow A(0, \Delta\omega) \exp(-i(\Delta\omega)^2 \beta_2 L / 2) \quad (3.17)$$

where  $L$  is the fiber length, GVD will be compensated exactly, and the pulse will retain its shape at the fiber output. Unfortunately, it is not easy to implement Eq. (3.17) in practice. In a simple approach, the input pulse is chirped suitably to minimize the GVD-induced pulse broadening. Since the frequency chirp is applied at the transmitter before propagation of the pulse, this technique is referred to as pre-chirping.

Fig.3.4(a) is an example of measured dispersion penalty for a BER of  $1 \times 10^{-9}$  in a 5Gbps transmission system using an external  $LiNbO_3$  modulator with adjustable chirp [53-54]. For the case of 128km transmission, operation with a chirp parameter of  $\sim 0.8$  reduces the dispersion penalty by 0.7dB. Similarly, at 192km and 256km the dispersion penalties were reduced by 0.5dB and 0.3dB by operating at a chirp parameter of 0.6 and 0.4 respectively. Note that there is a specific value of chirp parameter which minimizes the dispersion penalties at a specific propagation length. Note also that a large value of chirp parameter (large negative chirp) does not improve system performance, but leads to large dispersion penalties. In Fig.3.4(b), the received eye-patterns at 256km for different chirp parameters ( $C = 2, 1, 0,$  and  $-1$ ), are shown. The top trace indicates the eye-pattern at the transmitter. Note that the eye-opening is somewhat larger for negative chirp ( $C = 1$ ) than the chirp-less case ( $C = 0$ ). The eye-closure is severe even for the small value positive chirp ( $C = -1$ ).

## **3.2 The Reason For Tunable Dispersion Compensation**

### **3.2.1 Time Variant Optical Networks**

Fiber chromatic dispersion in optical networks has been considered as a time-invariant phenomenon. The fixed compensation of signal impairments in a “set-and-forget” approach at the time of manufacture and deployment would be expected to perform uniformly well over time. This is certainly the case for the optical networks operating at relatively low bit-rate where dispersion compensation is most often not needed. In scenarios that do not require either accurate compensation or dynamic network conditions, fixed compensation can be considered adequate. This static view is challenged more and more as the performance of optical networks continues to rise and the timescale of the system changes continues to decrease. The shrinking system margins are due to three key systems advances including, higher bit rates, WDM capabilities with narrower channel spacings, and the migration to more complex, time varying network topologies. The small changes that used to be insignificant when compared to the design power margins are now becoming very significant. These changes must now be compensated for to keep the systems operating. In addition, events that used to be viewed as catastrophic, such as restoration in case of failure, are becoming more common as the networks become truly reconfigurable. Therefore, it is not surprising that control of signal impairments in fiber-optic systems has acquired the new dimension of time, and that dispersion compensation has gained tunability as a highly desirable function [1].

### **3.2.2 The Reason For Tunable Dispersion Compensation**

The fixed dispersion compensations are suitable only for relatively low-speed, static systems as explained above. For the future optical communication systems, compensation devices must be tunable due to the following reasons [1]:

1. Inventory management. Even in a static network, distances between dispersion compensation points will vary, depending on the geography of the region and on the traffic requirements. Each fiber link will have a different length, and the chromatic dispersion value of the deployed fiber is only accurate to within some nonzero factory specification. As such, dispersion compensation modules must cover a wide range of compensation values. Any system integration company would need to stock many different modules of a given dispersion compensation module to account for the many values of accumulated chromatic dispersion. When considering inventory reduction, it is highly attractive to stock modules that can be tuned to the desired value, and the deployed interchangeably in a “set-and-forge” fashion. The alternative is to have a large stock of devices covering the whole range of required discrete compensation values or a source for custom devices to match the deployment needs. Similar considerations apply to the management of backup devices for an existing system.
2. Accuracy for  $\geq 40$ -Gbps systems. The required accuracy in dispersion compensation increases dramatically with the signal bit rate. Whereas the amount of residual dispersion that is tolerable at 10-Gbps in a partially-compensated link is approximately 1000 ps/nm, this margin shrinks to only 60 ps/nm for 40-Gbps systems. It is clear that providing highly accurate compensation would require either tunable or custom modules. Otherwise, increasing amounts of residual dispersion will accumulate over cascaded stages of imperfect partial dispersion compensation. The use of tunable modules seems to be the only practical solution for compensating accumulated dispersion with a manageable inventory of modules.

3. Changes in the path length. In a reconfigurable network, as signals are rerouted to avoid traffic congestion or faulty sections, the distance and type of fiber may change. The chromatic dispersion compensation unit at the receiver must follow these changes. It is important to note that even if the fiber spans are compensated periodically, span-by-span, the pervasive use of compensation at the transmitter and receiver suggests that optimization and tunability based on the path will still be needed. Moreover, the span length itself is constantly modified by rework of the network in the form of splicing in case of fiber breakage and repair.
  
4. Environmental effects. Temperature changes can lead to variations in dispersion that may be significant enough to impact the system. In fiber, the zero-dispersion wavelength changes with temperature, at a rate of  $0.03 \text{ nm}/^\circ\text{C}$ . Thus, the relative changes in dispersion is proportional to the magnitude of the slope of the fiber and to the thermal change [55]. Given a temperature change of  $\Delta T = 25^\circ\text{C}$ , a distance of  $L = 500\text{-km}$ , and an SMF dispersion slope of  $D^{(2)} = 0.08 \text{ ps}/(\text{nm}^2\text{-km})$ , the thermally induced variation in dispersion is  $\Delta D = 30 \text{ ps/nm}$ , which corresponds to the accumulated dispersion of  $2\text{-km}$  of SMF or  $7.5\text{-km}$  of NZDSF. This amount is relatively insignificant for  $10\text{-Gbps}$  systems, but is becoming significant for  $40\text{-Gbps}$  systems, where the  $1\text{-dB}$  tolerance is at  $\sim 60 \text{ ps/nm}$ .
  
5. Wavelength drift and filter passband shape. It is quite possible that in any WDM network, various components, such as lasers, filters, and multiplexers will experience wavelength drift. Particularly in the case of SONET rings, there could potentially be many demux/mux pairs that must be traversed by a signal. Now let's consider the filter passband shaper of filter and muxes. In any filter, there is a phase change induced on the transmitted signal if the signal is located off peak and on the sloping roll-off edges of the filter

passband function. A phase change can be thought as a time shift, in picoseconds. This change is taking place across the spectral bandwidth of the signal itself, as measured in nm. Therefore, a signal that passes through a filter but is not located at the peak will suffer from frequency-dependent phase delay (i.e., dispersion), which will then interact with the fiber chromatic dispersion and degrade the signal.

6. Changes in the signal power. As channels are added/dropped in a network or if the transmitter power changes over time, the total power in the fiber will change, thereby changing the effect due to fiber nonlinearities [56]. As the power changes, the optimal dispersion-compensation map may also change, requiring tunability of the dispersion. For  $\geq 40$ -Gbps signals, even self-phase modulation will change the dispersion map sufficiently to require tunable dispersion compensation [57].
7. High performance data formats. Tunability may be quite important when using nontraditional data formats in a system. For example, it has been shown that RZ transmission at 40-Gbps can extend the distance by a factor of two as compared to NRZ [58]. (Moreover, the RZ format is more sensitive to chromatic dispersion.) For this reason, RZ systems may require dynamically adaptive dispersion compensation even when NRZ formats may not.

### **3.3 Previous Works On Optical Tunable Dispersion Compensation**

As explained in previous sections, tunable dispersion compensation is becoming an essential technique in the optical links. Techniques employed for tunable dispersion compensation can be divided into two different sectors. The ones that process the signal after the photodetector or perform dispersion equalization at the transmitter are called

“electrical”. In contrast, techniques that operate on the optical signal directly are termed “optical”. Both types of tunable dispersion compensation techniques (electrical and optical) have received considerable attention in recent years.

In the electrical domain, a transversal filter is commonly employed, and the search for a “smart” equalizer filter capable of operating at bit rates as high as 80-Gbps is continuing [59-62]. The interest in electrical compensation is motivated by the possibility of integrating such a dispersion compensators with the photodetector and other receiver components. The combination of digital signal processing, high speed D/A converters and a complex E-field E/O converter enabled implementation of transmitter based electrical compensation possible. The advantages of the electrical techniques include the possibility of easily and dynamically tuning the amount of dispersion compensation. Beside pure performance, the size of compensators, its power consumption, the effort for adaptation and the cost are important factors in electrical techniques.

In the optical domain, one way to compensate for the dispersion effects is to force the optical signal through a device where spectral components that traveled faster slow down relative to other components. This process can in principle be adjusted to equalize the delay over the entire spectrum of an optical pulse, resulting in full dispersion compensation. The main advantage of using optical TDC are the ability to share the compensators between channels, capability to perform in-line compensations, and the characteristics including independent of power consumption and operating bit-rate. Table 3.1 summarizes advantages and disadvantages of optical and electrical TDC [63].

As both types of tunable dispersion compensation techniques have their own advantages, the best future solution is to combine both techniques. However, as bit rates increase, optical TDC may dominate over electrical TDC, because of their higher performance and lower power consumption. Also, as WDM networks become more complex and dynamic, optical TDCs may replace current DCF spools.

### 3.3.1 Previous Works On Optical Tunable Dispersion Compensation

In this section, we introduce a number of previous approaches on optical TDC including MEMS [8], multicavity etalons [9-13], fiber Bragg grating (FBG) [14-23], and integrated optical devices [24-30].

The implementation of MEMS based TDC requires an optical circulator, a bulk diffraction grating, lenses, and MEMS mirrors, as shown in Fig.3.5. The insertion loss was around  $\sim 10$  dB. It uses pulse shaping concept which was explained in detail in chapter 2 and first demonstrated in [34]. The input beam from a single-mode optical fiber is collimated through the first lens and goes to the bulk diffraction grating. WDM signals are separated to single channels and these signals are separated to angular frequency components, simultaneously by the bulk diffraction grating. Each beam is focused by the second lens onto the MEMS mirrors. The optical phase of each signal is tailored by one of the MEMS mirrors to give appropriate chromatic dispersion. The beams travel back to the lens and the bulk diffraction grating, and are coupled to the optical fiber. The output is separated by the optical circulator. MEMS mirrors are the key parts of this type of TDC. Fig.3.6 shows a schematic of the MEMS actuator and mirror. By changing the applied voltage given to the comb shape field actuator (from 0 to 100 V), the mirror deforms, as shown in Fig.3.6(a) and 3.6(b). Changing the applied voltage from 0 to 100 V, the chromatic dispersion was changed from 4.6 to 16.7 ps/nm having tuning range of  $\sim 12$  ps/nm.

The basic principle of multicavity etalon based TDC is shown in Fig.3.7 [9-13]. It employ two types of multicavity etalon, designed to have a linearly varying dispersion (as a function of wavelength) over a particular bandwidth. Etalon A in the figure is designed to have a negative dispersion slope while etalon B in the figure has a positive slope. The magnitude of the slopes are designed to be either equal to each other or in a simple ratio so that when the appropriate number of reflections is combined, there is a region where the dispersion is constant. The value of the dispersion is determined by the

relative spectral shift between the two etalons, which is controlled by thermoelectric cooler. The glass substrate thicknesses determine the overall device free spectral range (FSR). The end coating reflectivity ( $R_1$ ) is designed to be close to 100% to yield the all-pass transfer function, while the other coating reflectivities vary down to about 0.1%. Optical coupling is achieved using grin lenses with a typical fiber-to-fiber loss per pass of 0.5 dB as shown in Fig.3.8. Fig.3.8 is an example of double-pass the (2A/2B) etalons, yielding 4A-4B reflections. The device has a tuning range of  $-1500 \sim +1700$  ps/nm, 25GHz FSR and the insertion loss of 8.2 dB.

The most widely adopted optical TDC is FBG based TDC [14-23]. FBG has emerged as a powerful technology for dispersion compensation because of their potential for low loss, small footprint, and low optical nonlinearity. Bragg gratings are sections of single mode fiber in which the refractive index of the core is modulated in a periodic fashion as a function of the spatial coordinate along the length of the fiber. When the spatial periodicity of the modulation matches what is known as the Bragg condition with respect to the specific wavelength of light propagating through the fiber core, the periodic structure acts like an efficient mirror, reflecting the optical radiation that is traveling through the core of the fiber. This is known as a uniform grating and ideally reflects a single frequency of light. Such a resonant reflection structure has applications in optical filters, add/drop multiplexers, and optical switches. Most often, the useful part of the signal is that which is reflected from the grating. A three port optical circulator is traditionally used to separate the input and the output ports and enable the reflected wave to be accessed. For reflection based gratings, the transmitted part of the signal can be simply discarded by using an absorbing termination at the far end of the grating. When the periodicity of the grating is varied along the length, the result is a chirped grating, which can be used to compensate for chromatic dispersion. In chirped gratings, the Bragg matching condition for different optical frequencies occurs at different positions along the grating length. Thus, the round trip delay of each frequency can be tailored from the design of the chirp profile. In a data pulse that has been temporally distorted by chromatic dispersion, different frequency components arrive at the FBG with different

amounts of relative time delay. By tailoring the chirp profile such that the frequency components see a relative delay that is the inverse of the accumulated delay of the transmission fiber, the reflected pulse can be compressed. For instance, the frequencies in the leading edge of a pulse are reflected later in the grating and incur a long time delay, whereas the frequencies in the trailing edge of the pulse are reflected in the earlier part of the grating and incur a shorter time delay. The negative dispersion induced by the grating can be characterized by the slope of the time delay when plotted as a function of wavelength, which is related to the grating chirp. The chirp, in turn, is the rate of change of the spatial frequency as a function of position along the grating. This time vs wavelength slope is in units of ps/nm, which is the same as the fiber chromatic dispersion.

To achieve tunable dispersion compensation in a chirped FBG, the slope of the delay curve as a function of wavelength must be altered. Fig.3.9 shows the schematic of chirped reflective FBG based TDC. The ways to achieve tunability include bending [17], stretching [18], heating (thermal strain) [19], and rotating (mechanical strain) [21] the chirped FBG. The achieved tunable ranges and device bandwidth are summarized in Table 3.3.

Several types of dispersion compensation devices can be integrated on an optical chip. Such integration has long term promise for low cost and high performance. The techniques include integrating array waveguide gratings (in other words wavelength grating router) [24-26] and integrating Mach-Zehnder interferometers with thermal phase tuning [27-29]. The waveguide layout and the concept of the TDC are shown in Fig.3.10. Light enters a planar lightwave circuit (PLC) containing an extremely high-resolution wavelength grating router (WGR) through the single waveguide that is attached to an optical circulator, which is used to separate the input and output signal. The light passes through a first free-space region in the PLC, is coupled into the WGR, and enters a second free-space region. At this second free-space region, the PLC is cut and the light is then spectrally spread out across a variable-curvature reflecting membrane. There is a plano-cylindrical glass lens attached to the PLC that collimates the light in the plane of the PLC. To achieve linear chromatic dispersion, variable curvature reflecting mirror has

been used to apply a phase distribution that varies quadratically with wavelength. The WGR approach also uses pulse shaping concept which was explained in detail in chapter 2 and first demonstrated in [34].

Table.3.2 summarizes the characteristics of various technologies in optical TDC [1].

### 3.3.2 Figure Of Merit

Given that the purpose of dispersion compensation devices is to provide negative dispersion, a figure of merit (FOM) is being used to compare the relative performance among the different solutions. The FOM is defined as [63]

$$FOM = \Delta D \times (B)^2 \quad (3.18)$$

where  $\Delta D$  is the dispersion adjustment range of the device and  $B$  is the bandwidth of the device. The larger FOM indicates better tunability with wider available bandwidth. The actual amount obtained by different technologies in terms of dispersion adjustment range (tuning range), device bandwidth, and normalized FOM are summarized in Table 3.3.

## 3.4 Optical Tunable Dispersion Compensation With A VIPA based TDC

### 3.4.1 VIPA Based Optical TDC

In this section, VIPA based pulse shaper which provides both tunable dispersion compensation and DWDM capability will be explained in detail. The VIPA based optical TDC is identical to the VIPA Fourier transform pulse shaper used in the optical pulse burst manipulation explained in Chapter 2. The main difference is that for the optical pulse burst manipulations, the periodic spectral phase function is applied to a broadband

optical spectrum (much broader than VIPA FSR), where as for the tunable dispersion compensations, only single period spectral phase is applied to the input optical spectrum (narrower than VIPA FSR) and the periodic spectral phase function is used to extend applications to the DWDM.

The schematic of the VIPA based optical TDC is shown in Fig.3.11 [35, 64]. It is similar to the setup in [6] but the curved mirror is replaced with a SLM to provide programmability without any moving parts. The VIPA spatially disperses the spectral components of each wavelength channels. The spatially dispersed spectral components are focused at the Fourier plane, where the SLM is located, by using a focal length lens. The SLM at the Fourier plane applies the phases of individual spectral components within each wavelength channels according to the desired phase function which is pre-calculated to compensate the dispersion within the wavelength channels by a laboratory computer through a controller. For the reflected path, the lens and the VIPA recombine the dispersion compensated spectral components into a single output beam which is coupled back into the fiber. For the experiments of various fiber spans (in Fig.3.18 to Fig.3.22 and Fig.3.25 to Fig.3.26), a polarizer was inserted into the TDC setup to allow programmable independent phase and amplitude control. For the experiments of DWDM capabilities and polarization independence of TDC (in Fig.3.23 and Fig.3.24), the polarizer was removed and a flipper mirror and a polarimeter were inserted between the collimator and the VIPA to tap and monitor the polarization of the incoming light. The polarization controller at the input was used to change the polarization state of incoming light and later used to prove the polarization independence of the TDC.

The optimum focal length for the semicylindrical lens,  $f_1$ , is chosen to minimize beam clipping loss at the edge of the VIPA incident window as [7, 65],

$$t \tan(\theta_i / n_r) \geq w_0 \sqrt{1 + \frac{t^2 \lambda_0^2}{n_r^2 \pi^2 w_0^4}}, \quad w_0 = \frac{f_1 \lambda_0}{\pi W} \quad (3.19)$$

where the incident angle  $\theta_i = 2.5^\circ$ , refractive index of glass  $n_r = 2.0$ , VIPA thickness  $t = 1.5$ -mm, operating wavelength  $\lambda_0 = 1550$ -nm, and beam radius at the fiber collimator  $W = 2.0$ -mm. We used  $f_1 = 10.0$ -mm which is close to the optimal range.

The SLM is a standard liquid crystal modulator array composed of 128 controllable pixels with dimensions of 2-mm by 100- $\mu$ m per pixels which yields 12.8-mm in total. The optimum focal length  $f_2$  for the focusing lens was found by [7, 65],

$$\Delta\lambda(x) = -\lambda_0 \left[ \frac{\tan \theta_{in} \cos \theta_i}{n_r \cos \theta_{in}} \frac{x}{f_2} + \frac{1}{2} \frac{1}{n_r^2} \frac{x^2}{f_2^2} \right] \quad (3.20)$$

where  $\theta_{in} = \theta_i / n_r = 1.25^\circ$  and  $\Delta\lambda(x) \sim 9.0$ -mm is the spatial spread at the Fourier plane for wavelength of VIPA FSR ( $\sim 0.4$ -nm, 50-GHz). We used the optimum value of  $f_2 = 300$ -mm (the spatial spread,  $\Delta\lambda(x)$ , can be increased to 12.0-mm, which will cover the total SLM dimension by replacing  $f_2$  to 400-mm). In the actual experimental setup, we achieved spatial spread of 7.0-mm which yields 70 controllable pixels in the SLM which yields the spectral spread of  $\sim 0.0055$ -nm/pixel ( $\sim 0.68$ -GHz/pixel) for each wavelength channels. The pulse shaper has the resolution of  $\sim 1$ -pixel/chip (meaning the beam diameter at the SLM is approximately the size of a pixel). The pulse shaper was configured in a reflective geometry which has the advantage of saving the components (and space) and provides simpler alignment. The periodicity of the TDC was  $\sim 49.98$ -GHz, which was determined by the VIPA FSR, with passbands approximately centered on the ITU grid. The insertion loss for the TDC including circulator and polarization controller is around 15-dB. As a DCF module today is capable of compensating 80kms of SMF transmission fiber with an insertion loss of about 6-dB, the loss of the TDC is comparable to the estimated 18-dB loss that would be incurred for compensation of a 240km SMF span with the DCF. The complete description of insertion loss mechanisms in VIPA based pulse shaper can be found in Appendix A.

In section 3.1, we have explained the dispersion induced degradation is due to the phase factor  $\exp[i\beta_{2z}(\Delta\omega)^2/2]$  in Eq.(3.13) obtained during the propagation along the

fiber and all dispersion compensation schemes attempt to cancel the phase factor  $\exp[i\beta_2 z(\Delta\omega)^2/2]$ . This cancellation can be achieved by adding appropriate quadratic and cubic phase curve to the laser spectrum. Since the spectral components of the each wavelength channels are spatially dispersed at the Fourier plane of pulse shaper by the VIPA, quadratic and cubic phase curve can be added to the laser spectrum simply through applying the required voltage across the SLM by a laboratory computer through a controller. The phase provided by the  $n$ -th SLM pixel can be written as

$$\Phi(n) = \frac{\phi_{quad}}{2!} \left(n - \frac{N_{BW}}{2}\right)^2 \delta\omega^2 + \frac{\phi_{cubic}}{3!} \left(n - \frac{N_{BW}}{2}\right)^3 \delta\omega^3 \quad (3.21)$$

where  $N_{BW}$  is the total number of pixels,  $\phi_{quad}$  (in squared picoseconds) and  $\phi_{cubic}$  (in cubic picoseconds) represent the second and third order dispersion, respectively.  $\delta\omega$  (in rad/s) is the wavelength (or frequency) increment between the adjacent pixels. Note that the pixels are numbered in such way that longer wavelength components impinge on higher number pixels.  $\phi_{quad}$  and  $\phi_{cubic}$  are also the amplitudes of the quadratic and cubic phases involved in pulse shaping operation. We should also note, when  $|\beta_2|$  exceeds  $1\text{ps}^2/\text{km}$ ,  $\beta_3$  term is neglected in practice [44-45], so we set  $\phi_{cubic} = 0$ .

Fig.3.12 shows the conceptual diagram of the quadratic phase applied to incident wave spectrum by SLM in VIPA based optical TDC. By using the amplitude modulation capability of the SLM, we have limited the passband within the FSR to 28-GHz (41 pixels, shown as  $\Delta\Omega_1$  in Fig.3.12), which is large enough for 50-GHz spaced WDM systems, and placed the wavelength channel at the middle of the passband (passband characteristics of TDC is shown in Fig.3.25). This is done to ensure a linear mapping between optical frequency and spatial position (or SLM pixel number).

Within the programmed passband, the quadratic phases provided by pixel  $n$  of the SLM can be formulated as [64]

$$\Phi(n) = \frac{\phi_{quad}}{2}(n-21)^2(2\pi \cdot \Delta f)^2 \quad \text{and} \quad (DL)_{eff} = -\frac{2\pi c \cdot \phi_{quad}}{\lambda^2} \quad (3.22)$$

where  $n$  is the pixel number from 1 to 41,  $\phi_{quad}$  (in squared picoseconds) is the second-order phase dispersion,  $\Delta f$  is the frequency increment between adjacent pixels (which is  $\sim 0.0055$ nm or  $\sim 0.68$ -GHz in our case), and  $(DL)_{eff}$  is the effective dispersion provided by the VIPA based optical TDC setup. The phase variation is discretely sampled over the 41 pixels. The amount of chromatic dispersion applied by the TDC is determined by the quadratic phase variations within the pixels by changing  $\phi_{quad}$  in Eq.(3.22). The chromatic dispersion compensation of 240km standard SMF transmission was achieved by applying quadratic phase with maximum excursion of  $-6.3\pi$  for pixels 1 and 41 in Eq.(3.22) ( $\Delta\Phi_{max} = -6.3\pi$  in Fig.3.12). Likewise, 120km and 60km SMF were compensated by applying the quadratic phase with maximum excursion of  $-3.3\pi$  and  $-1.8\pi$ , respectively. One of the significant advantages of our set-up is that the SLM in TDC has close to 800 different phase levels within the 0 to  $2\pi$  range which can be programmed by using a laboratory PC and allow us to apply accurate values of chromatic dispersion needed in the system.

### 3.4.2 Evaluating System Performances

#### Bit Error Ratio (BER) Measurements

In any digital communications transmission system, the fundamental measure of the quality of the system is found in the probability that transmitted bits will be correctly received as logic ones or zeros. The parameter that describes this measure of quality is the BER. Simply stated, BER is the average probability of incorrect bit identification of a bit by decision circuit of the receiver for a specified time interval or quantity of bits. A commonly used criterion for digital optical receivers requires BER of less than  $1 \times 10^{-9}$  [66].

Fig.3.13 shows the schematic diagram of BER test set-up. The test equipment required to perform a BER test include a pattern generator and an error detector. The pattern generator will produce a known data sequence to the system or device under test. Test patterns can be designed such that they intentionally stress some aspect of the system. For example, a data sequence may be generated that is difficult for a clock recovery system to synchronize. Also, data patterns that attempt to mimic real traffic can be produced. A common pattern used is the pseudo-random binary sequence (PRBS). A PRBS has the characteristic of producing all possible combinations of ones and zeroes for a given pattern length. For example, a  $2^7-1$  PRBS pattern will produce all possible combinations of 7 bit binary numbers from 0000001 to 1111111 (The 0000000 sequence is not produced due to limitations of the logic hardware used to generate the pattern). Pattern generators also typically produce longer PRBS patterns, some as long as  $2^{31}-1$ , that will generate all combinations of 31 bit binary numbers except the case of all zeros.

The error detector is used to determine if the data received match the transmitted pattern. The error detector will receive the output of the receiver of the system. The system receiver under test will have attempted to determine the logic level of each bit transmitted by the system under test. The output of the receiver decision circuit is then routed to the error detector. In its most basic building blocks, the error detector consists of an internal pattern generator and an exclusive or logic gate. The error detectors internal pattern generator will produce a reference pattern identical to the pattern fed from the pattern generator feeding the test drive. The reference pattern is synchronized to the test device output and then compared bit for bit with the exclusive or gate. Determining the BER is then a simple matter of counting the total bits received and the number of bits that were incorrectly received.

In typical digital communication systems, the power from the transmitter is large enough that if it were to arrive unattenuated at the system receiver, there would be error-free communication. System performance in terms of BER is then often characterized in terms of the amount of attenuation between the transmitter and the receiver. Similarly, the BER can be characterized in terms of power level at the receiver. Fig.3.14 shows an

example of a typical BER characterization of a high-speed system. As the received power decreased, the signal-to-noise ratio is reduced and the probability of a bit being received in error increases.

### Eye diagram

The eye diagram shown in Fig.3.15 is an overlay of many transmitted waveforms [66]. By using a clock signal as the trigger input to the digital sampling oscilloscope, the transmitted waveform can be sampled over virtually the entire data pattern generated by the transmitter. Thus, all the various bit sequences that might be encountered can be sampled to build-up an eye diagram.

For eye diagram analysis the sample rate of a digital sampling oscilloscope is typically orders of magnitude slower than the data rate of the signal being characterized, i.e. when a point is sampled, the next adjacent point in time sampled will occur thousands of bits later in the transmitted waveform. It should be noted that the intent of the eye diagram is not to display individual transmitted bits. Instead, it is constructed from a multitude of waveform samples. It then allows a good visual representation of the overall quality of the waveform.

The eye diagram includes a significant amount of information about the transmitted signal. The relative separation between the two logic levels is easily seen in the vertical “opening” of the eye. Obviously, the more open the eye is, the easier it will be for the receiver to determine the signal logic level. Rise and fall times can be measured on an eye diagram to determine transmitter speed. Modern digital sampling oscilloscopes have the ability to automatically construct histograms to statistically analyze the eye diagram. The jitter describes the relative instability of the bit period or data rate of a signal. This can be quantified by measuring the variance in the relative time in which the rising and falling edges occur. By constructing a histogram at the eye diagram crossing point, jitter is determined.

### 3.4.3 Optical Transmission Results Using VIPA Based Optical TDC

Fig.3.16 shows the experimental set-up for TDC. A Tektronix OTS 9010 Optical Test System which consists of pulse pattern generator (PPG) and bit error rate tester (BERT) modules has been used to measure transmission performances (For the return to zero (RZ) lightwave transmission experiments in Chapter 4, Agilent Technologies N490113 Serial BERT has been used). The PPG provides both the 10Gbps data signal (in non-return to zero (NRZ) with  $2^{31}-1$  length PRBS format) and the clock signal for the synchronization between the PPG and the BERT as shown in Fig.3.13. The electric-to-optic (E/O) converter module is composed by a CW tunable laser, polarization controller (PC), and a  $LiNbO_3$  external modulator (shown in Fig.3.17(a)). The E/O converter module was intentionally positively chirped to yield similar characteristics as a directly modulated laser (shown in Fig.3.17(b)) explained in Section 3.1.3. A RF driver is used to amplify the 10Gbps PPG data signal and a bias-T is used to apply the amplified 10Gbps data signal and a fixed dc bias to the  $LiNbO_3$  external modulator input as shown in Fig.3.17(a). The output optical power of the CW LD is 5.0dBm. The  $LiNbO_3$  external modulator had  $\sim 7$ dB insertion loss and the two PCs before and after the  $LiNbO_3$  external modulator had  $\sim 3$ dB insertion loss including the connector losses. So the output optical power of E/O converter module is  $-5.0$ dBm. The polarization controller between the E/O converter module and the TDC is needed to change the polarization state of incoming light and later used to prove the polarization independence of the TDC. The TDC is a VIPA based optical TDC explained in detail in Section 3.4.1. The TDC and polarization controller combination had  $\sim 15$ dB insertion loss including the optical circulator, yielding  $-19.5$ dBm optical power at the output. The pre-compensated TDC output is then connected to the erbium doped fiber amplifier (EDFA) to boost the optical power. The EDFA is operated at 150mA bias current yielding  $\sim 30$ dB optical gain in the 1550nm window, resulting in 10.5dBm optical power.

The transmission link consist of two fiber spans up to 240km SMF. An additional optical in-line amplifier (EDFA) was used to compensate the optical power loss within the

system link. Various length of fiber spools within the system link were used to generate different dispersions (20km ~ 240km SMF with  $D = +17\text{ps/nm-km}$  and 4.8km ~ 9.5km DCF with  $D = -90\text{ps/nm-km}$ ) to prove tunability of TDC in both positive and negative directions, and variable optical attenuators (VOA) were placed after the fiber spools to fix the insertion loss within the fiber links to 26dB in order to maintain constant optical power of  $-16.0\text{dBm}$  at the optical in-line amplifier and pre-amplifier input for different fiber length.

The received optical signal at the transmission link output is amplified by an optical pre-amplifier (EDFA). The tunable optical bandpass filter (BPF) from JDS Fitel (TB4500), having the 3dB bandwidth of  $\sim 1.3\text{nm}$  and the insertion loss of  $\sim 4\text{dB}$  in the 1530nm to 1560 nm window, is used after the EDFA to filter out the optical amplifier noises (and select a single wavelength channel within the DWDM channels in the future experiments). Another VOA is used to vary the received optical power at the O/E converter module. By changing the received optical power with the VOA, we could construct the BER curve similar to Fig.3.14 which quantifies the system performance. The O/E converter module output is fed to the BERT to measure the BER. The O/E output is also connected to the digital sampling oscilloscope to measure the eye diagram. The 2x2 coupler is used to measure the optical power and the BER simultaneously as shown in Fig.3.16.

Fig.3.18 shows TDC measurements using a positively chirped 10-Gbps NRZ source in terms of BER characteristics and power penalties. Fig.3.18(a) is the BER curves for SMF transmission without TDC upto 40km (which is the maximum distance that can be transmitted without TDC for our positively chirped 10-Gbps NRZ transmission system). The curve with cross(+) markers is the back-to-back case (B2B), where everything is removed except a VOA and a 2x2 coupler between the E/O module and the O/E converter module (no SMF propagation) in Fig.3.16. This curve will be used as the reference curve for the entire experiments. The curve with circle( $\circ$ ) markers is the case for no SMF propagation but every optical components between E/O module and O/E converter module in Fig.3.16 are included (B2B VIPA). In this case the SLM phase in

TDC set to a constant (No compensation). The  $\sim 1.5$ dB power penalty in B2B VIPA case from B2B case is partly due to additional components in the setup and partly due to the residual dispersion in VIPA based TDC setup (path length difference between shorter wavelength and longer wavelength within the VIPA based TDC setup [6]). It can be further reduced (or eliminated) by carefully aligning the setup. But we performed experiments without fully eliminating such residual dispersion, because it can be removed by applying some additional negative chromatic dispersion provided by the VIPA based TDC itself which is much simpler. The power penalties due to 20km and 40km SMF transmissions are  $\sim 5$ dB and  $\sim 8$ dB, respectively. Fig.3.18(b) shows the BER curves for the chromatic dispersion compensation results for various fiber lengths upto 240km (4080 ps/nm) using TDC. The chromatic dispersion compensation of 240km standard SMF transmission was achieved by changing quadratic phase with maximum excursion of  $-6.3\pi$  for pixels 1 and 41 ( $\Delta\Phi_{max} = -6.3\pi$  in Fig.3.12) by adjusting  $\phi_{quad}$  in Eq.(3.22). Likewise, 120km and 60km SMF were compensated by applying the quadratic phase with maximum excursion of  $-3.3\pi$  and  $-1.8\pi$ , respectively. The results in Fig.3.18(b) show error-free transmission with the power penalty kept below 1-dB in all cases. For comparison figures also show the BER curves for back-to-back operation without the TDC set-up (B2B), with the TDC set-up but with the SLM phase set to a constant (B2B VIPA), and for 20km and 40km of SMF transmission without dispersion compensation (without TDC set-up).

Fig.3.19 shows the eye diagrams of various SMF transmission lengths without TDC compensation using a 10-GHz photodiode (which was used to measure the BER in Fig.3.18). The eye diagrams start to degrade when SMF transmission length exceeds 20km (Fig.3.19(b)), and they are completely closed when SMF transmission length exceeds 60km (Fig.3.19(d)).

Fig.3.20 shows the eye diagrams of various SMF transmission lengths with optimum TDC compensation using a 10-GHz photodiode. The clear eye openings in these results show the accumulated dispersions are effectively removed by the TDC, which is consistent with the BER results in Fig.3.18.

Fig.3.21 shows BER curves for a positively chirped 10-Gbps NRZ source transmitted along the various DCF spans with and without TDC compensation. The BER curve with cross(+) markers is the back-to-back case (B2B) and the BER curve with up-triangle( $\triangle$ ) marker is the 4.8km DCF transmission without TDC. The results for the chromatic dispersion compensation for 4.8km DCF (+425 ps/nm) and 9.5km DCF (+850 ps/nm) using TDC are shown in BER curve with circle( $\circ$ ) markers and down-triangle( $\nabla$ ) markers, respectively. The chromatic dispersion compensation of 9.5km DCF transmission was achieved by changing quadratic phase with maximum excursion of  $+1.0\pi$  for pixels 1 and 41 ( $\Delta\Phi_{max} = +1.0\pi$  in Fig.3.12) by adjusting  $\phi_{quad}$  in Eq.(3.21). Likewise, 4.8km was compensated by applying the quadratic phase with maximum excursion of  $+0.4\pi$ . The results show error-free transmission with the power penalty kept below 1-dB in all cases. The results show the positive dispersion compensation capabilities of the VIPA based TDC. For comparison figures also show the BER curves for 20km (square( $\square$ ) markers) and 40km (diamond( $\diamond$ ) markers) of SMF transmission without dispersion compensation (without TDC set-up).

Fig.3.22 shows the eye diagrams of various DCF transmission lengths using a 10-GHz photodiode. Fig.3.22(a) and (c) show the eye diagrams of 4.8km DCF transmission for before and after TDC compensation. Fig.3.22(b) and (d) show the eye diagrams of 9.5km DCF transmission for before and after TDC compensation. The clear eye openings after the compensation results (Fig.3.22(c) and (d)) show the accumulated dispersions are effectively removed by the TDC, which is consistent with the BER results in Fig.3.21.

To prove DWDM capability of the TDC, SMF transmission lengths was fixed to 240km in Fig.3.16 (120km SMF in each fiber span) and four adjacent 50-GHz spaced ITU wavelength channels around 1550nm (1550.12, 1550.52, 1550.92, 1551.32nm) have been applied by tuning the wavelength of E/O module. The chromatic dispersion compensation for 240km SMF was achieved by changing quadratic phase with maximum excursion of  $-6.3\pi$  for pixels 1 and 41 ( $\Delta\Phi_{max} = -6.3\pi$  in Fig.3.12) by adjusting  $\phi_{quad}$  in Eq.(3.22) and no additional adjustments were needed for different wavelengths. Similar error-free transmission has been achieved for all four wavelength cases as shown in

Fig.3.23 which shows potential WDM capability of the TDC if the VIPA FSR is matched to the WDM channel spacing. For comparison figures also show the BER curves for back-to-back operation without the TDC set-up (B2B), with the TDC set-up but with the SLM phase set to a constant (B2B VIPA), and for 20km and 40km of SMF transmission without dispersion compensation (without TDC set-up).

Fig.3.24 shows the polarization independence of TDC. The BER was measured by using the setup with 240km SMF transmission compensated by TDC (-4080 ps/nm dispersion applied) with different polarization states. Five different polarization states (namely, arbitrary elliptical, linear horizontal, linear vertical, linear 45-degrees, left hand circular) were tested. The different polarization states were tuned by using a polarization controller at the TDC input and monitored by a polarimeter as shown in Fig.3.11. No adjustments were made at the TDC for the different polarization states. The results in Fig.3.24 show that the dependence of the power penalty due to the polarization is negligible. The BER for the back-to-back (B2B), 20km and 40km of SMF transmission without dispersion compensation is also shown in Fig.3.24 for comparison.

Fig.3.25 shows the transmission spectra for the TDC with different dispersion settings ranging from -4080 to +4080 ps/nm. No significant changes in the transmission spectrum were observed. The deviation of the spectrum was less than 2-dB over the full range of the TDC tested. This indicates the capability of programmable wavelength-dependent phase response with a relatively flat amplitude response that depends only weakly on wavelength and programmed dispersion. These are important features needed for tunable dispersion compensating modules.

Fig.3.26(a) show examples of the spectral phase response which is another characterization measurements of the TDC performed by one of my collaborator Shijun Xiao. It is measured by modulating a microwave tone onto a CW laser, which is passed through the TDC, detected, and analyzed by a vector network analyzer over a 20-GHz optical band for several dispersion settings from -2000 to +2000 ps/nm. Detailed experimental setup is shown in Fig.3.26(b) and also can be found in [67]. The results confirm that clear quadratic phase functions can easily be applied. In some cases

evidence of small phase steps can be observed at large phase shifts (e.g. 6 ~ 10-GHz region of +2000 ps/nm). These steps correspond to the individual pixels in the SLM and can, in principle, be smoothed by reducing the spectral resolution of the VIPA based TDC.

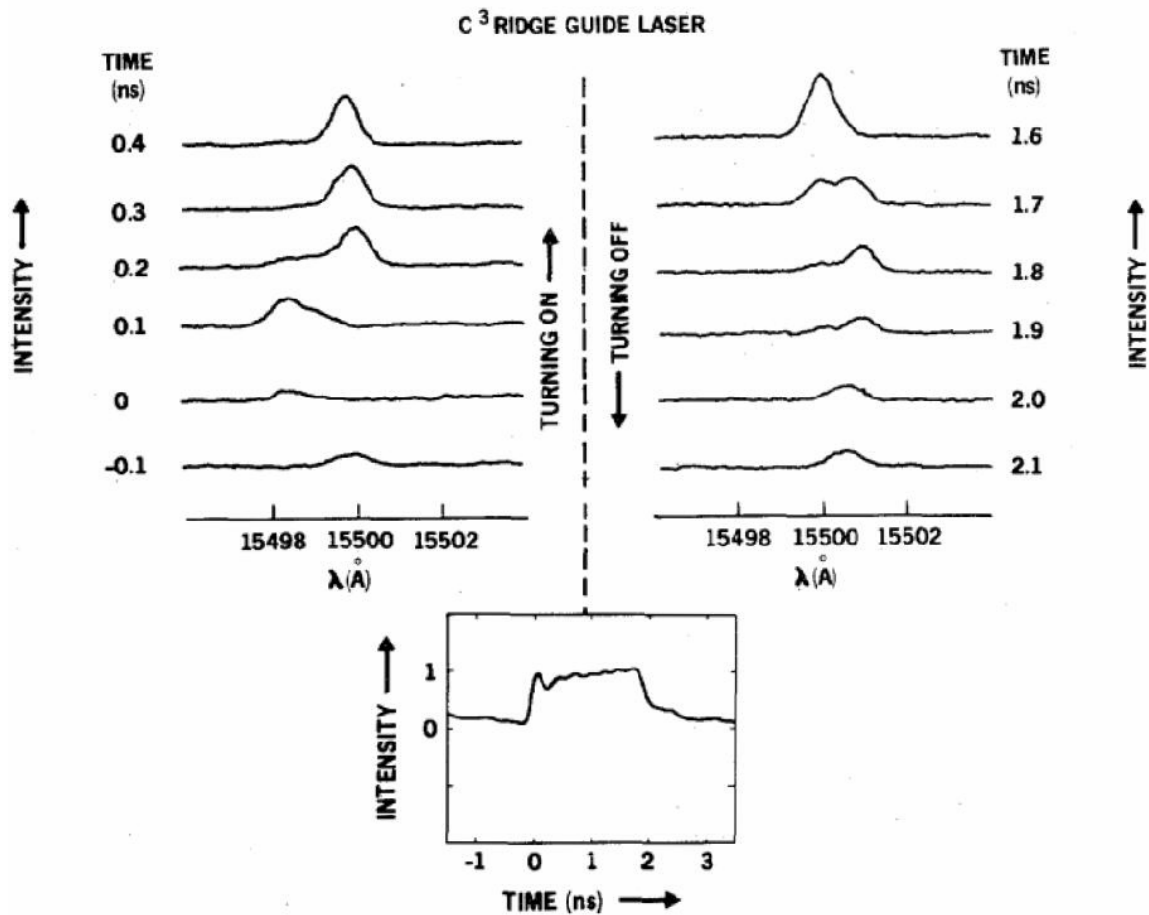


Fig. 3.1 Time resolved spectra speed 100ps apart are shown for the start-up and shut-down portion of a pulse from a positively chirped optical source (adapted from [50])

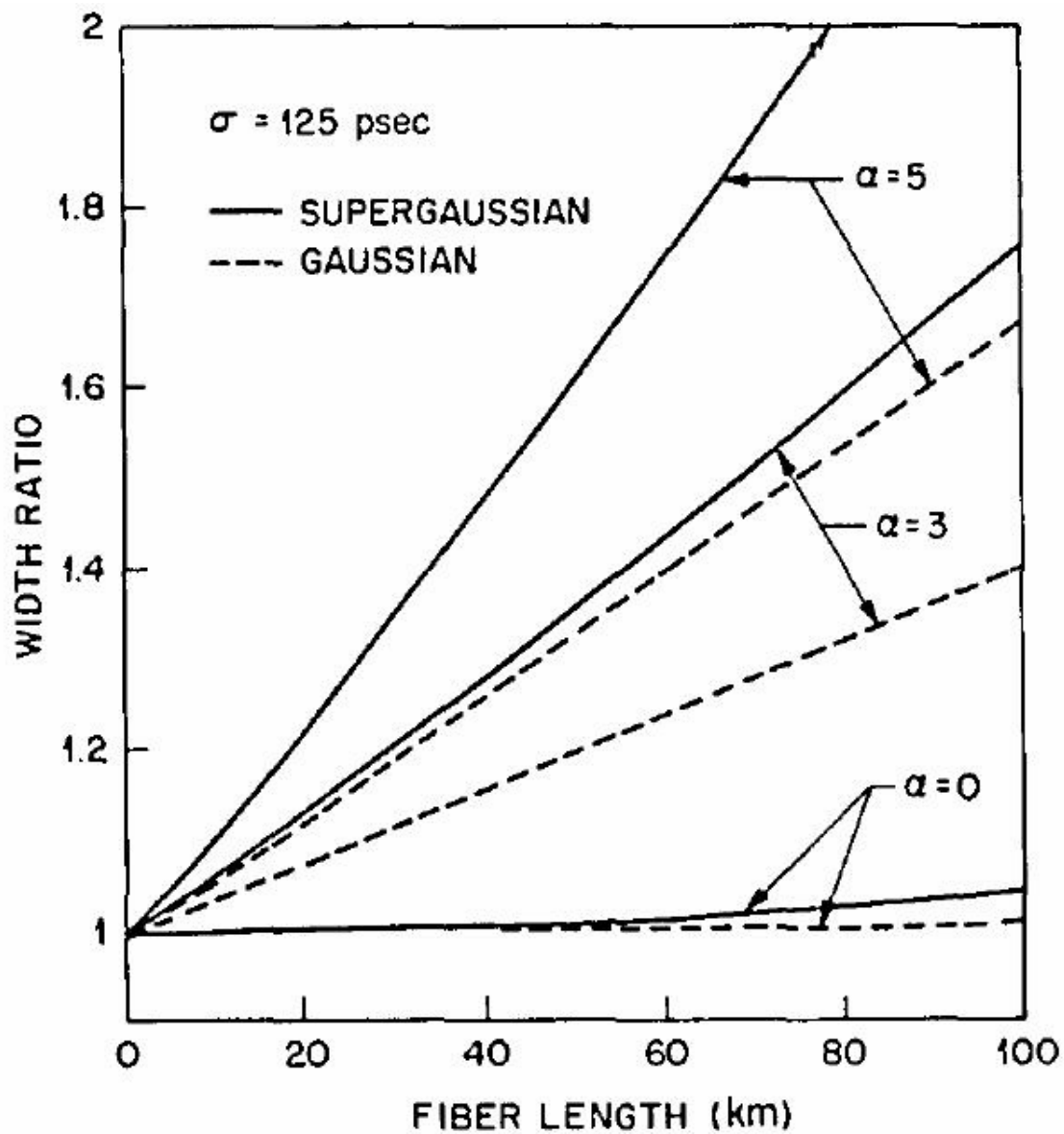


Fig.3.2 Broadening of a 125-psec half-width pulse with the fiber length for three values of the chirp parameters using  $D=16\text{ps/nm/km}$ . Solid and dashed curves correspond to super-Gaussian and Gaussian pulse shape (adapted from [46]).

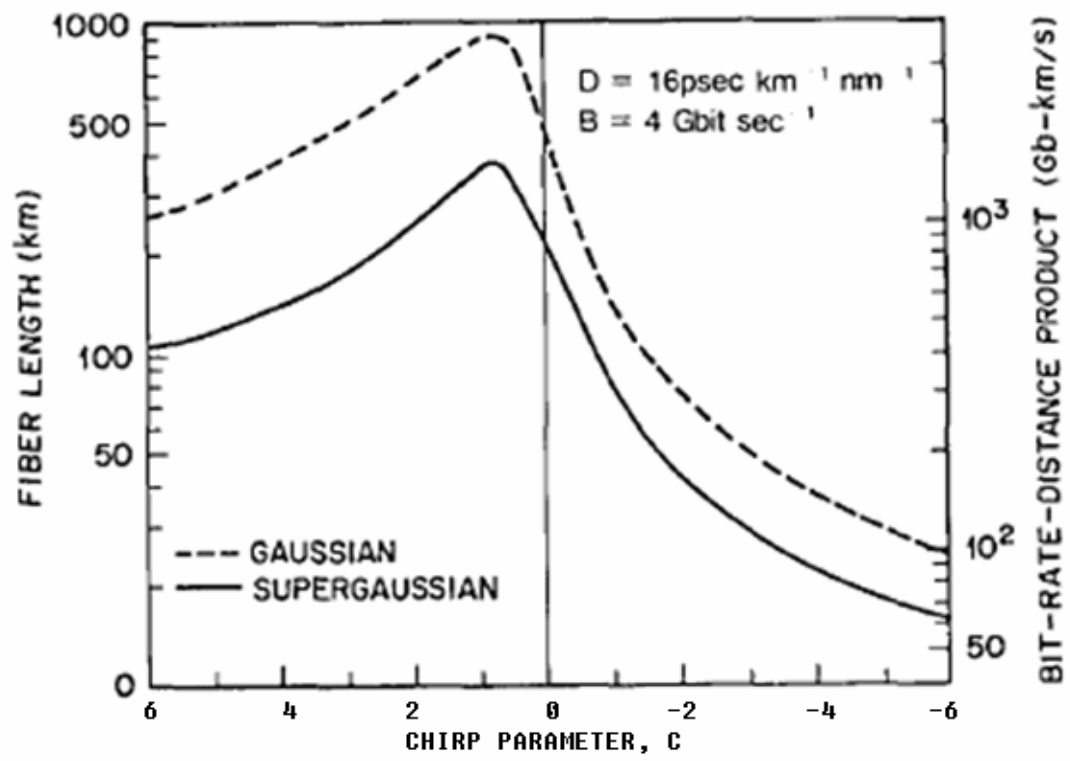
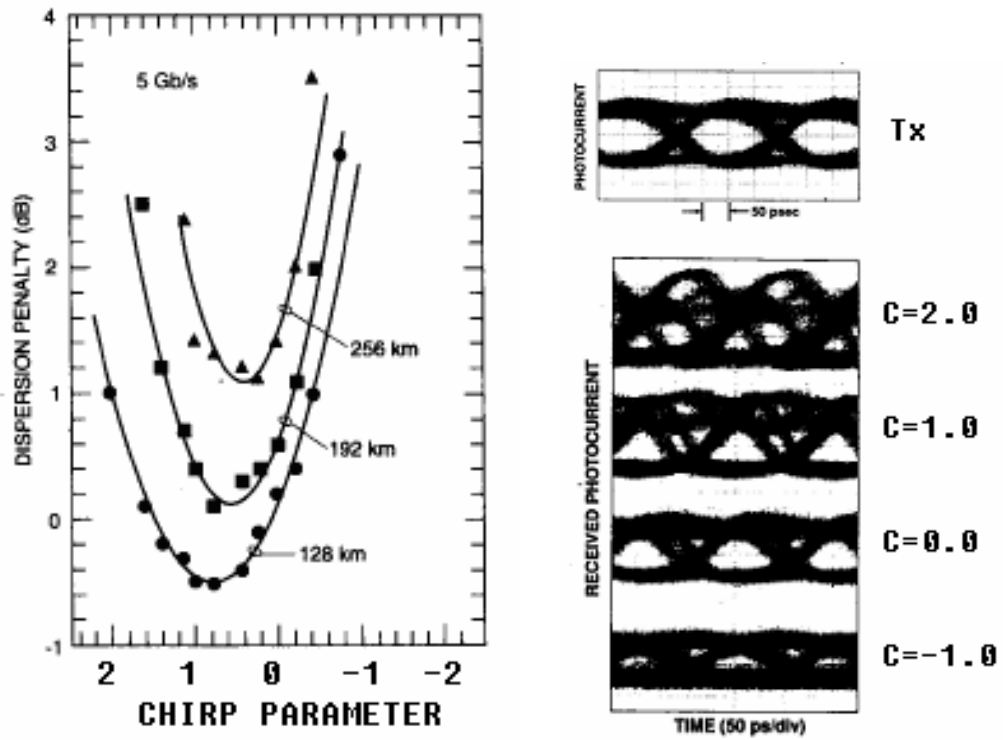


Fig.3.3 Variation of maximum fiber length with chirp parameter C. The BD product shown is assuming a bit rate of 4Gbps (adapted from [46]).



(a)

(b)

Fig.3.4 (a) Measured dispersion penalty versus modulator chirp parameter in 5Gbps transmission system using external  $LiNbO_3$  modulator with adjustable chirp, (b) eye-patterns at 256km for different chirp parameters (adapted from [53]).

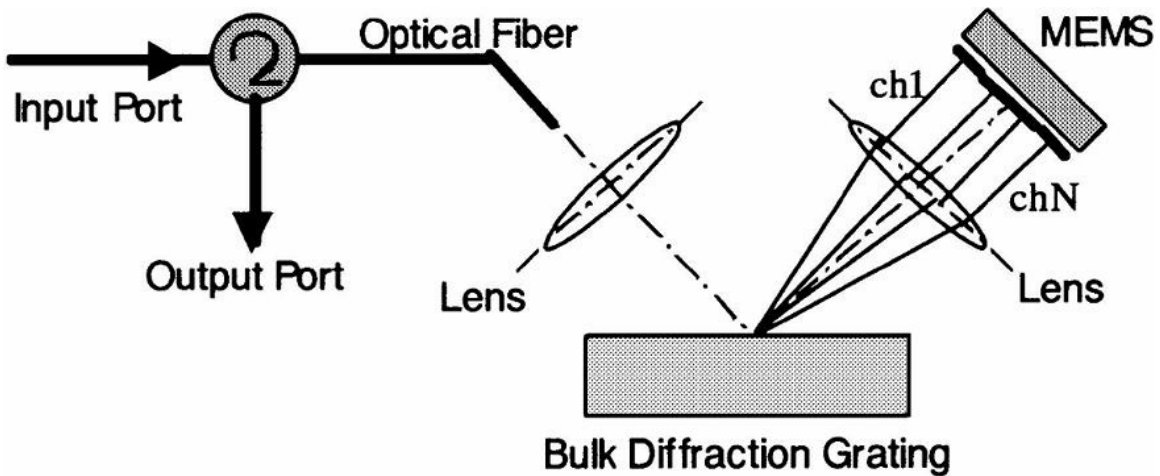


Fig.3.5 Schematics of MEMS based TDC (adapted from [8]).

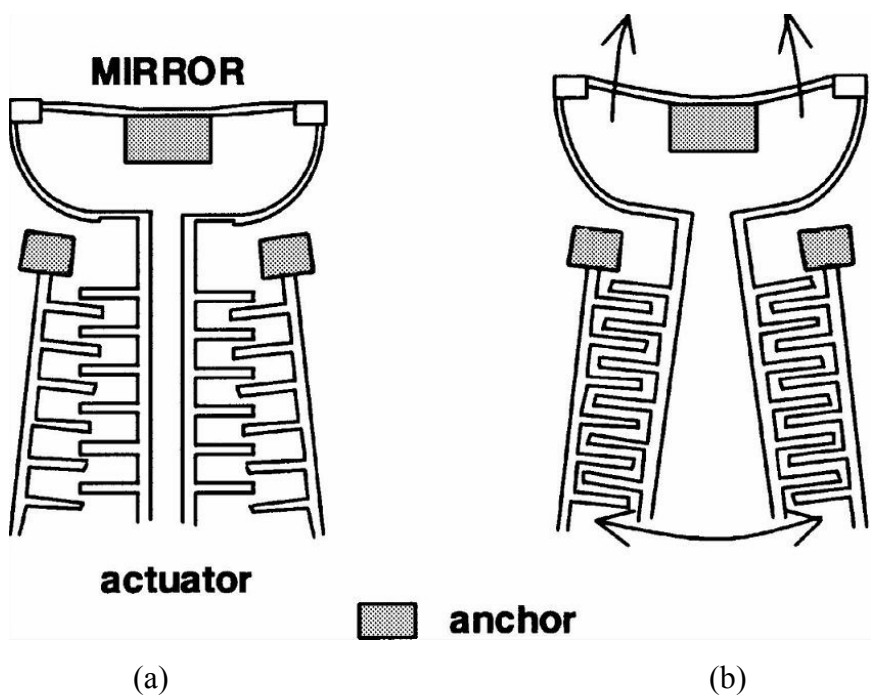


Fig.3.6 Schematic of the MEMS actuator and mirror: (a) No voltage applied. (0 [V]) (b) Voltage applied (100 [V]). (adapted from [8]).

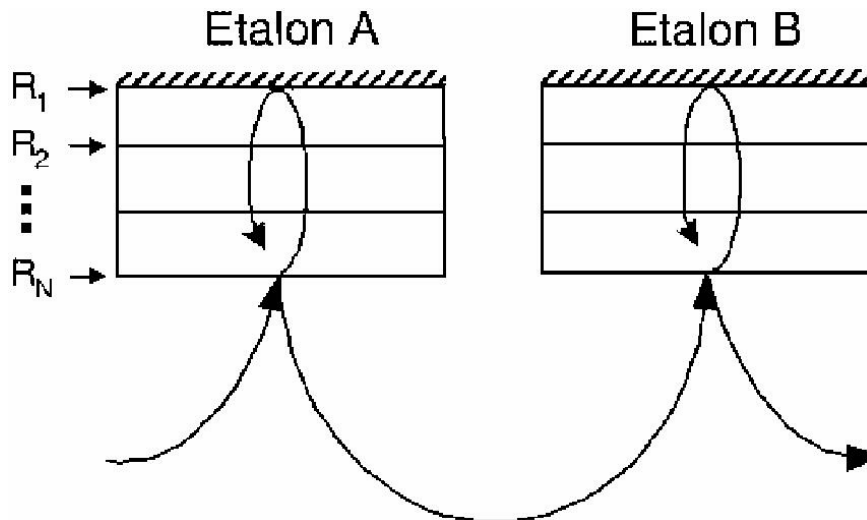


Fig.3.7 Schematic of multicavity etalon TDC. The etalons have a reflective interface between each cavity with only  $R_1$  being close to 100% reflective. (adapted from [10-11])

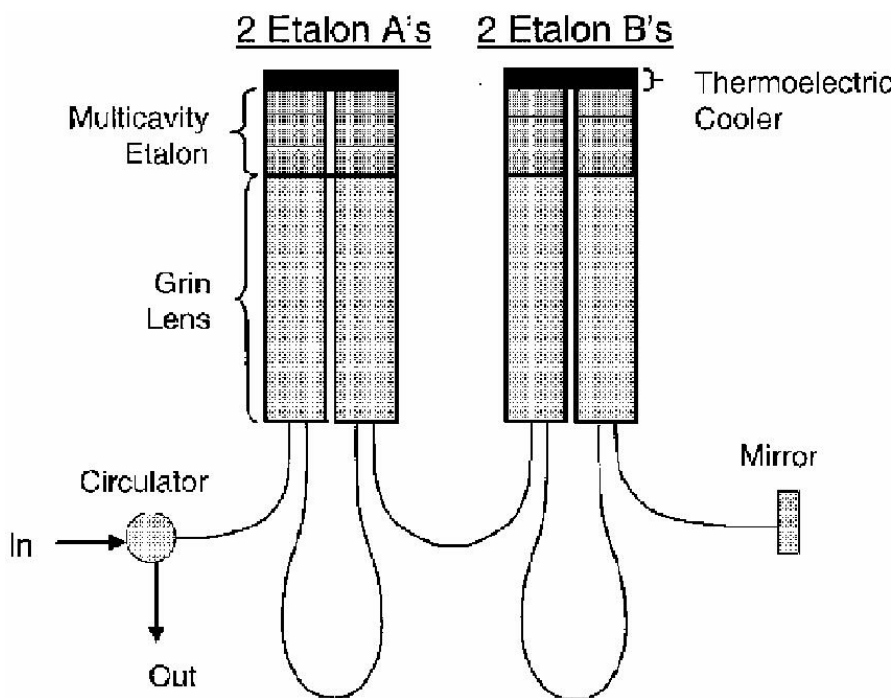


Fig.3.8 Optical coupling configuration for multicavity etalon based TDC. (adapted from [10-11])

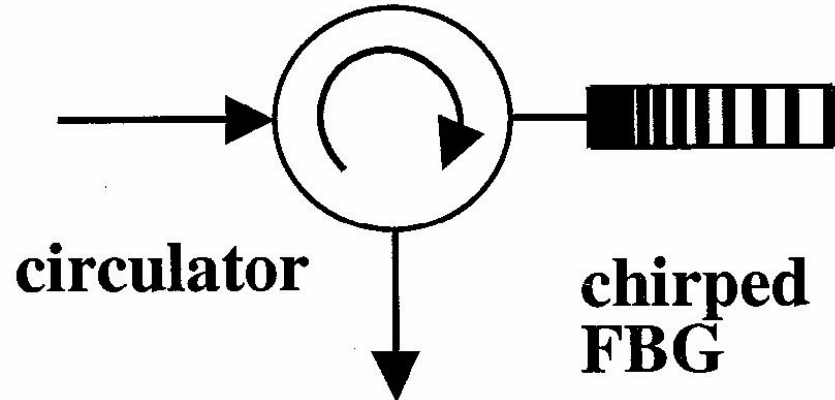


Fig.3.9 Schematic of chirped reflective FBG based TDC.

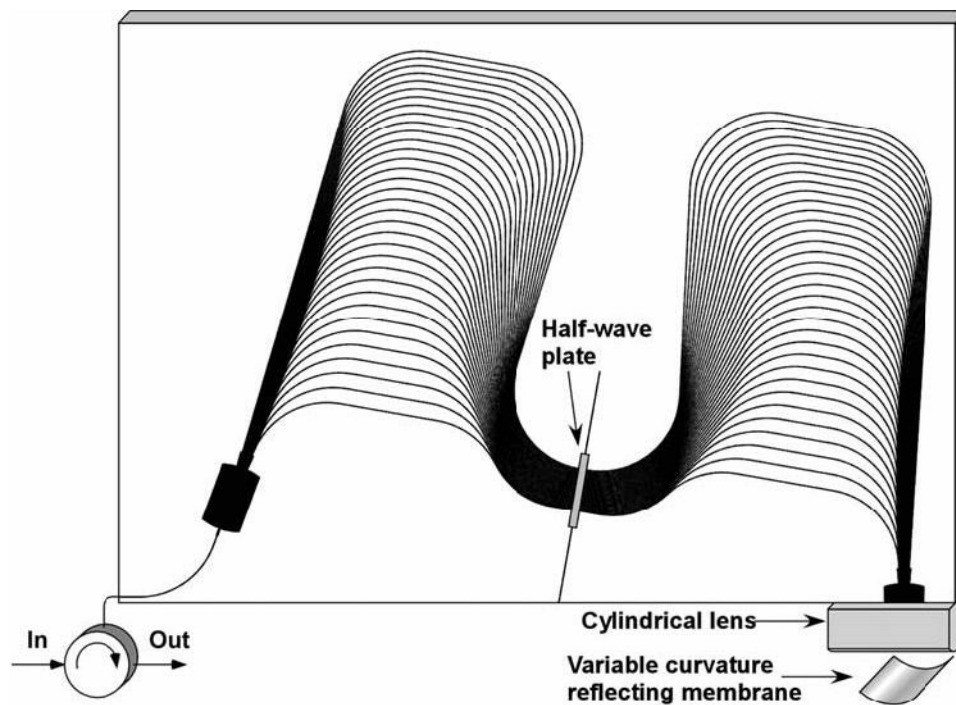


Fig.3.10 Schematic layout of the WGR based TDC using pulse shaper concept (adapted from [25]).

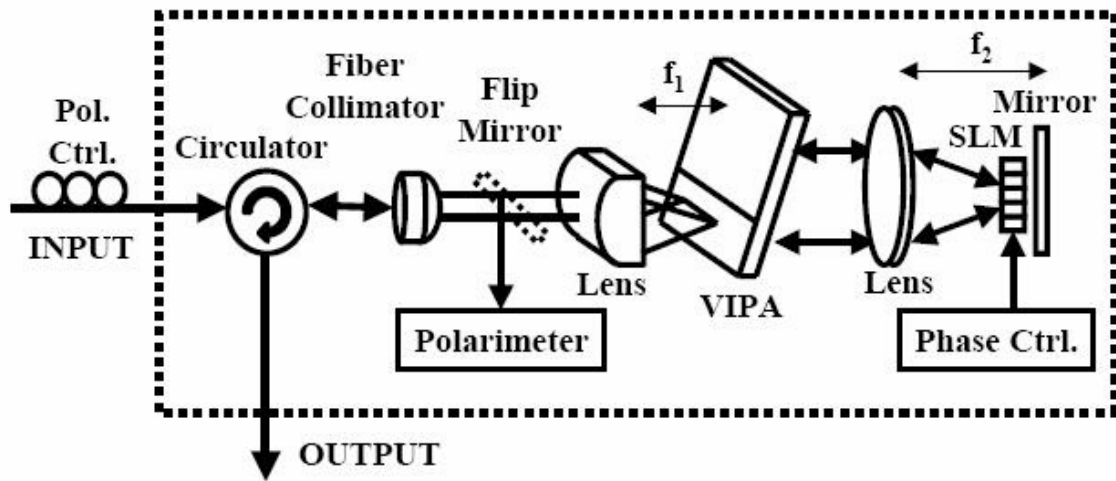


Fig.3.11 Schematic of VIPA based optical TDC

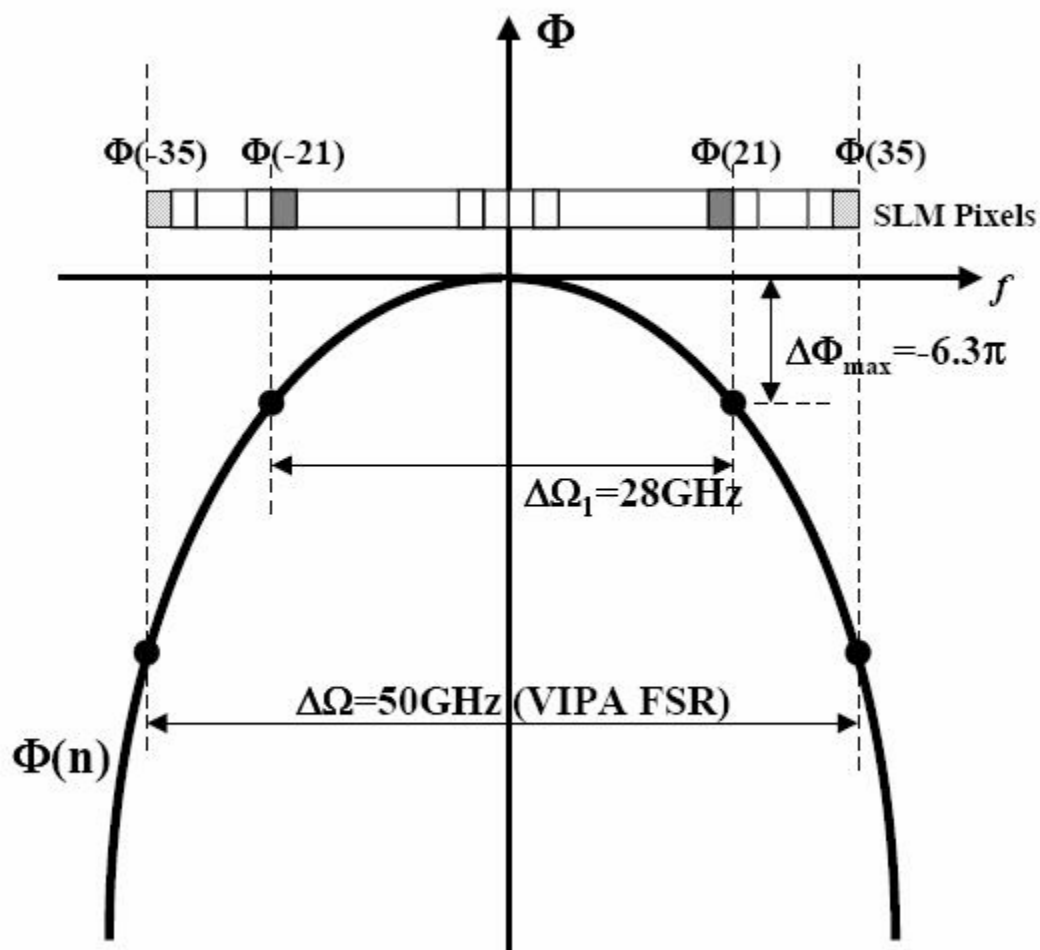


Fig.3.12 Conceptual diagram of quadratic phase applied to incident wave spectrum by SLM in a VIPA based optical TDC.

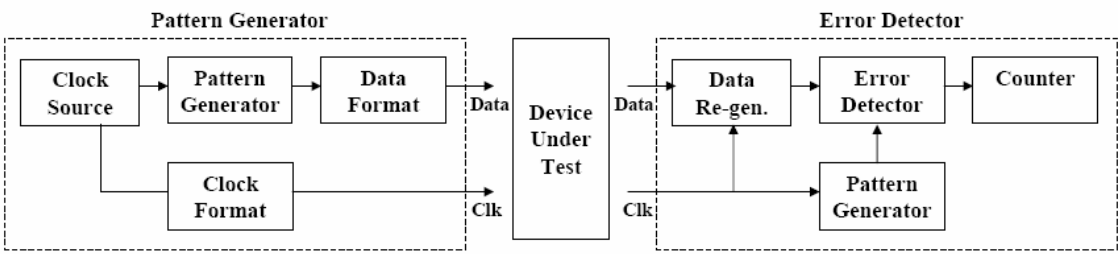


Fig.3.13 Schematic diagram of BER test set-up

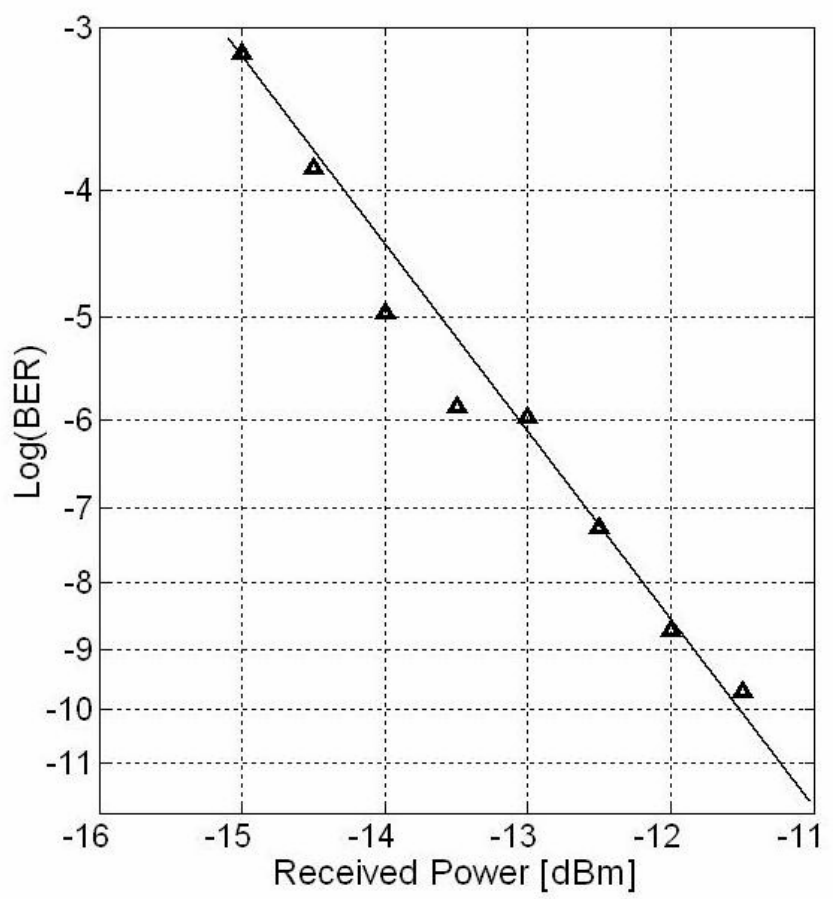
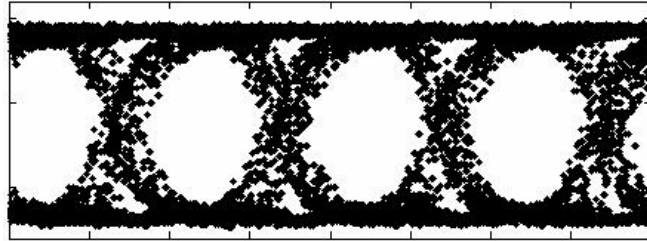
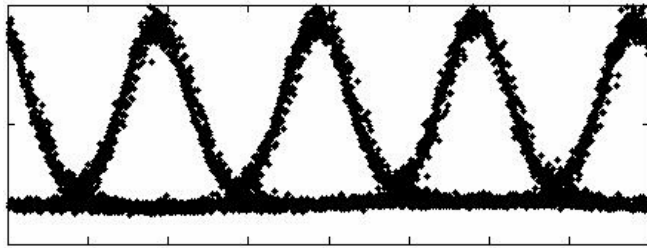


Fig.3.14 Example of typical BER curve (BER vs received power)



(a)



(b)

Fig.3.15 Example of typical eye diagrams : (a) For Non-Return-to-Zero (NRZ) signals. (b) For Return-to-Zero (RZ) signals.

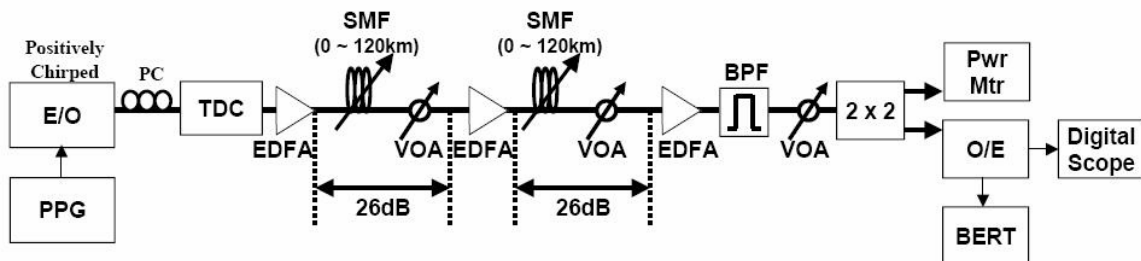


Fig.3.16 Experimental set-up for TDC

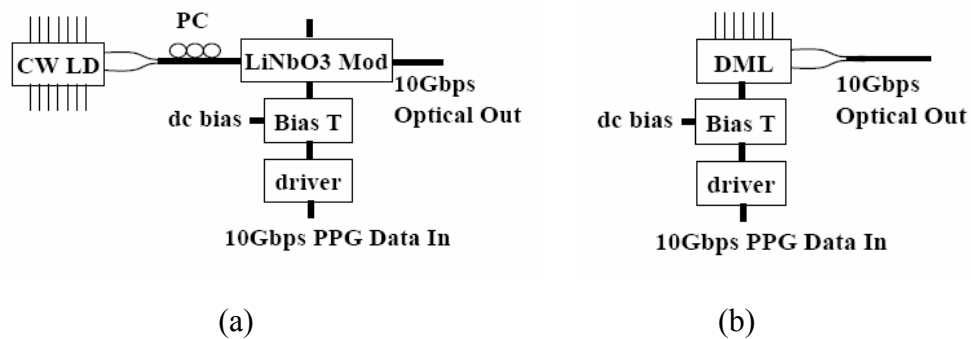


Fig.3.17 Electric-to-Optical (E/O) converter module : (a) For  $LiNbO_3$  external modulator. (b) For directly modulated laser.

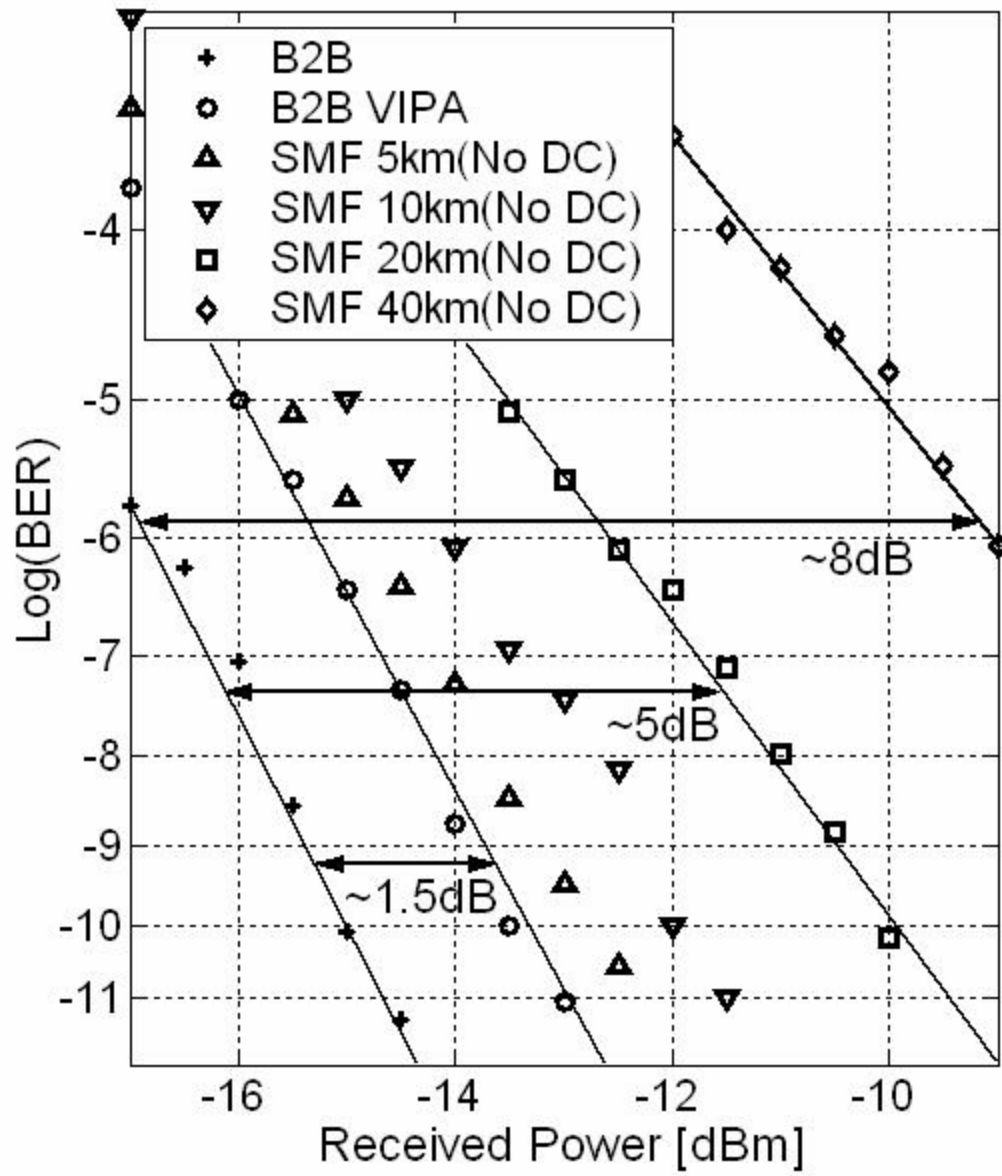
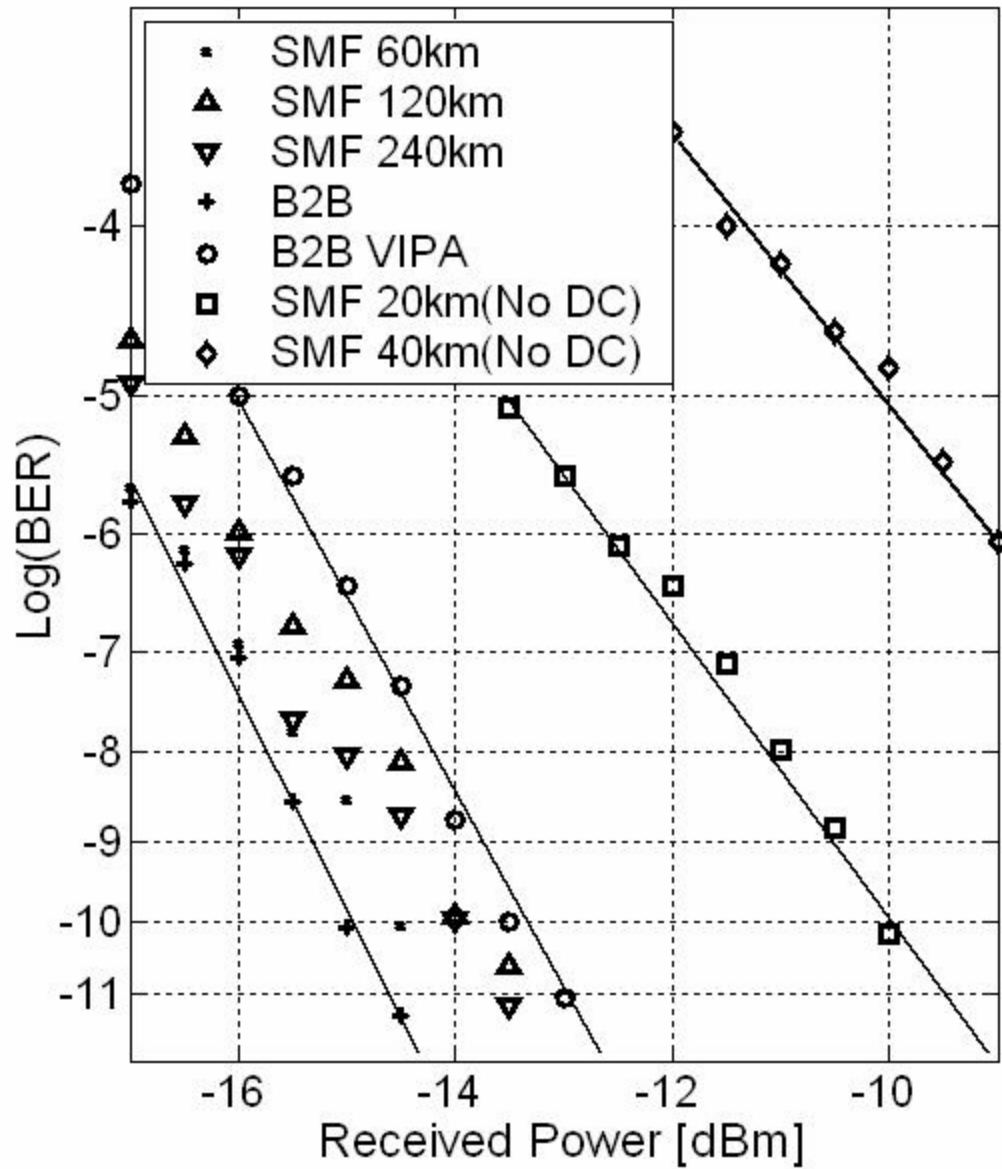


Fig.3.18(a)



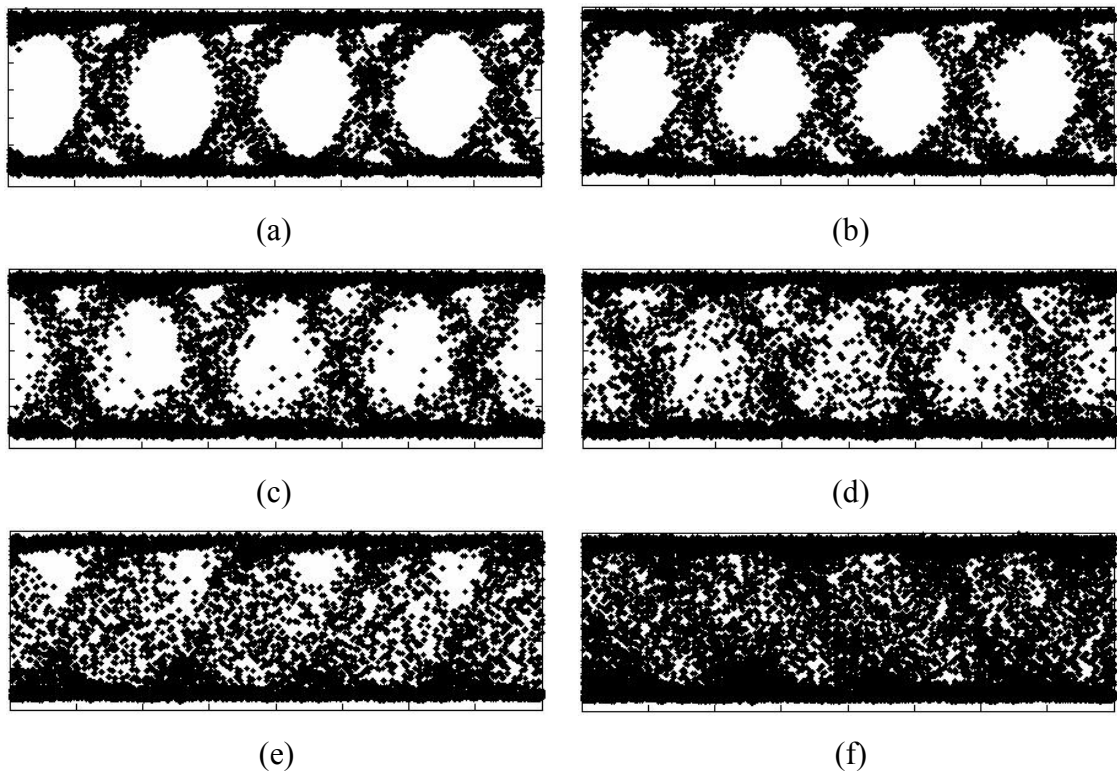


Fig.3.19 Eye diagrams before TDC compensation for a positively chirped 10-Gbps NRZ ( $2^{31}-1$ ) source (a) Back-to-Back (B2B). (b) After 20km SMF transmission. (c) After 40km SMF transmission. (d) After 60km SMF transmission. (e) After 120km SMF transmission. (f) After 240km transmission.

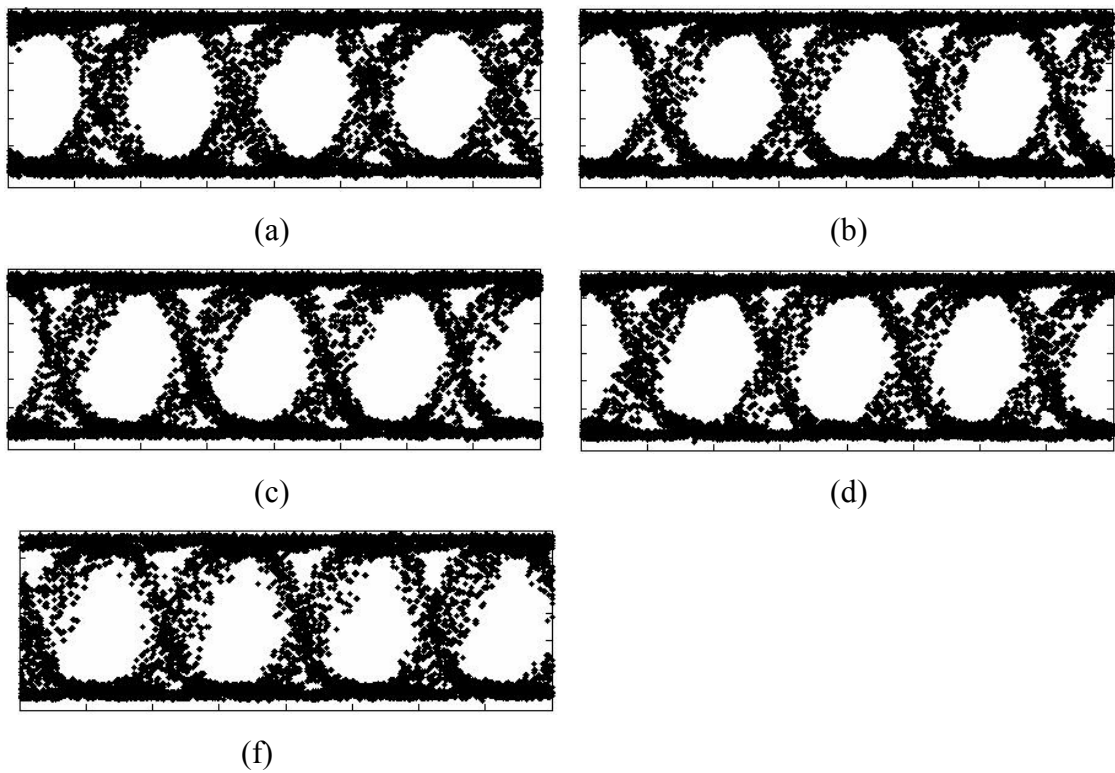


Fig.3.20 Eye diagrams after optimum TDC compensation for a positively chirped 10-Gbps NRZ ( $2^{31}-1$ ) source. (a) 20km SMF transmission and compensation (-340 ps/nm). (b) 40km SMF transmission and compensation (-680 ps/nm). (c) 60km SMF transmission and compensation (-1020 ps/nm). (d) 120km SMF transmission and compensation (-2040 ps/nm). (e) 240km SMF transmission and compensation (-4080 ps/nm).

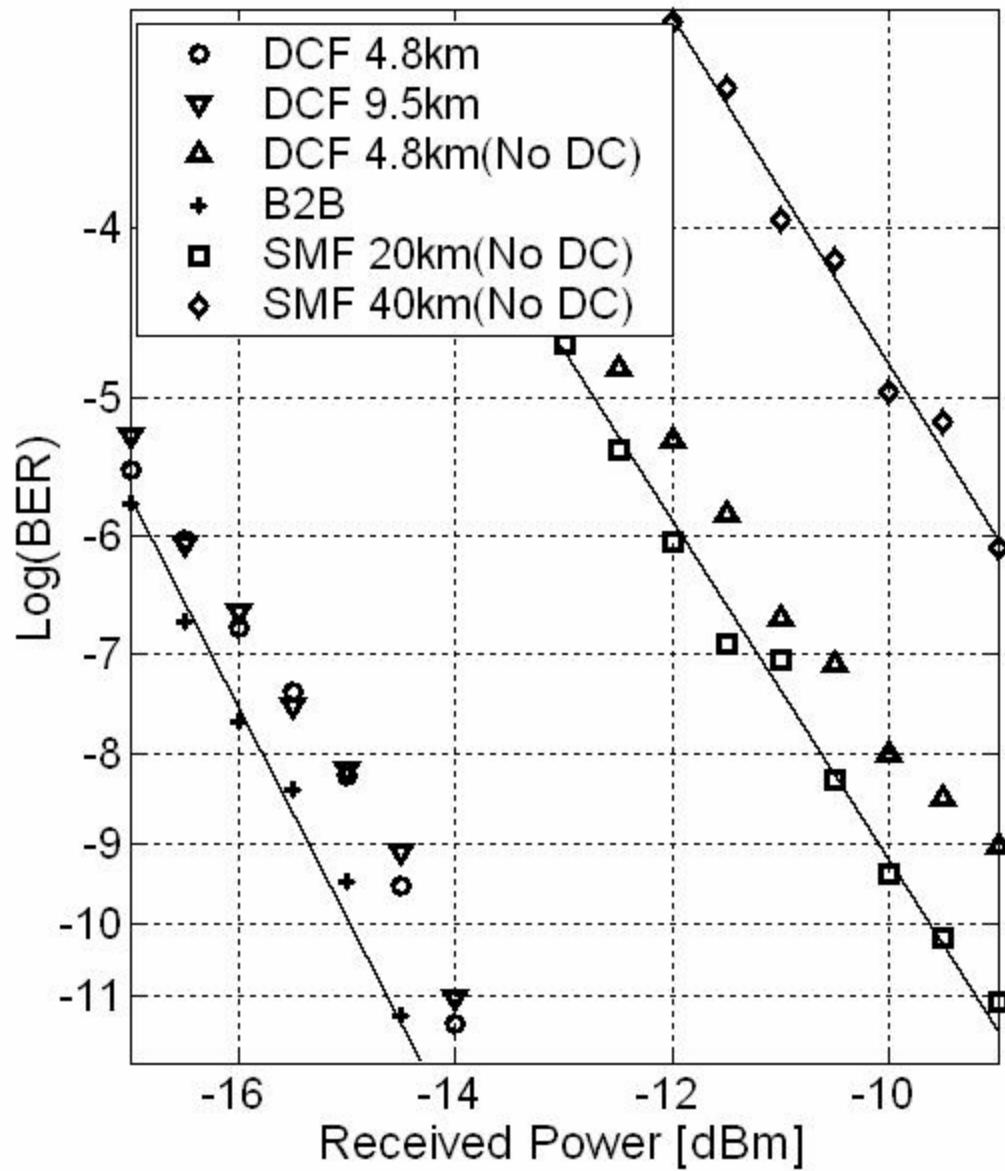


Fig.3.21 BER curves for a positively chirped 10-Gbps NRZ source transmitted along the various DCF spans with and without TDC compensation.

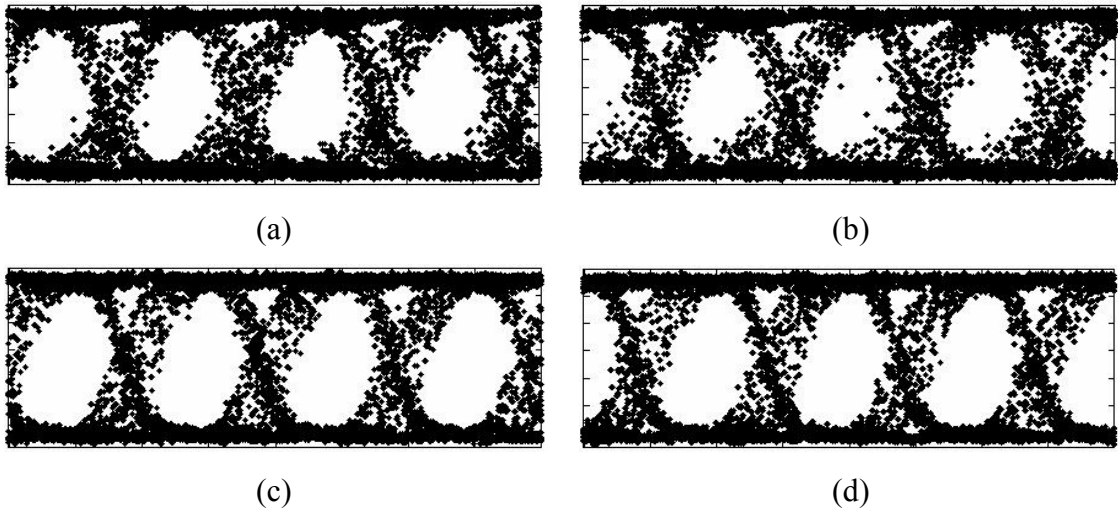


Fig.3.22 Eye diagrams of DCF transmission and compensation (a) 4.8km DCF transmission without TDC compensation. (b) 9.5km DCF transmission without TDC compensation. (c) 4.8km DCF transmission and compensation (+425 ps/nm). (d) 9.5km DCF transmission and compensation (+850 ps/nm).

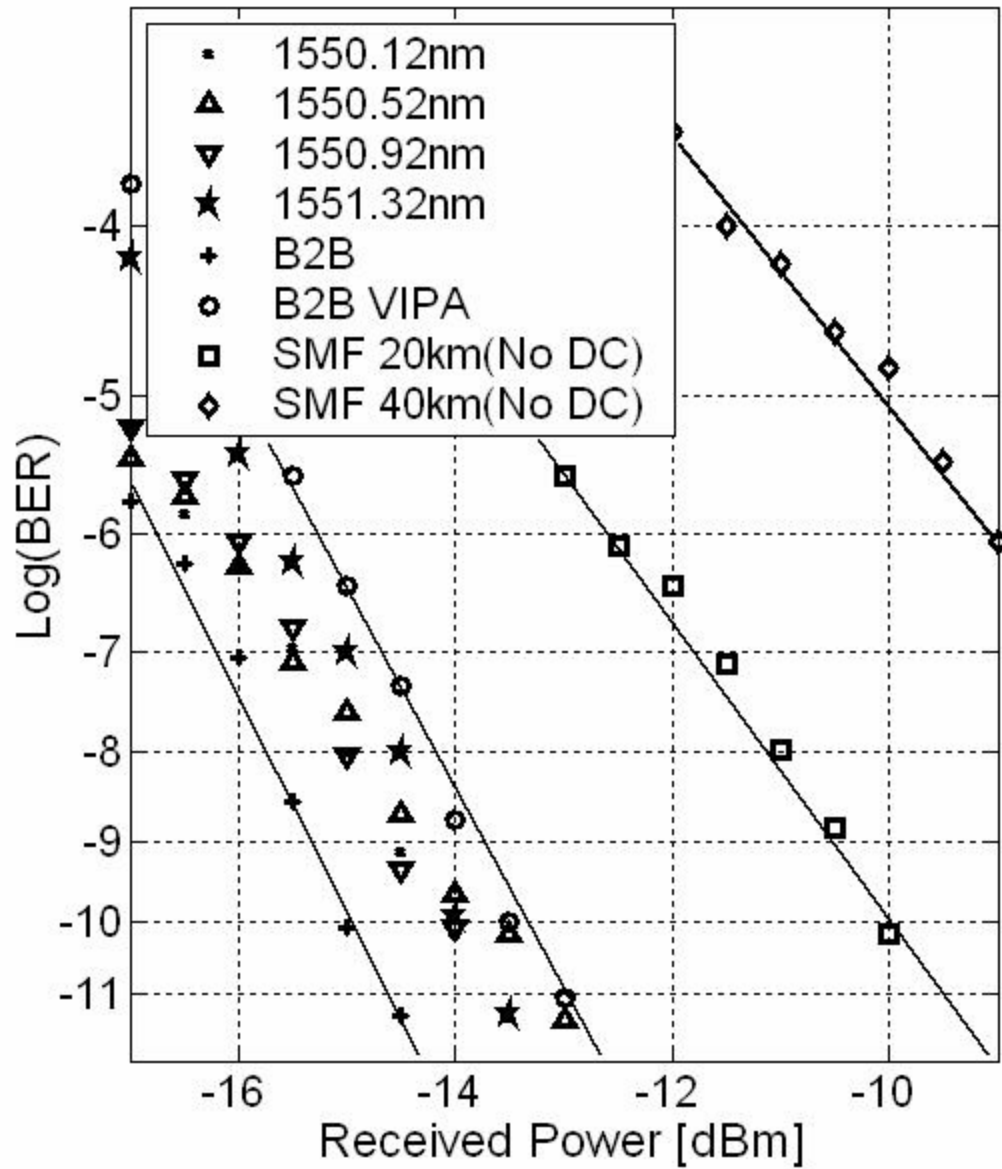


Fig.3.23 BER curves for a positively chirped 10-Gbps NRZ source transmitted along 240km SMF and compensated by TDC for several adjacent 50-GHz spaced ITU wavelength channels around 1550nm (1550.12, 1550.52, 1550.92, 1551.32nm).

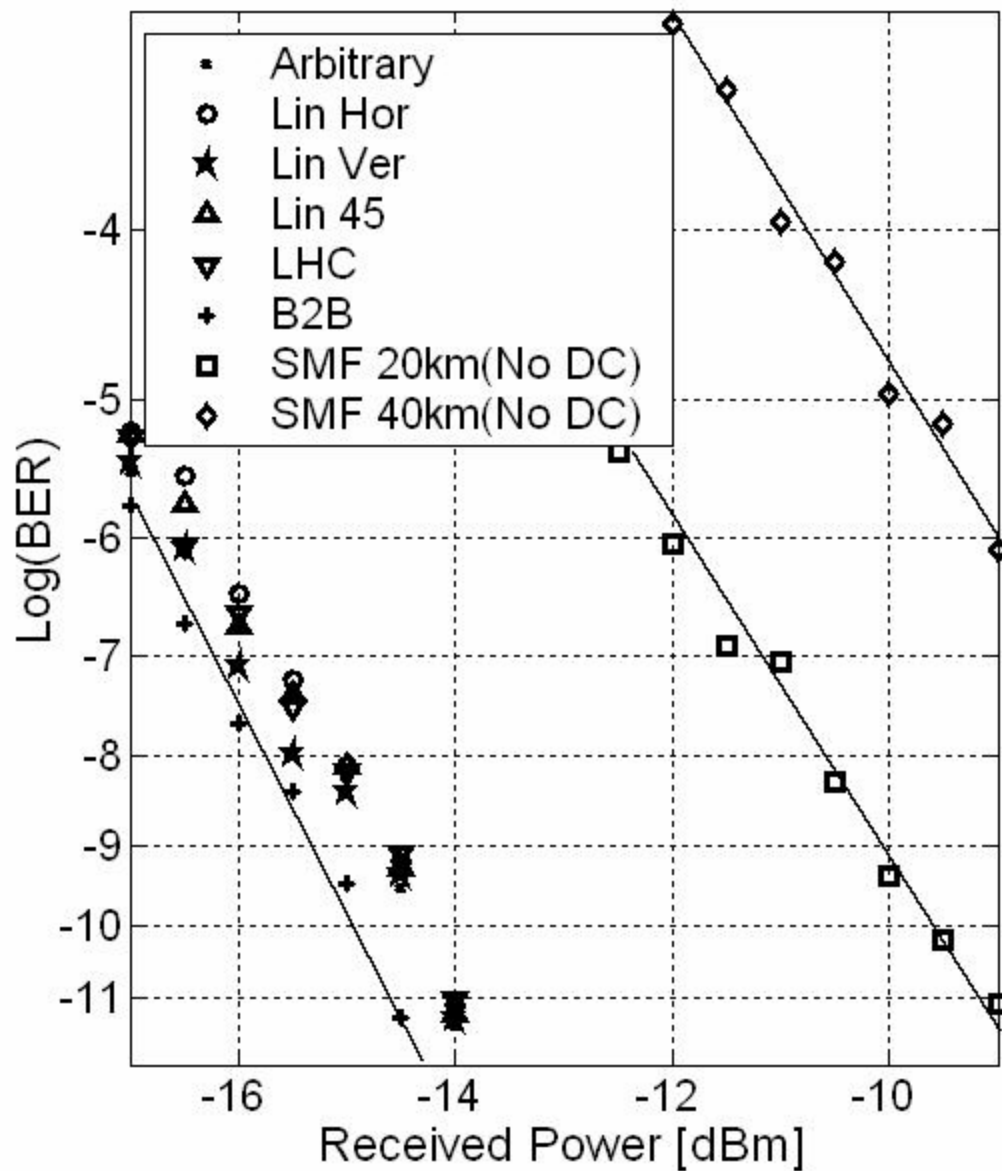


Fig.3.24 BER curves for a positively chirped 10-Gbps NRZ source transmitted along 240km SMF and compensated by TDC for five different polarization states (arbitrary elliptical, linear horizontal, linear vertical, linear 45-degrees, left hand circular).

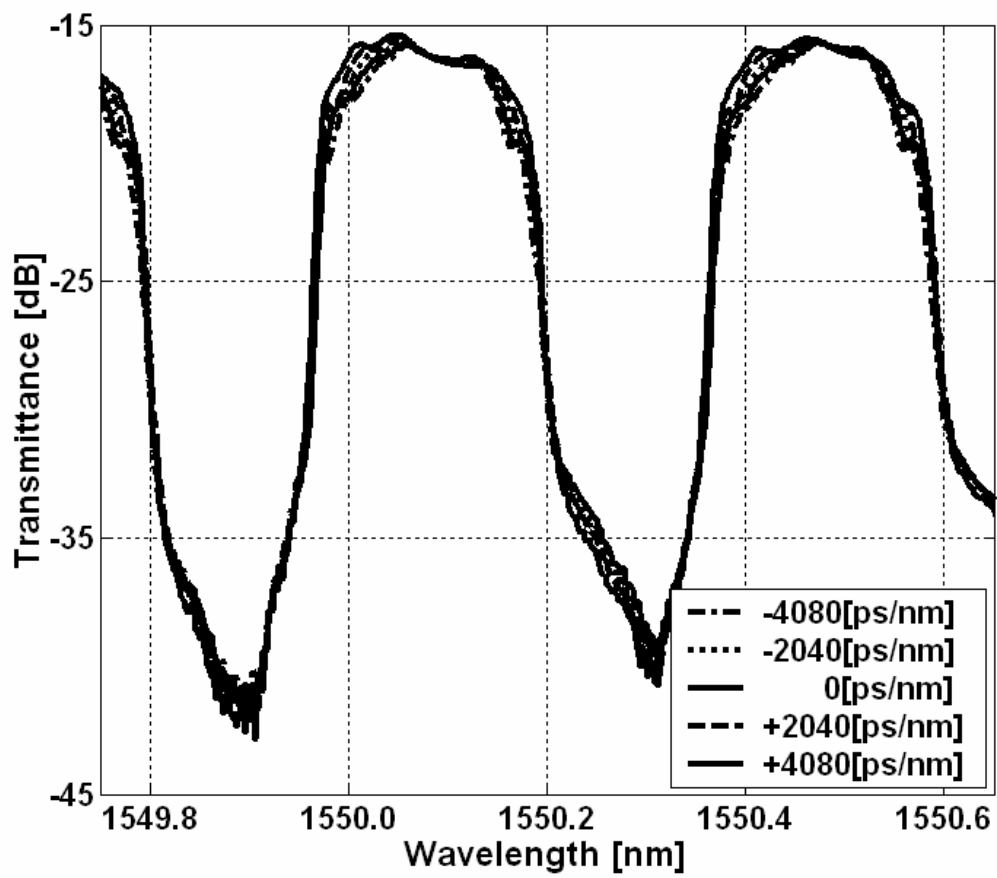


Fig.3.25(a)

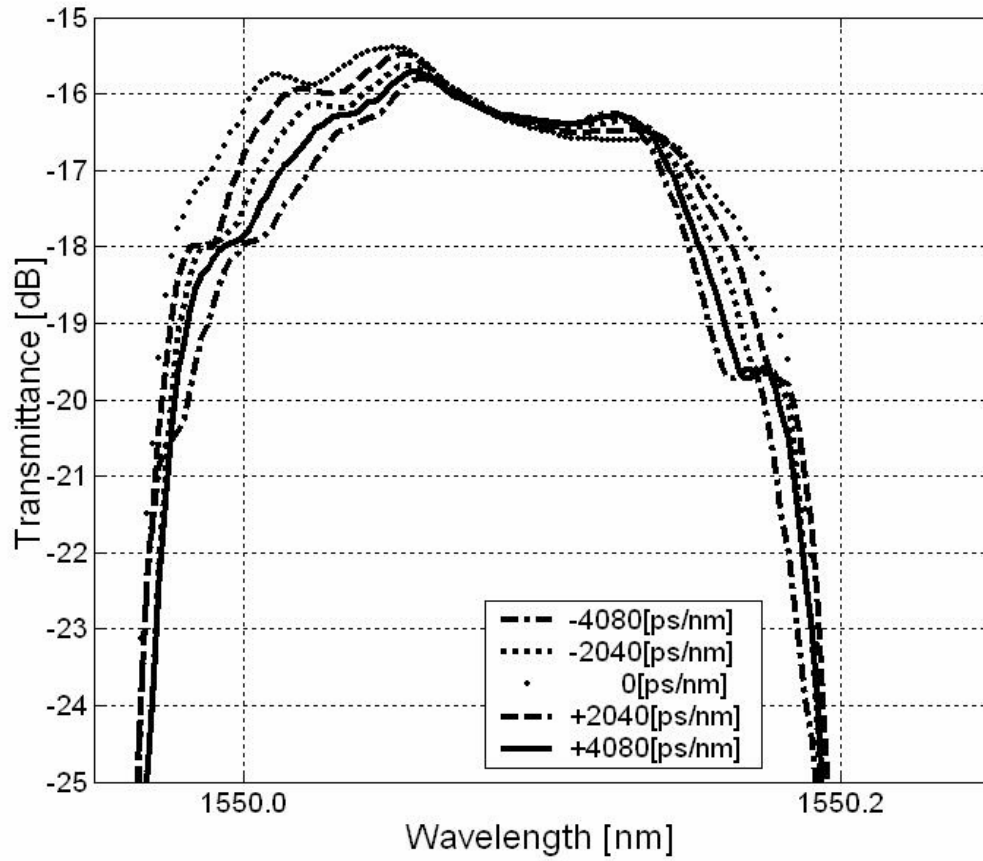
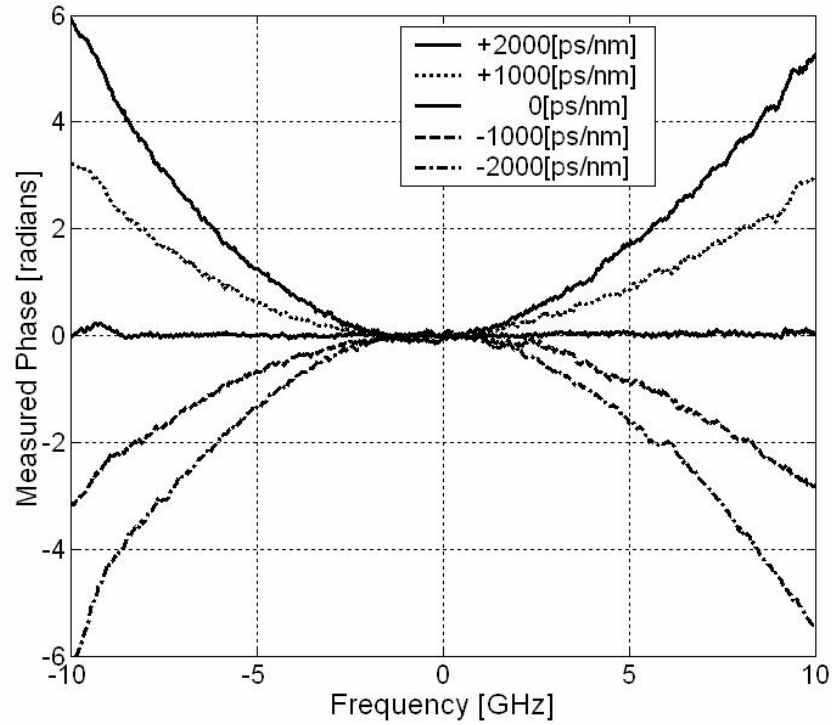
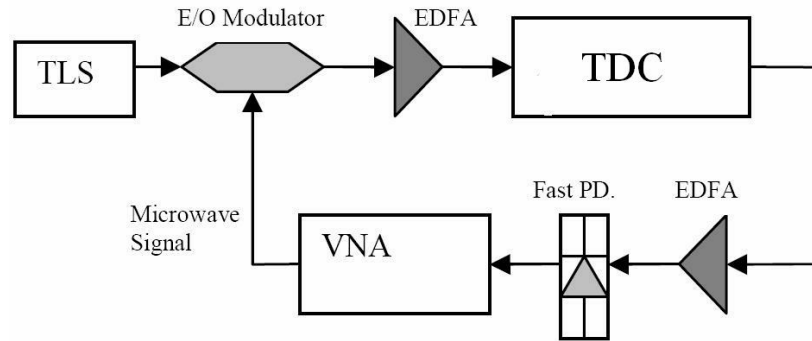


Fig.3.25(b)

Fig.3.25 (a) VIPA based TDC Transmission spectra with different dispersion settings ranging (from -4080 ps/nm to +4080 ps/nm). (b) Same figure as Fig. 3.25(a) with expanded axis.



(a)



(b)

Fig.3.26 (a) Measured phase response with different dispersion settings (from -2000 ps/nm to +2000 ps/nm) for TDC. (b) Experimental Setup.

Table 3.1  
Comparison of optical and electrical TDC.

Optical TDC	Advantage	<ul style="list-style-type: none"> <li>- Theoretically compensate linear optical impairments perfectly</li> <li>- Compensate many channels simultaneously</li> <li>- Power consumption independent of bit rate</li> </ul>
	Disadvantage	<ul style="list-style-type: none"> <li>- Compensation is linear only</li> <li>- Optics has cost disadvantage because of small market volumes</li> </ul>
Electrical TDC	Advantage	<ul style="list-style-type: none"> <li>- Compensation can readily be nonlinear</li> <li>- Electronics has cost advantage because of large market volumes</li> </ul>
	Disadvantage	<ul style="list-style-type: none"> <li>- Compensation after direct detection is imperfect because of loss of phase and polarization information (transmitter-based or coherent-detection electrical TDC do have phase information, but have added complexity)</li> <li>- Compensate only one channel at a time</li> <li>- Power consumption increases with bit rate</li> <li>- Electronics becomes more and more difficult as bit rate increases</li> </ul>

Table 3.2  
Characteristics of optical TDC technologies.

Technology	Insertion loss	Channel spacing	Nonlinear effect	Tuning speed	Difficult challenge
DCF	0.2 dB/km	Any	High	Not tunable	Fabrication
FBG	~ 4dB	Fixed	Low	~ 1ms	Grating design, Piezo stability
AWG	~ 10dB	Fixed	Low	~ 100ms	Packaging, Control
MZI	~ 10dB	Fixed	Low	~ 100ms	Packaging, Control
VIPA	~ 15dB	Fixed	Low	~ 10ms	Coating, Alignment

Table 3.3  
Comparison of optical TDC technologies.

Sector	Technology	Tuning Range [ps/nm]	BW [GHz]	FOM (norm.)	Ref.
MEMS	MEMS	-4.6 ~ -16.7 (12)	400	1.92	[8]
Etalon	GT-etalon	-200 ~ +200 (400)	20	0.16	[9]
	Multicavity etalon	-220 ~ +200 (440)	80	2.81	[10]
	Multicavity etalon	-800 ~ +800 (1600)	25	1.00	[11]
		-1500 ~ +1700 (3200)	25	2.00	
		-500 ~ +500 (1000)	30	0.91	
	Cascaded single cavity	-500 ~ +500 (1000)	20	0.40	[12]
Coupled cavity etalon	-300 ~ +400 (700)	NA	NA	[13]	
FBG	Polymer FBG (simulation)	-110 ~ -2400 (2200)	NA	NA	[14]
	Dual FBG, thermal strain	-180 ~ -380 (200)	NA	NA	[15]
	Piezoelectric actuator	-100 ~ -600 (500)	62.5	1.95	[16]
	Bending metal support beam	SMF 100km (1500)	100	15.00	[17]
		-400 ~ +400 (800)	100	8.00	
	Stretcher	-300 ~ -700 (400)	100	4.00	[18]
		-300 ~ +300 (600)	100	6.00	
	Thermal strain	-370 ~ -1420 (1050)	23	0.55	[19]
	Stretcher & thermal strain	-178 ~ -302 (130)	150	2.92	[20]
	Mechanical bending	-495.5 ~ -1406 (910)	NA	NA	[21]
	Magnetic Field	-188 ~ -472 (280)	200	11.20	[22]
Mechanical strain	-290 ~ -730 (440)	100	4.40	[23]	

Table 3.3  
Comparison of optical TDC technologies (continued).

Sector	Technology	Tuning Range [ps/nm]	BW [GHz]	FOM (norm.)	Ref.
PLC	WGR	-200 ~ +200 (400)	100	4.00	[24]
		-500 ~ +500 (1000)	100	10.00	[25]
	WGR (OFC 2006, PDP10)	-1125 ~ +150 (1375)	25	0.85	[26]
	MZI interferometer	SMF 200km (3400)	25	2.12	[27]
	3 stage MZI interferometer	SMF 180km (3060)	50	7.65	[28]
		-200 ~ +200 (400)	100	4.00	
3 stage MZI interferometer	SMF 225km (3825)	25	2.39	[29]	
Ring resonator	SMF 185km (3000)	50	7.50	[30]	
VIPA	3-D mirror (JLT 2002)	-650 ~ +650 (1300)	100	13.00	[32]
	3-D mirror (ECOC 2000)	-800 ~ +800 (1600)	100	16.00	[33]
	SLM (Our Work)	-4080 ~ +850 (4900)	50	12.25	

## 4. RETURN-TO-ZERO LIGHTWAVE TRANSMISSION WITH VIPA BASED PULSE SHAPER

### 4.1 Introduction

The choice of modulation format has an important performance/economic trade-off. From a performance standpoint, the best modulation format is dictated by many system parameters, such as system length, the fiber type, the dispersion management, and the optical bandwidth. One of the key challenges of the system design is to transmit a pulse shape that will survive the long transmission distance in the presence of dispersion, fiber nonlinearity and the added optical noise from the amplifiers [1].

Transmission based on this simple on/off pulse scheme is referred to a unipolar pulse system. When the shape of the light pulse used is a rectangular pulse that occupies the entire bit period, the format is referred to as a Non-Return-to-Zero (NRZ) format. A string of binary data with optical pulses that do not occupy the entire bit period are described generically as Return-to-Zero (RZ). Much attention has been focused recently on the use of RZ signaling [1] because of its demonstrated improved immunity to fiber nonlinearities related to NRZ [1, 68]. If rectangular pulses were generated with a pulse width half the bit time, their spectral occupancy would be twice that of NRZ, as the first nulls in the frequency domain would occur at  $\pm 2B$ , relative to the optical carrier, and their potential spectral efficiency would be one half that of NRZ signals. But as the RZ format occupies twice the spectral width of NRZ format, it will be more severely effected by the chromatic dispersion.

Previous works on tunable dispersion compensation for RZ signal transmissions include nonlinearly-chirped fiber Bragg grating [69] and multicavity etalon [10] based TDC. However the tuning range of these works is limited to  $\pm 250$  ps/nm. In the

previous chapter, we have demonstrated a TDC capable of producing a tuning range of  $-4080 \sim +850$  ps/nm using the transmission setup with 10-Gbps positively chirped NRZ signals. Here, we extend our work to demonstrate tunable chromatic dispersion compensation for 10-Gbps Return-to-Zero (RZ) signal transmissions with different pulse durations using standard SMF upto 100-km ( $-1700$ ps/nm).

## 4.2 Experiments And Results

We composed a RZ signal transmission setup as shown in Fig.4.1 to measure the TDC performance in terms of the dispersion power penalty. The VIPA based TDC is explained in detail in Section 3.4.1. A pulse-width and wavelength tunable RZ transmitter producing 10-Gbps RZ signals is used as the optical source [70,71]. This tunable RZ transmitter includes a 10-GHz actively mode-locked fiber laser and a high resolution grating based pulse shaper which is able to resolve individual spectral lines generated from the mode-locked laser. This line-by-line pulse shaper functions as a wavelength and bandwidth tunable high resolution optical filter for precise spectral line-by-line control. By appropriately setting the pulse shaper, width and wavelength tunable pulses can be achieved, in which the wavelength is determined by the passband of the pulse shaper and the pulse width is determined by the number of spectral lines passing through the pulse shaper. These pulses are passed through a standard intensity modulator for on-off keying at 10-Gbps. This results in a pulse-width tunable RZ transmitter. The RZ transmitter was composed by one of my collaborators Zhi Jiang.

In the experiment, the RZ transmitter was tuned for  $\sim 1550.1$ nm center wavelength to match the TDC passband as shown in Fig.4.2. The pulse duration was tuned to produce  $\sim 30$ ps pulses ( $\sim 33\%$  RZ) as shown in Fig.4.5(a) (also shown in the inset of Fig.4.1) and  $\sim 50$ ps pulses ( $\sim 50\%$  RZ) as shown in Fig.4.5(d). Two EDFAs were used to compensate the optical power loss within the system link, various lengths of fiber spools were used to generate different dispersions (20km  $\sim$  100km SMF with  $D = +17$  ps/nm-km) to prove

the tunability of TDC, and variable optical attenuators were placed after the fiber spools to fix the insertion loss within the fiber links to 26-dB in order to maintain constant power at the second optical amplifier input for different fiber lengths. An optical bandpass filter (BPF) with  $\sim 2$ nm passband was used to remove optical amplifier noise and a 10-GHz photodiode was used to detect the optical signal for BER measurements.

Fig.4.3(a) shows the BER for back-to-back operation without the TDC setup (B2B) and with the TDC setup but with the SLM phase set to a constant (B2B VIPA), and for 20km, 30km, and 40km of SMF transmission without dispersion compensation (without TDC setup) using the RZ transmission setup with  $\sim 33$ ps pulse duration in inset of Fig.4.1. The dispersion power penalties for 20km, 30km, and 40km of SMF transmission are 3dB, 6dB, and 10dB, respectively. Fig.4.3(b) shows the BER results when the TDC is optimized for various SMF spans up to 100km for 33% RZ data by programming the appropriate quadratic phase function onto the SLM. The results in the figure show error-free transmission, with the power penalty kept below 1-dB in all cases. For comparison the figure also shows the BER without the TDC setup for a 20km uncompensated SMF span that is identical to the curve in Fig.3a. We also have obtained very similar (error-free) results using our TDC (same setting for given span length) for 50% RZ signal transmission over spans up to 100km as shown in Fig.4.4.

Fig.4.5 shows the typical eye diagrams (another key optical transmission performance gauge) for back-to-back, and for 100km SMF transmission both before and after chromatic dispersion compensation 33% RZ (Fig.4.5(a)-(c)) and 50% RZ (Fig.4.5(d)-(f)) signals. Fig.4.5(a) and 4.5(d) show the back-to-back results for the 33% RZ and 50% RZ signals which were measure by using 50-GHz photodiode and 50-GHz bandwidth sampling oscilloscope. Fig.4.5(b) and 4.5(e) show the results for 100km SMF transmission before the TDC compensation using a 10-GHz photodiode (which was used to measure the BER in Fig.4.3). The eye diagrams are completely closed in both cases. Fig.4.5(c) and 4.5(f) show the chromatic dispersion compensated results for 100km SMF transmission with the TDC using a 10-GHz photodiode (which was used to measure the BER in Fig.4.3). The clear eye openings in these results show the accumulated

dispersions are effectively removed by the TDC, which is consistent with the BER results in Fig.4.3(b). These results clearly indicate the effectiveness of the TDC compensation for different pulse durations.

Both the BER curves and eye diagrams remain well behaved over the full range of fiber lengths and dispersion tested, and for both 33% and 50% RZ formats. The reason for performing TDC compensation up to 100km SMF was due to the accumulated optical amplifier noise (amplifier spontaneous emission (ASE) noise) within the transmission link rather than the TDC compensation capability itself. This can easily be resolved by using the additional optical filters (i.e. ASE rejection filters) after every one or two fiber spans within the transmission link. Therefore, the extension to compensation of even larger amounts of dispersion should be possible.

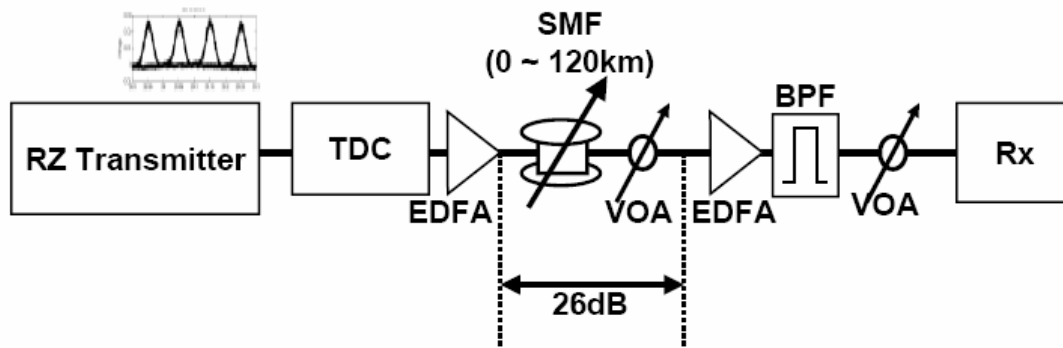


Fig.4.1 Schematic diagram for the experimental setup for RZ lightwave transmission.

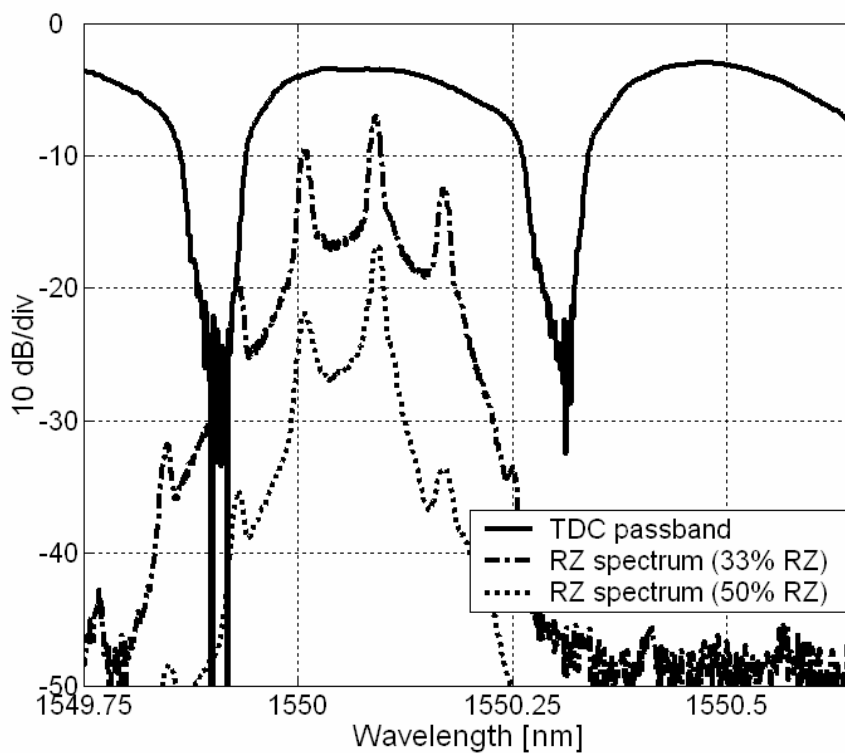


Fig.4.2 TDC transmittance and optical spectrum for the optically generated RZ signal with different pulse durations.

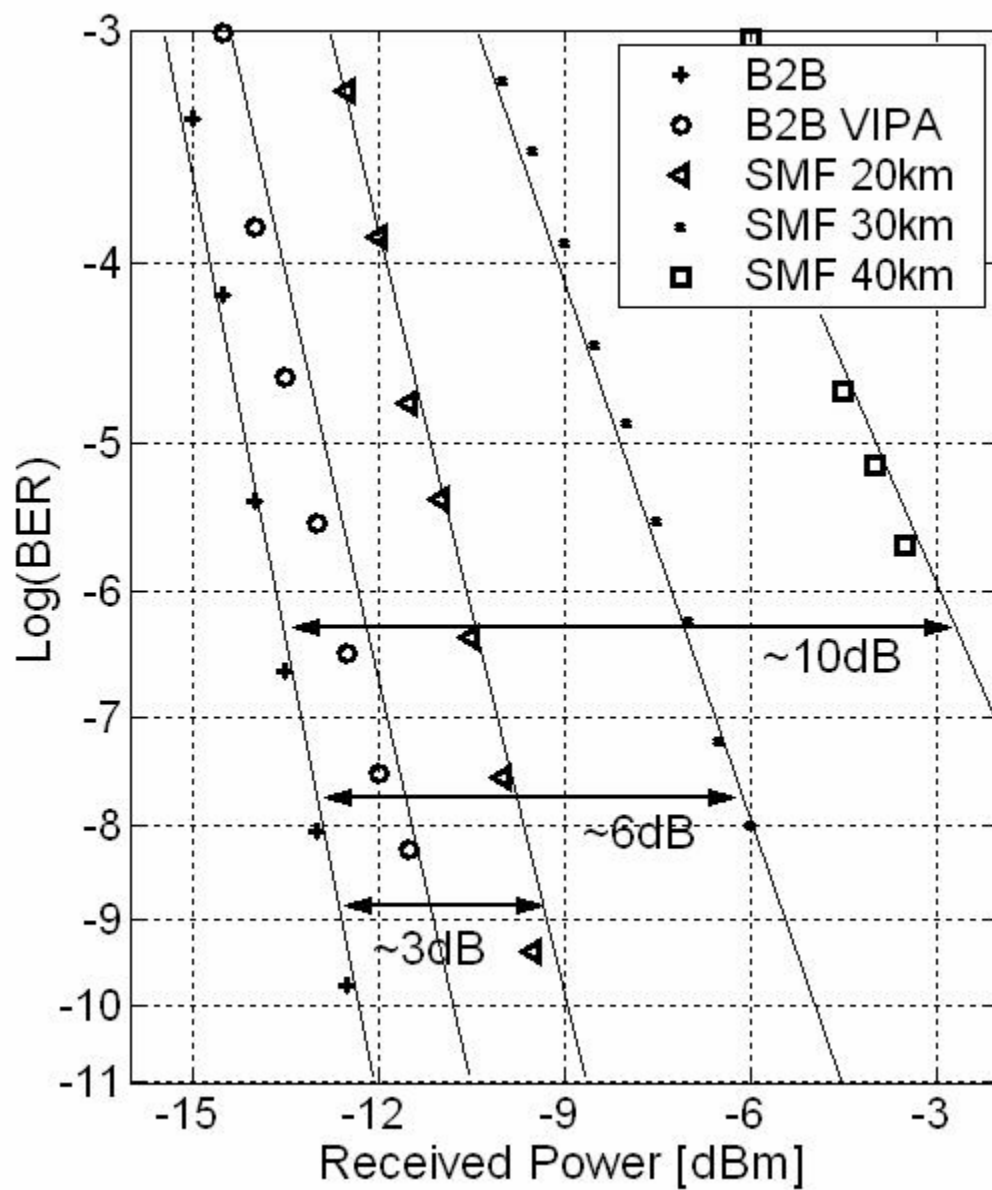


Fig.4.3(a)

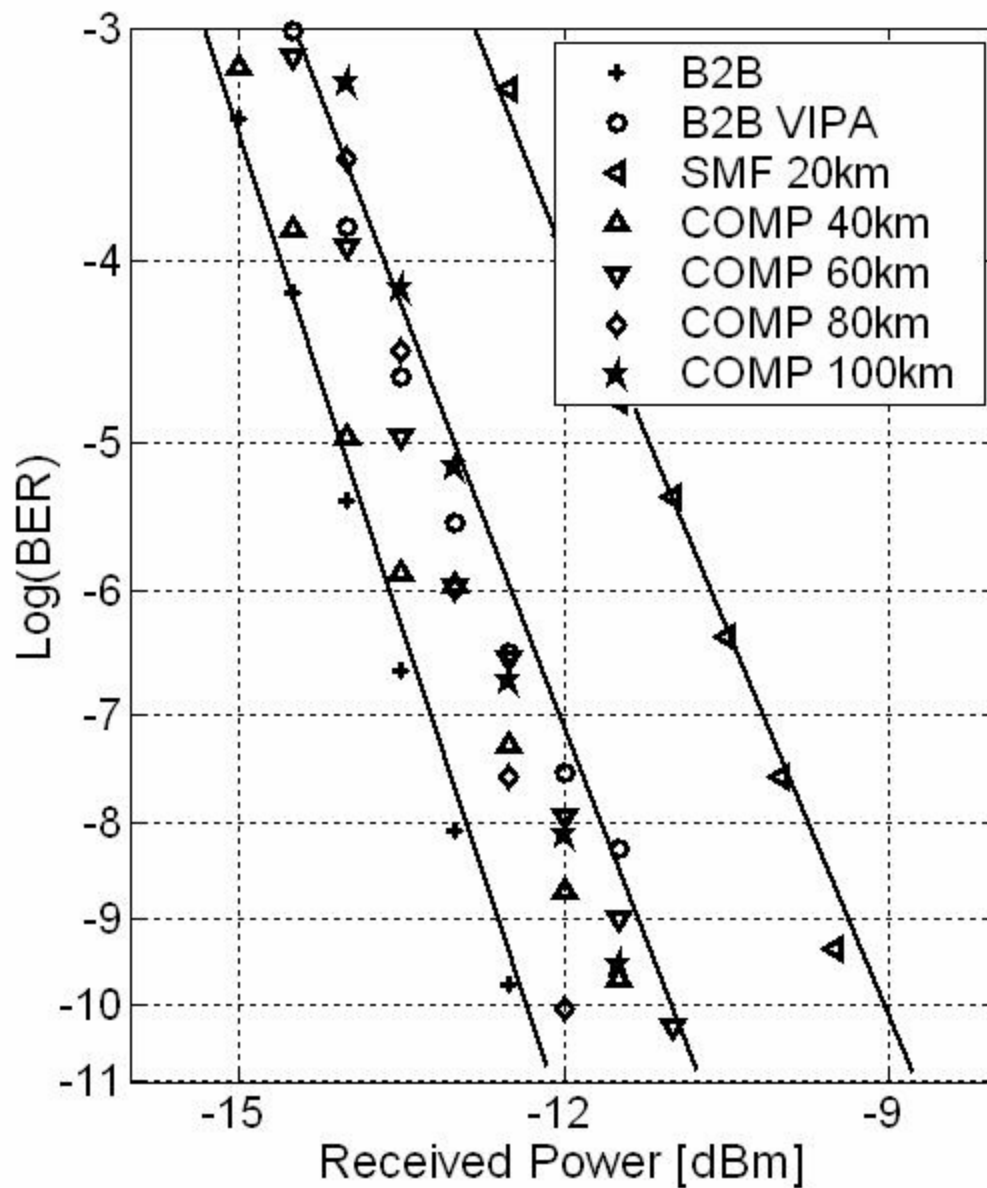


Fig.4.3(b)

Fig.4.3 TDC measurements using 33% RZ signal source : (a) BER vs received power without TDC. (b) BER vs received power after TDC optimum compensation.

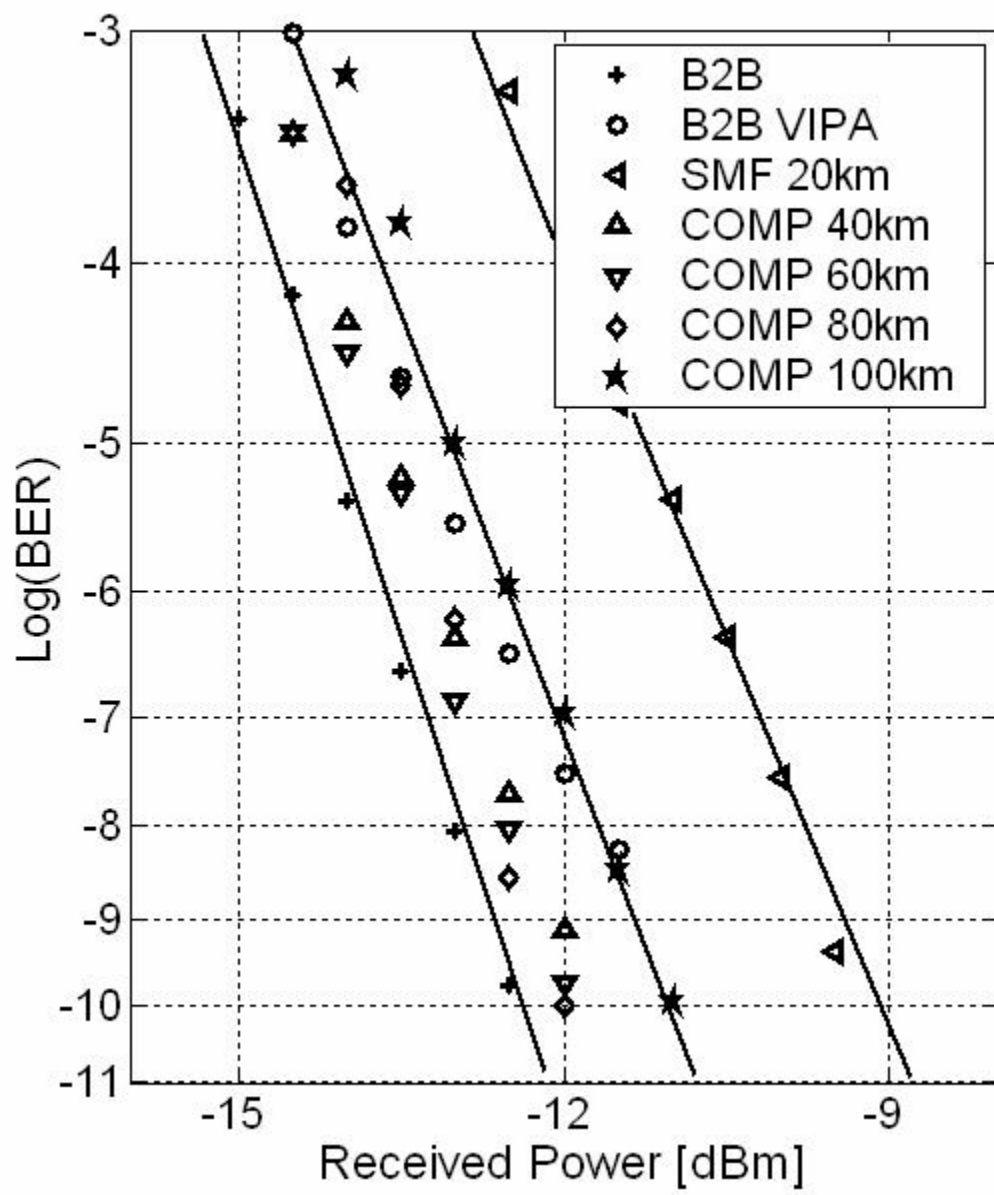


Fig.4.4 TDC measurements : BER vs received power after TDC optimum compensation for 50% RZ signal source.

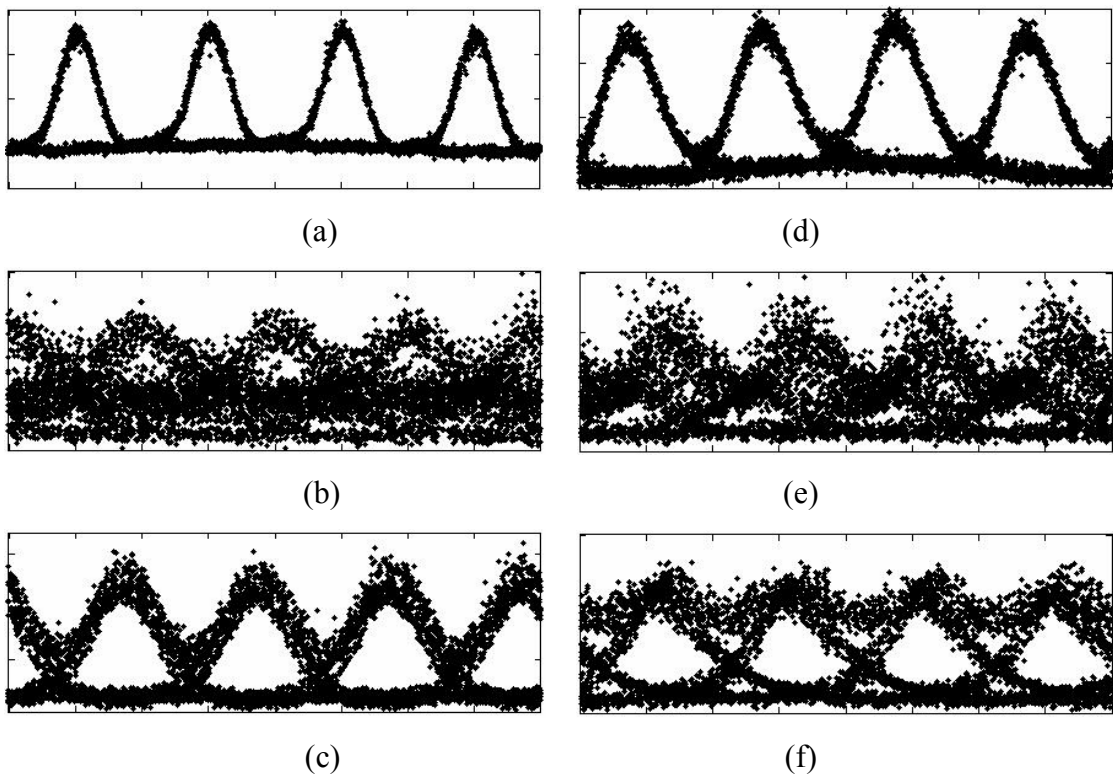


Fig.4.5 Eye diagrams for 10-Gbps RZ source : (a) For 33% RZ, back-to-back without TDC (measured by 50-GHz PD). (b) For 33% RZ, 100km SMF transmission without TDC. (c) For 33% RZ, 100km SMF transmission with optimum compensation by TDC. (d) For 50% RZ, back-to-back without TDC (measured by 50-GHz PD). (e) For 50% RZ, 100km SMF transmission without TDC. (f) For 50% RZ, 100km SMF transmission with optimum compensation by TDC

## 5. CONCLUSION

We have demonstrated an optical tunable dispersion compensator (TDC) using Virtually-Imaged Phased-Array (VIPA) based Fourier transform pulse shaper. The TDC can provide accurate chromatic dispersion compensation of  $-4080 \sim +850$  ps/nm with 50-GHz spaced WDM capability and polarization independence. We performed the evaluation of the TDC using a positively chirped 10-Gbps nonreturn-to-zero (NRZ) data signals over a range of 0 to 240 km SMF and 0 to 9.5 km DCF. Our results correspond to full tunable dispersion compensation of 3x more SMF than previously reported results and should be expected to provide a tuning range of  $\pm 4080$  ps/nm without changes to the compensator setup. This is, to our best knowledge, the largest tuning range achieved for an optical TDC with WDM capability. Furthermore, because both the transmission spectra and the BER curves remain well behaved over the full range of fiber lengths and dispersion tested, we believe that extension to compensation of even larger amount of dispersion is possible.

We have extended our tunable chromatic dispersion compensation experiments with different modulation formats (10-Gbps RZ lightwave transmission with different pulse durations). 33% RZ and 50% RZ formats have been evaluated using optical transmission link upto 100km SMF ( $-1700$  ps/nm). We achieved error-free transmission upto 100km SMF and no signs of spectral distortions were observed, we believe that extension to compensation of larger amount of dispersion is possible in different modulation formats.

We also have demonstrated optical pulse burst manipulations using similar VIPA based Fourier transform pulse shaping apparatus. Because we used ultrashort pulses with spectra broader than the free spectral range in this application, the spatial phase function applied with the pulse shaper is replicated periodically onto the optical spectrum. The result is that the pulse shaper output is a burst of pulses, with the pulse spacing equal to

the inverse of the VIPA free spectral range. The intensities of the individual pulses in the burst are determined by a temporal envelope function obtained from the inverse Fourier transform of the applied spatial phase function. These effects arise specifically because of the periodic spectral dispersion provided by the VIPA and have not been observed with grating based Fourier transform pulse shapers. Our experimental data are in good agreement with simulations. Our VIPA based Fourier transform pulse shaping scheme also holds promise for programmable optical waveform synthesizers (as well as optical TDC) with finer spectral resolution than conventional grating-based pulse shapers.

## LIST OF REFERENCES

## LIST OF REFERENCES

- [1] I. Kaminow and T. Li, "Optical fiber telecommunications IVB, systems and impairments," 4<sup>th</sup> ed. An Elsevier Science Imprint, California, Academic Press, 2002.
- [2] A.M.Weiner, "Femtosecond optical pulse shaping and processing," *Prog. Quantum Electron.*, vol.19, no.3, pp161-238, 1995.
- [3] A.M.Weiner, "Femtosecond pulse shaping using spatial light modulators," *Rev. Sci. Instrum.* vol.71, pp1929-1960, 2000.
- [4] T.Kurokawa, H.Takenouchi, and H.Tsuda, "Terabit optical signal processing based on time-space-conversion," in *LEOS'99 12th Annual Meeting, IEEE*, vol.1, pp188-189, 1999.
- [5] H.Tsuda, K.Okamoto, T.Ishii, K.Naganuma, Y.Inoue, H.Takenouchi, and T.Kurokawa, "Second- and third-order dispersion compensator using a high-resolution arrayed-waveguide grating," *IEEE Photonics Technology Letters*, vol.11, pp569-571, 1999.
- [6] M.Shirasaki, "Large angular dispersion by a virtually imaged phased array and its application to a wavelength demultiplexer," *Optics Letters*, vol.21, pp.366-368, 1996.
- [7] S.Xiao, A.M.Weiner, and C. Lin, "A dispersion law for virtually imaged phased-array spectral dispersers based on paraxial wave theory," *IEEE Journal of Quantum Electronics*, vol.40, pp.420-426, 2004.
- [8] T.Sano, T.Iwashima, M.Katayama, T.Kanie, M.Harumoto, M.Shigehara, H.Suganuma, and M.Nishimura, "Novel multichannel tunable chromatic dispersion compensator based on MEMS and diffraction grating," *IEEE Photonics Technology Letters*, vol. 15, pp. 1109-1100, 2003.
- [9] X.Shu, K.Sugden, P.Rhead, J.Mitchell, I.Felmeri, G.Lloyd, K.Byron, Z.Huang, I.Khrushchev, and I.Bennion, "Tunable dispersion compensator based on distributed Gires-Tournois etalons," *IEEE Photonics Technology Letters*, vol.15, no.8, pp.1111-1113, 2003.

- [10] L.M.Lunardi, D.J.Moss, S.Chandrasekhar, L.L.Buhl, M.Lamont, S.McLaughlin, G.Randall, P.Colbourne, S.Kiran, and C.A.Hulse, "Tunable dispersion compensation at 40-Gb/s using a multicavity etalon all-pass filter with NRZ, RZ, and CS-RZ modulation," *IEEE Journal of Lightwave Technology*, vol.20, no.12, pp.2136-2144, 2002.
- [11] D.J.Moss, M.Lamont, S.McLaughlin, G.Randall, P.Colbourne, S.Kiran, and C.A.Hulse, "Tunable dispersion and dispersion slope compensators for 10 Gb/s using all-pass multicavity etalons," *IEEE Photonics Technology Letters*, vol.15, no.5, pp.730-732, 2003.
- [12] B.J.Vakoc, W.V.Sorin, and B.Y.Kim, "A tunable dispersion compensator comprised of cascaded single-cavity etalon," *IEEE Photonics Technology Letters*, vol. 17, pp. 1043-1045, 2005.
- [13] X.Shu, K.Sugden, and I.Bennion, "Optically tunable dispersion compensator based on coupled-cavity etalon structure," *Optical Fiber and Communication (OFC) Conference*, OWO6, 2005.
- [14] H.Y.Liu, H.B.Liu, G/D/Peng, and T.W.Whitbread, "Polymer fiber Bragg grating tunable dispersion compensation," *Optical Fiber and Communication (OFC) Conference*, OWO5, 2005.
- [15] K.Yoshiara, M.Takabayashi, S.Matsumoto, Y.Shimakura, and T.Sugihara, "Tunable dispersion compensator with twin chirped fiber gratings for polarization mode dispersion and chromatic dispersion," *Optical Fiber and Communication (OFC) Conference*, JWA21, 2005.
- [16] J.A.J.Fells, S.E.Kanellopoulos, P.J.Bennett, V.Baker, H.F.M.Pridde, W.S.Lee, A.J.Collar, C.G.Rogers, D.P.Goodchild, R.Feced, B.J.Pugh, S.J.Clements, and A.Hadjifotiou, "Twin fiber grating tunable dispersion compensator," *IEEE Photonics Technology Letters*, vol.13, no.9, pp.984-986, 2001.
- [17] Y.W.Song, D.Starodubov, Z.Pan, Y.Xie, A.E.Willner, and J.Feinberg, "Tunable WDM dispersion compensation with fixed bandwidth and fixed passband center wavelength using a uniform FBG," *IEEE Photonics Technology Letters*, vol. 14, pp. 1193-1195, 2002.
- [18] Z.Pan, Y.W.Song, C.Yu, Y.Wang, Q.Yu, J.Popelek, H.Li, Y.Li, and A.E.Willner, "Tunable chromatic dispersion compensation in 40-Gb/s systems using nonlinearly chirped fiber Bragg gratings," *IEEE Journal of Lightwave Technology*, vol.20, no.12, pp.2239-2246, 2002.

- [19] D.Gauden, E.Goyat, A.Mugnier, P.Lesueur, P.Yvernault, and D.Pureur, "A tunable four-channel fiber Bragg grating dispersion compensator," *IEEE Photonics Technology Letters*, vol.15, no.10, pp.1387–1388, 2003.
- [20] N.Q.Ngo, S.Y.Li, R.T.Zheng, S.C.Tjin, and P.Shum, "Electrically tunable dispersion compensator with fixed center wavelength using fiber Bragg grating," *IEEE Journal of Lightwave Technology*, vol.21, no.6, pp.1568-1575, 2003.
- [21] J.Kim, J.Bae, Y.-G.Han, S.H.Kim, J.-M.Jeong, and S.B.Lee, "Effectively tunable dispersion compensation based on chirped fiber Bragg gratings without central wavelength shift," *IEEE Photonics Technology Letters*, vol.16, no.3, pp.849–851, 2004.
- [22] J.Mora, B.Ortega, M.V.Andres, J.Capmany, J.L.Cruz, D.Pastor, and S.Sales, "Tunable dispersion device based on a tapered fiber Bragg grating and nonuniform magnetic fields," *IEEE Photonics Technology Letters*, vol.15, no.7, pp.951–953, 2003.
- [23] J.Mora, A.Diez, M.V.Andres, P.-Y. Fonjallaz, M.Popov, "Tunable dispersion compensator based on a fiber Bragg grating written in a tapered fiber," *IEEE Photonics Technology Letters*, vol.16, no.12, pp.2631–2633, 2004.
- [24] C.R.Doerr, L.W.Stulz, S.Chandrasekhar, and R.Pafchek, "Colorless tunable dispersion compensator with 400-ps/nm range integrated with a tunable noise filter," *IEEE Photonics Technology Letters*, vol.15, no.9, pp.1258–1260, 2003.
- [25] C.R.Doerr, D.M.Marom, M.A.Cappuzzo, E.Y.Chen, A.Wong-Foy, L.T.Gomez, and S.Chandrasekhar, "40-Gb/s colorless tunable dispersion compensator with 1000-ps/nm tuning range employing a planar lightwave circuit and a deformable mirror," *Optical Fiber and Communication (OFC) Conference*, PDP5, 2005.
- [26] C.R.Doerr, L.L.Buhl, M.A.Cappuzzo, E.Y.Chen, A.Wong-Foy, L.T.Gomez, R.Blum, and H.Bulthuis, "Polarization-independent tunable dispersion compensator comprised of a silica arrayed waveguide grating and a polymer slab," *Optical Fiber and Communication (OFC) Conference*, PDP9, 2006.
- [27] C.R.Doerr, M.Cappuzzo, A.Wong-Foy, L.Gomez, E.Laskowski, and E.Chen, "Potentially inexpensive 10-Gb/s tunable dispersion compensator with low polarization sensitivity," *IEEE Photonics Technology Letters*, vol.16, no.5, pp.1340–1342, 2004.

- [28] C.R.Doerr, S.Chandrasekhar, M.Cappuzzo, E.Chen, A.Wong-Foy, L.Gomez, S.Patel, and L.Buhl, "Two Mach-Zehnder-type tunable dispersion compensators integrated in series to increase bandwidth and/or range while maintaining single-knob control," *IEEE Photonics Technology Letters*, vol.17, no.4, pp.828–830, 2005.
- [29] C.R.Doerr, S.Chandrasekhar, L.L.Buhl, M.A.Cappuzzo, E.Y.Chen, A.Wong-Foy, and L.T.Gomez, "Tunable dispersion compensator with integrated wavelength locking," *Optical Fiber and Communication (OFC) Conference*, PDP9, 2005.
- [30] W.Chen, W.Chen, S.Chu, B.Little, J.Hryniewicz, D.Gill, O.King, F.Johnson, R.Davidson, K.Donovan, J.Gibson, H.Jiao, and G.Carter, "Compact, Full C-Band, Widely Tunable Optical Dynamic Dispersion Compensators," *Optical Fiber and Communication (OFC) Conference*, PDP8, 2006.
- [31] L.D.Garrett, A.H.Gnauck, M.H.Eiselt, R.W.Tkach, C.Yang, C.Mao, and S.Cao, "Demonstration of virtually-imaged phased-array device for tunable dispersion compensation in 16 x 10 Gb/s WDM transmission over 480 km standard fiber," *Optical Fiber and Communication (OFC) Conference*, vol.4, pp.187-189, 2000.
- [32] H.Ooi, K.Nakamura, Y.Akiyama, T.Takahara, T.Terahara, Y.Kawahata, H.Isono, and G.Ishikawa, "40-Gb/s WDM transmission with Virtually Imaged Phased Array (VIPA) variable dispersion compensator," *IEEE Journal of Lightwave Technology* vol. 20, pp. 2196-2203, 2002.
- [33] M.Shirasaki, et al., "Variable Dispersion Compensator using The Virtually Imaged Phased Array (VIPA) for 40-Gbit/s WDM Transmission Systems," *European Conference and Exhibition on Optical Communication (ECOC)*, Post-Deadline Papers 2.3, 2000.
- [34] C.-C.Chang, H.P.Sardesai, and A.M.Weiner, "Dispersion-free fiber transmission for femtosecond pulses using a dispersion-compensating fiber and a programmable pulse shaper," *Optics Letters*, vol. 23, pp. 283-285, 1998.
- [35] G.-H.Lee and A.M.Weiner, "Programmable optical pulse burst manipulation using a virtually imaged phased array (VIPA) based Fourier transform pulse shaper," *IEEE Journal of Lightwave Technology*, vol.23, pp.3916-3923, 2005.
- [36] A.M.Weiner and D.E.Leaird, "Generation of terahertz-rate trains of femtosecond pulses by phase-only filtering," *Optics Letters*, vol.15, pp51-53, 1990.

- [37] H.Wang, Z.Zheng, D.E.Leaird, A.M.Weiner, T.A.Dorschner, J.J.Fijol, L.J.Friedmann, H.Q.Nguyen, and L.A.Palmaccio, "20-fs pulse shaping with a 512-element phase-only liquid crystal modulator," *IEEE Journals on Selected Topics in Quantum Electronics*, vol.7, no.4, pp.718-727, 2001.
- [38] D.E.Leaird, S.Shen, A.M.Weiner, A.Sugita, S.Kamei, M.Ishii, and K.Okamoto, "Generation of high-repetition-rate WDM pulse trains from an arrayed-waveguide grating," *IEEE Photonics Technology Letters*, vol.13, no.3, pp.221-223, 2001.
- [39] D.E.Leaird and A.M.Weiner, "Femtosecond direct space-to-time pulse shaping," *IEEE Journal of Quantum Electronics*, vol.37, no.4, pp.494-504, 2001.
- [40] M.M.Wefers and K.A.Nelson, "Space-time profiles of shaped ultrafast optical waveforms," *IEEE Journal of Quantum Electronics*, vol.32, pp.161-172, 1996.
- [41] C.C.Chang and A.M.Weiner, "Dispersion compensation for ultrashort pulse transmission using two-mode equalizer fibers," *IEEE Photonics Technology Letters*, vol.6, no.12, pp.1392-1394, 1994.
- [42] S.Etemad, T.Banwell, S.Galli, J.Jackel, R.Menendez, P.Toliver, J.Young, P.Delfyett, C.Price, and T.Turpin, "Optical-CDMA Incorporating Phase Coding Of Coherent Frequency Bins: Concept, Simulation, Experiment," *Optical Fiber and Communication (OFC) Conference*, FG5, 2004.
- [43] J.G.Proakis, "Digital Communications," 3<sup>rd</sup> ed., New York: McGraw-Hill, 1995
- [44] G.P.Agrawal, "Fiber-Optic Communication Systems," 3<sup>rd</sup> ed., Wiley-Interscience, 2002.
- [45] G.P.Agrawal, "Nonlinear Fiber Optics," 3<sup>rd</sup> ed., Academic Press, 2001.
- [46] G.P.Agrawal and M.J.Potasek, "Effect of frequency chirping on the performance of optical communication systems," *Optics Letters*, vol.11, no.5, pp.318-320, 1986.
- [47] A.F.Elrefaie, R.E.Wagner, D.A.Atlas, and D.G.Daut, "Chromatic dispersion limitations in coherent lightwave transmission systems," *IEEE Journal of Lightwave Technology*, vol.6, no.5, pp.704-709, 1988.
- [48] J.C.Cartledge and G.S.Burley, "The effect of laser chirping on lightwave system performance," *IEEE Journal of Lightwave Technology*, vol.7, no.3, pp.87-93, 1989.

- [49] B.W.Hakki, "Evaluation of transmission characteristics of chirped DFB lasers in dispersive optical fiber," *IEEE Journal of Lightwave Technology*, vol.10, no.7, pp.964-970, 1992.
- [50] R.A.Linke, "Modulation induced transient chirping in single frequency lasers," *IEEE Journal of Quantum Electronics*, vol.21, no.6, pp.593-597, 1985.
- [51] P.J.Corvini and T.L.Koch, "Computer simulation of high-bit-rate optical fiber transmission using single-frequency lasers," *IEEE Journal of Lightwave Technology*, vol.5, no.11, pp.1591-1595, 1987.
- [52] F.Koyama and K.Iga, "Frequency chirping in external modulators," *IEEE Journal of Lightwave Technology*, vol.6, no.1, pp.87-93, 1988.
- [53] A.H.Gnauck, S.K.Korotky, J.J.Veselka, J.Nagel, C.T.Kemmerer, W.J.Minford, and D.T.Moser, "Dispersion penalty reduction using an optical modulator with adjustable chirp," *IEEE Photonics Technology Letters*, vol.3, no.10, pp.916-918, 1991.
- [54] J.A.J.Fells, M.A.Gibbon, I.H.White, G.H.B.Thomson, R.V.Penty, C.J.Armistead, E.M.Kimber, D.J.Moule, and E.J.Thrush, "Transmission beyond the dispersion limit using a negative chirp electroabsorption modulator," *Electronics Letters*, vol.30, no.14, pp.1168-1169, 1994.
- [55] T.Kato, Y.Koyano, and M.Nishimura, "Temperature dependence of chromatic dispersion in various types of optical fibers," *Optical Fiber and Communication (OFC) Conference*, vol.1, pp.104-106, 2000.
- [56] C.Furst, C.Scheerer, G.Mohs, J.-P.Elbers, and C.Glingener, "Influence of the dispersion map on limitations due to cross-phase modulation in WDM multispan transmission systems," *Optical Fiber and Communication (OFC) Conference*, vol.1, pp.MF4-1-MF4-3, 2001.
- [57] T.N.Nielsen, B.J.Eggleton, J.A.Rogers, P.S.Westbrook, P.B.Hansen, and T.A.Strasser, "Dynamic post dispersion optimization at 40-Gb/s using a tunable fiber Bragg grating," *IEEE Photonics Technology Letters*, vol.12, no.2, pp.173-175, 2000.
- [58] K.Ennser, R.I.Laming, and M.N.Zervas, "Analysis of 40-Gb/s TDM-transmission over embedded standard fiber employing chirped fiber grating dispersion compensators," *IEEE Journal of Lightwave Technology*, vol.16, no.5, pp.807-811, 1998.

- [59] J.H.Winters and R.D.Gitlin, "Electrical signal processing techniques in long-haul fiber-optic systems," *IEEE Transactions on Communications*, vol.38, no.9, pp.1439–1453, 1990.
- [60] A.J.Weiss, "On the performance of electrical equalization in optical fiber transmission systems," *IEEE Photonics Technology Letters*, vol.15, no.9, pp.1225–1227, 2003.
- [61] C.R.S.Fludger, J.Whiteway, and P.Anslow, "Electronic equalization for low cost 10 Gbit/s directly modulated systems," *Optical Fiber and Communication (OFC) Conference*, WM7, 2004.
- [62] V.Curri, R.Gaudino, A.Napoli, and P.Poggiolini, "Electronic equalization for advanced modulation formats in dispersion-limited systems," *IEEE Photonics Technology Letters*, vol.16, no.11, pp.2556–2557, 2004.
- [63] C.R.Doerr, "Optical Compensation of System Impairments," *Optical Fiber and Communication (OFC) Conference*, OThL1, 2006.
- [64] G.-H.Lee, S.Xiao, and A.M.Weiner, "Programmable, polarization-independent, and DWDM-capable chromatic dispersion compensator using a virtually-imaged phased-array and spatial light modulator," *Optical Fiber and Communication (OFC) Conference*, OThE5, 2006.
- [65] S.Xiao and A.M.Weiner, "An eight-channel hyperfine wavelength demultiplexer using a virtually imaged phased-array (VIPA)," *IEEE Photonics Technology Letters*, vol.17, no.2, pp.372–374, 2005.
- [66] C.DeCusatis, E.Maass, D.P.Clement, and R.C.Lasky, "Handbook of fiber optic data communications", Academic Press, 1998.
- [67] S.Xiao and A.M.Weiner, "Programmable photonic microwave filters with arbitrary ultra wideband phase response," submitted to *IEEE Transactions on Microwave Theory and Technique*.
- [68] D.Breuer, and K.Petermann, "Comparison of NRZ- and RZ-modulation format for 40-Gb/s TDM standard-fiber systems," *IEEE Photonics Technology Letters*, vol.9, no.3, pp.398–400, 1997.
- [69] Z.Pan, Q.Yu, Y.W.Song, and A.E.Willner, "40-Gb/s RZ 120-km transmission using a nonlinearly-chirped fiber Bragg grating (NL-FBG) for tunable dispersion compensation," *Optical Fiber and Communication (OFC) Conference*, ThGG50, 2002.

- [70] Z.Jiang, D.E.Leaird, and A.M.Weiner, "Width and wavelength-tunable optical RZ pulse generation and RZ-to-NRZ format conversion at 10-GHz using spectral line-by-line control," *IEEE Photonics Technology Letters*, vol.17, no.12, pp.2733–2735, 2005.
- [71] G.-H.Lee, Z.Jiang, S.Xiao, and A.M.Weiner, "1700 ps/nm tunable dispersion compensation for 10 Gbit/s RZ lightwave transmission," *Electronics Letters*, vol.42, no.13, pp. 768-769, 2006.
- [72] J.T.Verdeyen, "Laser electronics," 3<sup>rd</sup> ed. Prentice Hall, Upper Saddle River, New Jersey, 1995.

## APPENDIX

## A. LOSS MECHANISMS IN VIPA BASED PULSE SHAPER

A simple model for understanding loss mechanisms in VIPA based pulse shaper is explained in this appendix. The model assumes Gaussian beam propagation along the free space. The Gaussian beam can be expressed as,

$$E(r, z) = E_0 \frac{\omega_0}{\omega(z)} \exp\left[-\frac{r^2}{\omega^2(z)}\right] \exp\left[-j\left\{kz - \tan^{-1}\left(\frac{z}{z_0}\right)\right\}\right] \exp\left[-j\frac{kr^2}{2R(z)}\right] \quad (\text{A.1})$$

where

$$\omega^2(z) = \omega_0^2 \left[1 + \left(\frac{z}{z_0}\right)^2\right], \quad R(z) = z \left[1 + \left(\frac{z_0}{z}\right)^2\right], \quad z_0 = \frac{\pi n \omega_0}{\lambda_0} \quad (\text{A.2})$$

where  $E_0$  is the initial field amplitude,  $\omega_0$  is the beam waist,  $n$  is the refractive index, and  $\lambda_0$  is the operating wavelength. The first term in Eq.(A.1) is the amplitude factor which describes amplitude of fields as beam propagates along z-direction. The second term in Eq.(A.1) is the longitudinal phase factor which describes changes in phase of beam as it propagates along z-direction. The last term in Eq.(A.1) is the radial phase factor which describes equiphase surface along z-direction (spherical with curvature  $R(z)$ ), more details can be found in [72].

The application of Gaussian beam in the VIPA can be understood as sum of the multiple beams in one observation plane with different phase fronts as (the concepts are shown in Fig.A.1 and Fig.A.2)

$$\begin{aligned} E(r, z) &= E_1(r, z) + E_2(r, z) + E_3(r, z) + \dots + E_N(r, z) \\ &= \sum_{n=1}^N E_n(r, z) \end{aligned} \quad (\text{A.3})$$

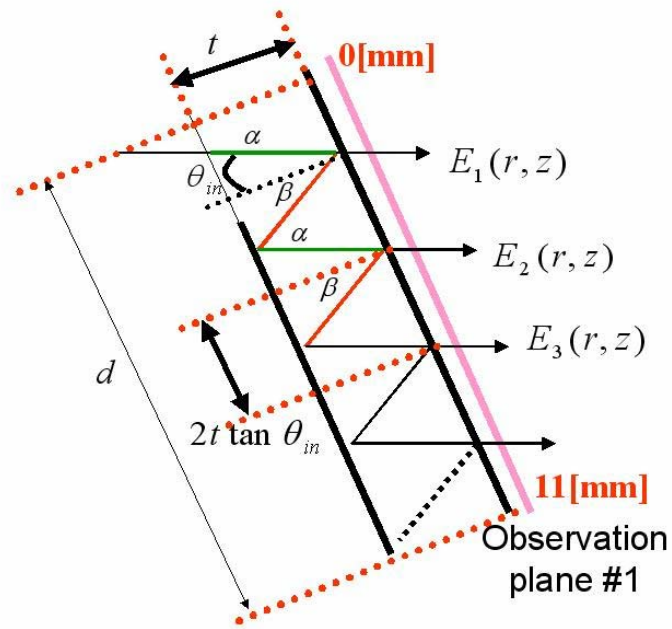


Fig.A.1 Gaussian beam path within the VIPA and output field at observation plane.

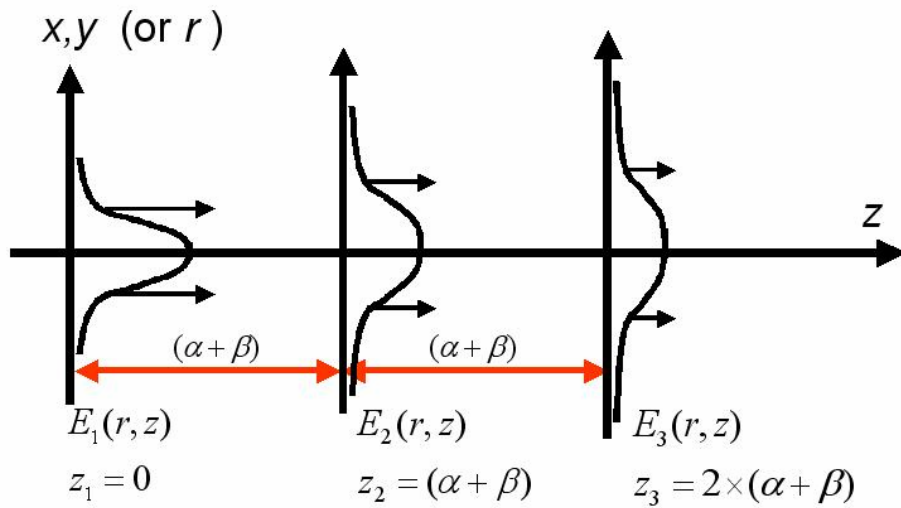


Fig.A.2 Multiple output field at the VIPA output (observation plane) expressed in terms of propagation axis ( $z$ -axis).

where

$$N = \frac{d}{2t \times \tan \theta_{in}}, \quad z_n = 2t \sin \theta_{in} \quad (\text{A.4})$$

where  $d$  is the length of the VIPA,  $t$  is the thickness of the VIPA,  $\theta_{in}$  is the light incident angle,  $N$  is the total number of discrete fields which is equal to the number of bounces of light path within VIPA, and  $z_n$  is the distance (spacing) between multiple outputs. Fig.A.3 shows a simulated example of normalized VIPA output intensity profile with respect to positions along the VIPA at the observation plane #1 in Fig.A.1.

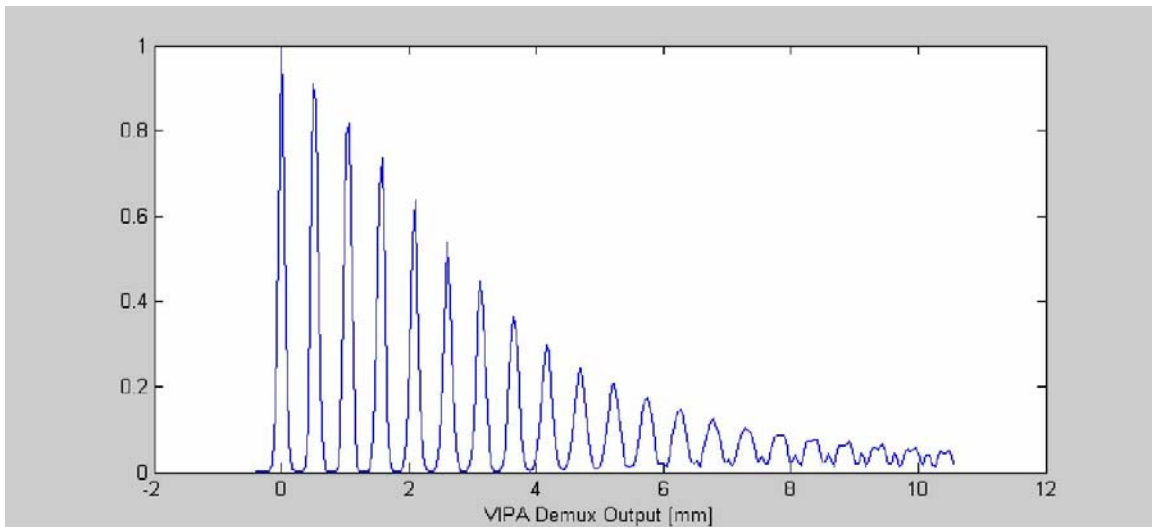


Fig.A.3 Simulated example of VIPA output at the observation plane.

The loss mechanisms of VIPA based pulse shaper include loss due to finite length of VIPA, loss due to coupling between propagating and reflecting waves, loss due to placing spatial mask (filter), and loss due to finite incident window.

The loss mechanism due to finite length of VIPA can be expressed as (and shown in Fig.A.4).

$$P_{inc} = P_{finite} + P_{trans} \quad (A.5)$$

$$L_{finite} = \frac{P_{finite}}{P_{inc}} = \frac{P_{finite}}{P_{finite} + P_{trans}} \quad (A.6)$$

where,  $L_{finite}$ ,  $P_{inc}$ ,  $P_{finite}$ ,  $P_{trans}$  denote loss due to finite length of VIPA, VIPA incident optical power, optical power lost due to finite length of VIPA, and transmitted optical power. The amount of loss can be adjusted by changing incident angle (thus increasing or decreasing number of bounces in the VIPA).

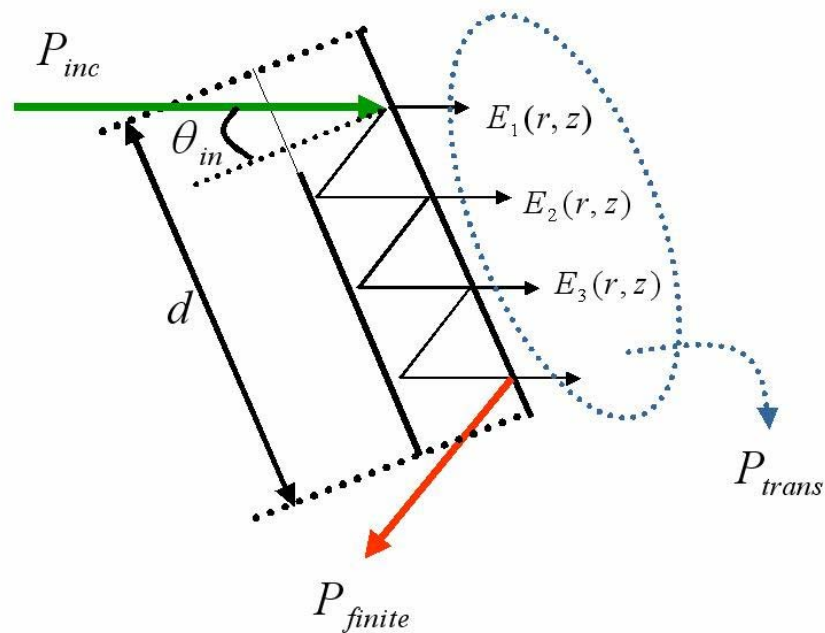


Fig.A.4 VIPA loss due to finite length of VIPA.

Fig.A.5 shows simulated results of VIPA output due to the coupling loss between propagating and reflecting waves. The coupling loss between propagating and reflecting waves arise from the geometry of apparatus which produces flipped version of multiple waves in propagating and reflecting directions as shown in Fig.A.5. Fig.A.6 shows the setup and observation planes of VIPA based pulse shaper to measure the loss mechanism due to coupling between propagating and reflecting waves. The propagating waves observed at VIPA output plane #1 in Fig.A.6 are those similar to Fig.A.3 (peak at the left hand side in Fig.A.5), and the reflecting waves observed at VIPA output plane #2 in Fig.A.6 have flipped profiles (peak at the right hand side in Fig.A.5). Fig.A.7 shows the convolved results of propagating and reflecting waves.

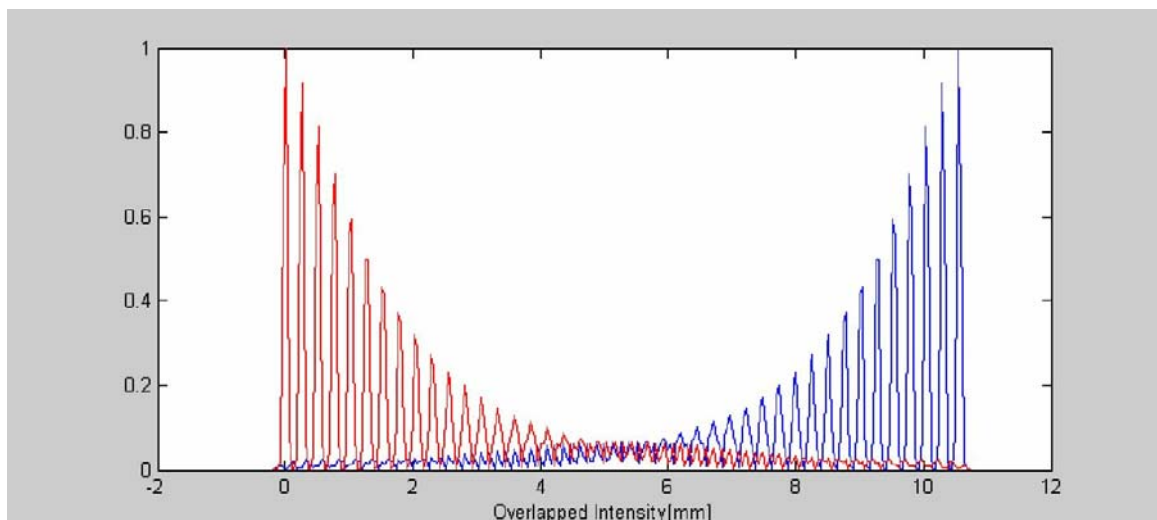


Fig.A.5 Simulated example of overlapped VIPA output of propagating and reflecting waves at the observation planes.

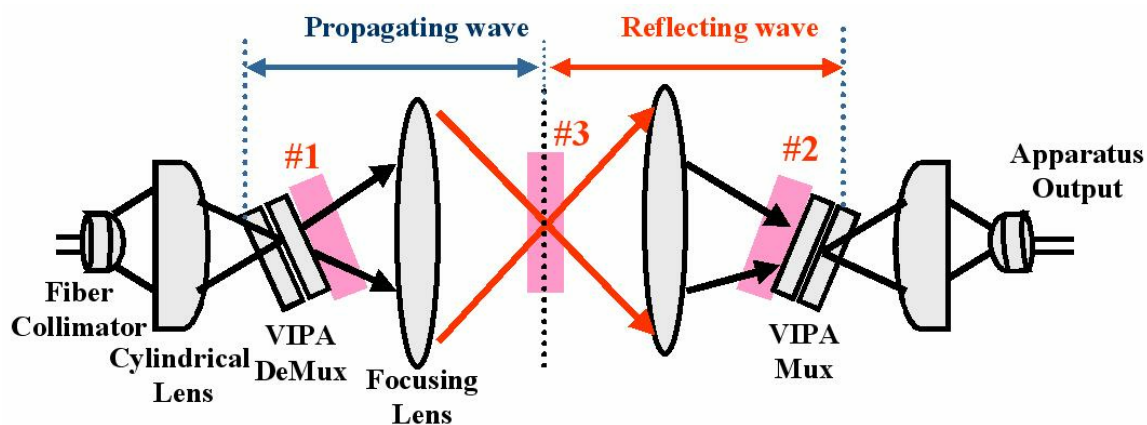


Fig.A.6 Setup and observation planes of VIPA based pulse shaper to measure the loss mechanism due to coupling between propagating and reflecting waves.

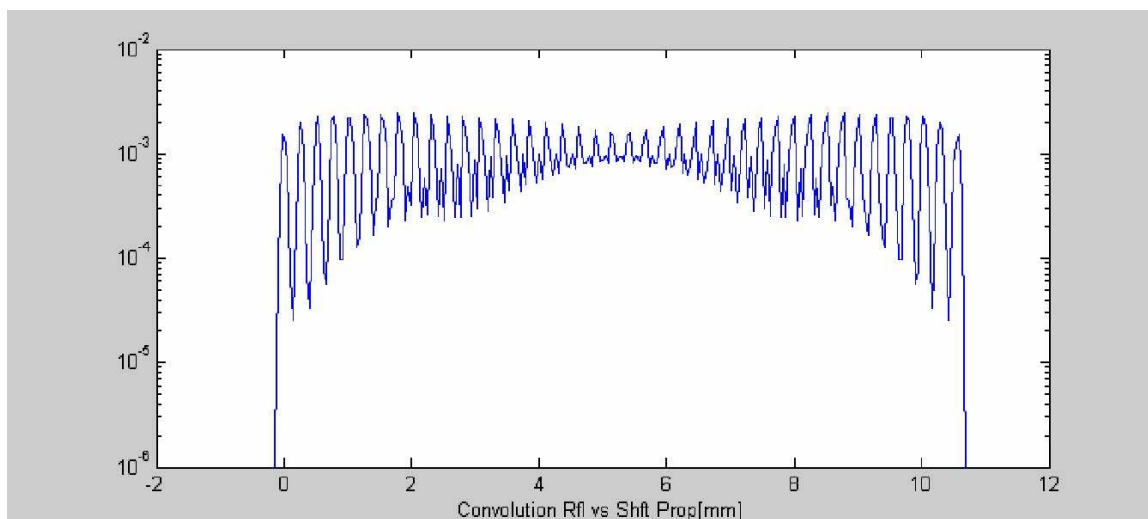


Fig.A.7 Convolved intensity for propagating and reflecting waves.

The loss mechanism due to placing a spatial mask (filter) arise due to passing only one spatial mode at the Fourier plane of the pulse shaper. This is similar to baseband operations which gets rid of all high frequency terms. It is more convenient to implement phase and amplitude modulation with one spatial mode after placing spatial masks but induce some additional losses.

The loss due to finite incident window happens because of the clipped portion of incident wave and first reflected wave. This losses can be adjusted by changing the incident beam size and incident angle.

The controllable parameters for the insertion loss mechanisms in VIPA based pulse shaper are relative amount of shift between VIPA DeMux and VIPA Mux ( $\delta$ ), input beam incident angle ( $\theta_{in}$ ), size of input beam waist ( $\omega_0$ ), size of spatial mask ( $\Delta v$ ), reflectivity of VIPA ( $R$ ), and position of incident beam ( $d$ ) as shown in Fig.A.8.

Fig.A.9 to A.12 show some results of changing controllable parameters for the insertion loss mechanisms in VIPA based pulse shaper. For these simulations, the size of spatial mask was fixed to get lowest order (baseband) mode only, the position of incident beam was centered in the middle (where it has lowest loss), and changing the reflectivity of VIPA was not considered. The length and thickness of the VIPA were 11-mm and 1.5-mm, respectively.

Fig.A.9 shows the simulated results for controlling the relative amount of shift between VIPA DeMux and VIPA Mux ( $\delta$ ). The beam waist was fixed to  $\omega_0 = 50\mu\text{m}$  and incident angle was  $\theta_{in} = 3\text{-degrees}$ . The upper figures are the overlapped intensities of propagating and reflecting waves and the lower figures are the convolved results of propagating and reflecting waves. Fig.A.9(a), A.9(b), A.9(c), A.9(d) are  $\delta = 0$ ,  $\delta = 3$ ,  $\delta = 5$ ,  $\delta = 8\text{-mm}$ , respectively. Fig.A.10 shows the insertion loss for controlling the relative amount of shift between VIPA DeMux and VIPA Mux. The minimum insertion loss occurs at  $\delta = 6\text{-mm}$ .

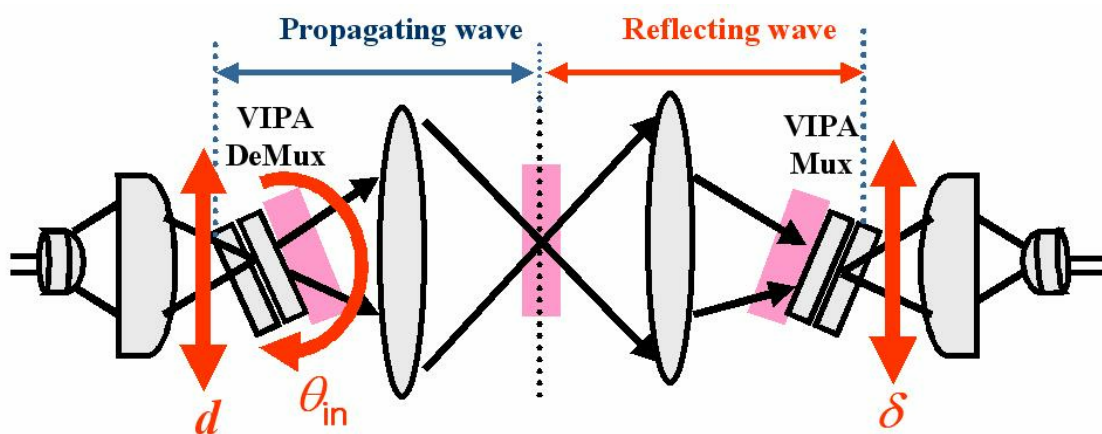


Fig.A.8 Controllable parameters for the insertion loss mechanisms in VIPA based pulse shaper : relative amount of shift between VIPA DeMux and VIPA Mux ( $\delta$ ), input beam incident angle ( $\theta_{in}$ ), position of incident beam ( $d$ ).

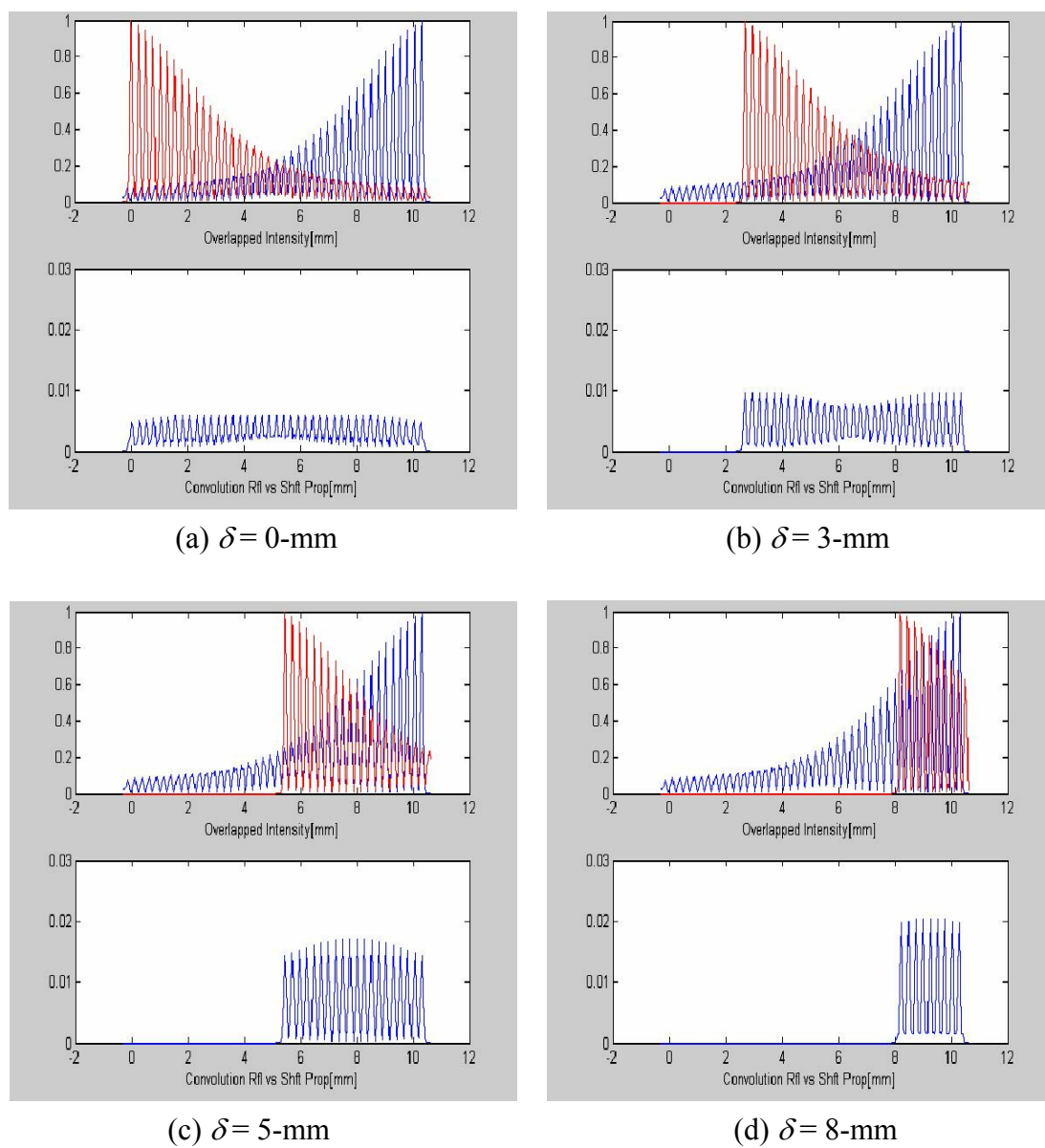


Fig.A.9 Simulated results for controlling the relative amount of shift between VIPA DeMux and VIPA Mux ( $\delta$ ). The upper figures are the overlapped intensities of propagating and reflecting waves and the lower figures are the convolved results of propagating and reflecting waves.

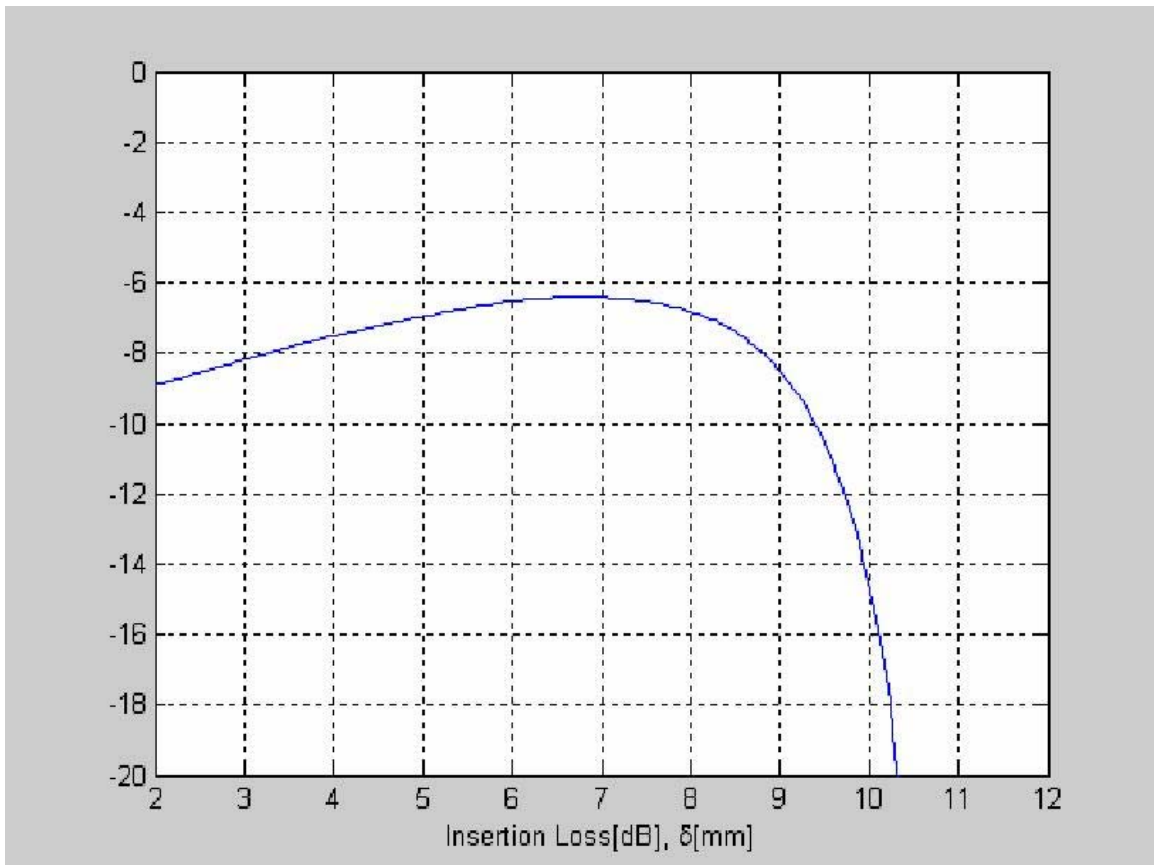
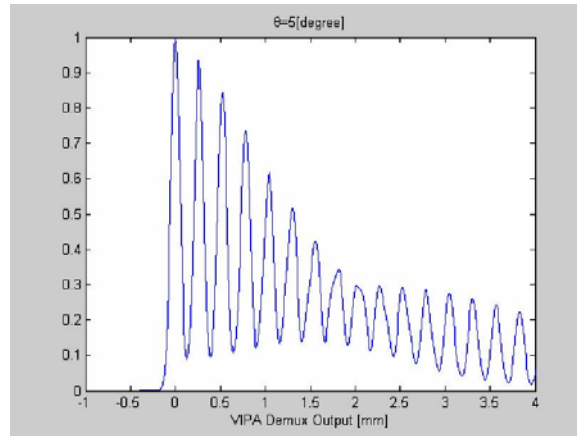
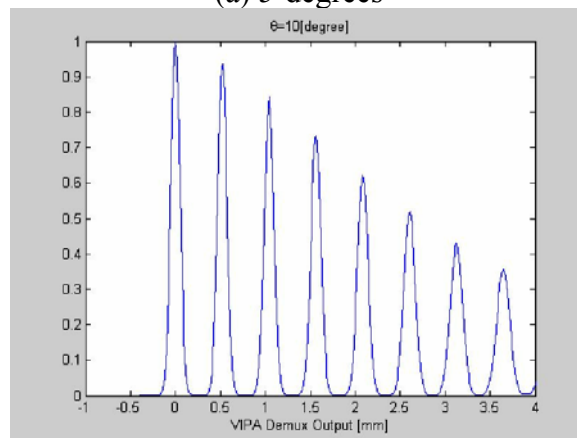


Fig.A.10 Insertion loss for controlling the relative amount of shift between VIPA DeMux and VIPA Mux. The minimum insertion loss occurs at  $\delta = 6$ -mm.

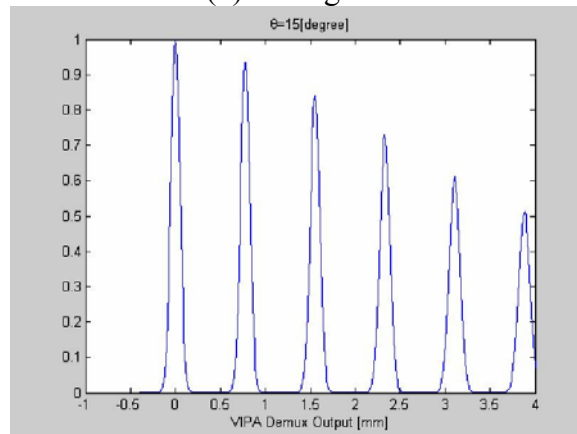
Fig.A.11 shows the simulated results of intensity of propagating waves for changing incident angle ( $\theta_{in}$ ). The beam waist was fixed to  $\omega_0 = 60\mu\text{m}$ . Fig.A.11(a), A.11(b), A.11(c) are  $\theta_{in} = 5$ ,  $\theta_{in} = 10$ ,  $\theta_{in} = 15$ -degrees, respectively. As incident angle increases, spacing between multiple modes increase, resulting in reduced number of bounces in VIPA. Fig.A.12 shows the insertion loss for changing incident angle. Optimum values for  $\theta_{in}$  and  $\delta$  are shown. The minimum insertion loss occurs at  $\theta_{in} = 5$ -degrees and  $\delta = 8$ -mm.



(a) 5-degrees



(b) 10-degrees



(c) 15-degrees

Fig.A.11 Simulated results of intensity of propagating waves for changing incident angle ( $\theta_m$ ).

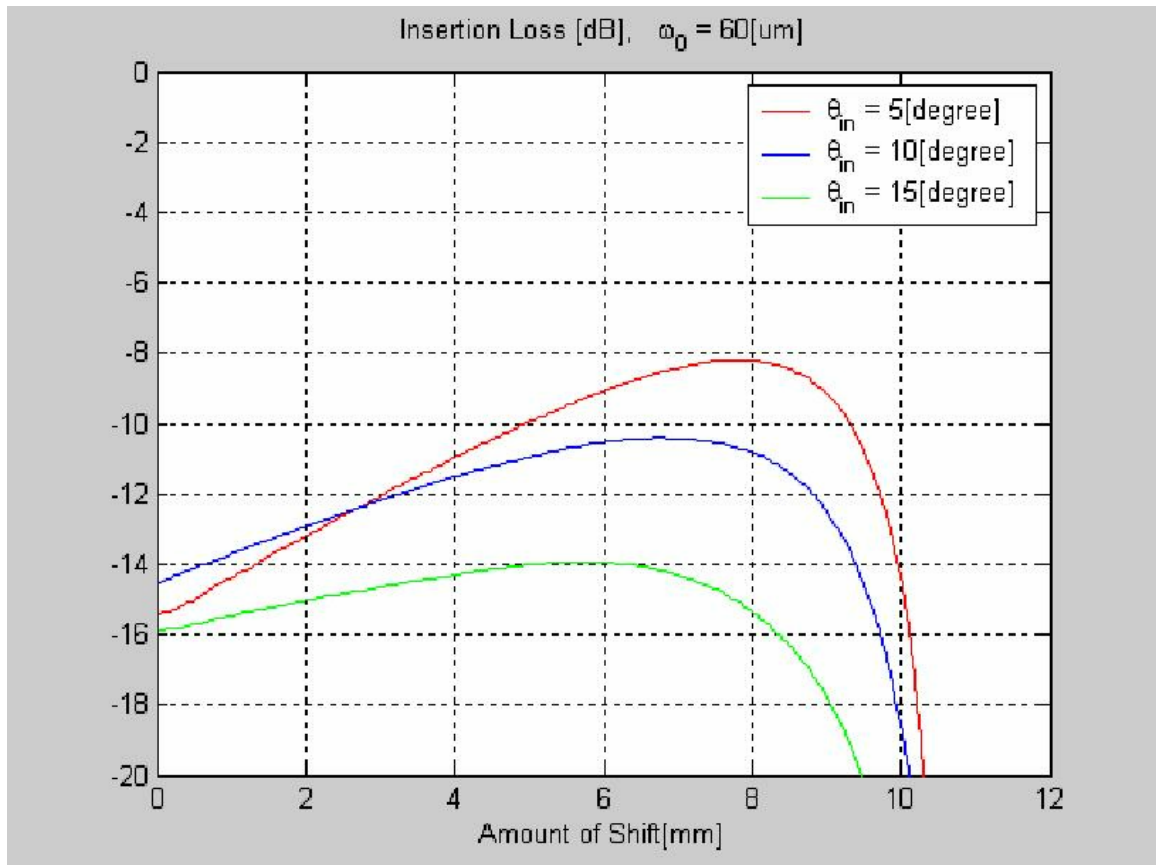


Fig.A.12 Insertion loss for changing incident angle ( $\theta_{in}$ ). Optimum values of  $\theta_{in}$  and  $\delta$  are shown.